# Intelligent and Automatic Inspection, Reconstruction and Process Planning Methods for Remanufacturing and Repair

by

Yufan Zheng

A thesis submitted in partial fulfillment of the requirements for the degree of

Doctor of Philosophy

Department of Mechanical Engineering

University of Alberta

# Abstract

Nowadays, it is critical to explore methods for dealing with worn and damaged components because of rising concerns over escalating emissions, resource depletion, and other environmental issues. Remanufacturing and repairing have been considered environmentally friendly manufacturing strategies to resist the increase in waste production. However, these processes are lacking automation support because compared to the manufacturing process, stochastic returns of used parts and their uncontrollable quality condition results in a high degree of uncertainty for the remanufacturing and repairing process. To fix these issues, the research proposed aims to automate and optimize the processes by improving the research areas in three perspectives: damage inspection (identification and localization), nominal volume reconstruction and process planning. The developed methodology features (a) an intelligent inspection to support automated classification and localization of damages from the end-of-life part; (b) an efficient geometric reconstruction of the damaged part to support the damaged volume extraction; (c) cost-driven and collision-free process planning that support hybrid remanufacturing processes.

From the perspective of intelligent damage inspection, the RGB images and depth images are acquired by a depth camera. Then, the deep learning neural network segments and classify the damage. With that result, the spatial position of the damaged area is calculated by the integration of damage segments and the point clouds. In the damage volume extraction view, an efficient and precise nominal model reconstruction method is

developed, which includes the processes of StepRANSAC surface fitting, SDM refitting, modelling, damage volume localization, and extraction. The result of reconstruction significantly facilitates the repairing process because it does not require prior information on the nominal CAD model. For hybrid remanufacturing, two hybrid manufacturing strategies are explored separately in developing the collision-free and cost-driven process planning. In both systems, the level of automation of hybrid processes is strongly increased. Finally, the conclusion, discussion and future work are followed. The proposed research can be extended to investigate damage quantification, freeform surface-based model reconstruction, process planning for complicated cases in future work.

# Preface

This thesis is my original work by Yufan Zheng. 6 journal papers related to this thesis have been submitted or published are listed below.

1. Y. Zheng, H. Mamledesai, H. Imam and R. Ahmad, "A novel deep learning-based automatic damage detection and localization method for remanufacturing/repair", *Computer-aided design and application* (accepted) (Chapter 3). (I was responsible for methodology development, coding, data collection, data analysis and paper writing; H. Mamledesai and H. Imam assisted with data collection; R. Ahmad was the principal investigator and supervisor on the project).

2. Y. Zheng, A. J. Qureshi, and R. Ahmad, "Algorithm for remanufacturing of damaged parts with hybrid 3D printing and machining process," *Manufacturing Letter* (2018), vol. 15, pp. 38–41. (Chapter 4 & 6). (I was responsible for methodology development, coding, data collection, data analysis and paper writing; J. Qureshi supervised the methodology and R. Ahmad was the principal investigator and supervisor on the project).

3. Y. Zheng, J. Liu, Z. Liu, T. Wang, and R. Ahmad, "A Primitive-based 3D Reconstruction method for Remanufacturing," *International Journal of Advanced Manufacturing Technology* (2019), 103, pp. 3667-3681. (Chapter 4). (I was responsible for methodology development, coding, data collection, data analysis and paper writing; J. Liu assisted with the data analysis; Z. Liu assisted with coding; T.

Wang assisted with the experiments and data collection; R. Ahmad was the principal investigator and supervisor on the project).

4. Y. Zheng, J. Liu, R. Ahmad, "A cost-driven process planning method for hybrid additive-subtractive remanufacturing," *Journal of Manufacturing Systems* (2020), vol.55, pp. 248-263. (Chapter 5). (I was responsible for methodology development, coding, data collection, data analysis and paper writing; J. Liu was involved with concept formulation; R. Ahmad was the principal investigator and supervisor on the project).

5. Y. Zheng and R. Ahmad, "Automated feature extraction for hybrid additive-subtractive remanufacturing", *Procedia CIRP*, vol.93, pp. 56-61 (Chapter 5 & 6). (I was responsible for methodology development, coding, data collection, data analysis and paper writing; R. Ahmad was the principal investigator and supervisor on the project).

6. Y. Zheng, R. Ahmad, "Feature extraction and process planning of integrated hybrid additive-subtractive system for remanufacturing," *Mathematical Bioscience and Engineering* (2020), 17(6), pp. 7274-7301 (Chapter 6). (I was responsible for methodology development, coding, data collection, data analysis and paper writing; R. Ahmad was the principal investigator and supervisor on the project).

# Acknowledgements

First, I would sincerely thank my supervisor, Dr. Rafiq Ahmad, for his advice, expertise and support. Also, I would thank my supervisory committee members, Dr. Yongsheng Ma, Dr. Basel Alsayyed Ahmad and Dr. Cagri Ayranci for their support and encouragement.

I would also like to thank all my collogues from the LIMDA lab, who has helped a lot in research, particularly, Dr. Pablo Martinez, Mr. Feiyu Jia, Mr. Harshavardhan Mamledesai, Mr. Juan Tzintzun, Miss Habiba Imam, Mr. Mario Soriano, Mr. David Baca, Mr. Pedro Yepez, Miss Saraswati Jituri.

Also, I would thank Dr. Jikai Liu from Shandong University for his encouragement and kind suggestions.

At last, I would thank my family and my fiancée Miss Xinning Wang for always supporting and caring for my life and studies.

# Table of Contents

# List of Tables

xii

# List of Figures

xvi

# List of Abbreviations

| | |
|---|---|
| CAD | Computer-aided Design |
| CAM | Computer-aided Manufacturing |
| CAPP | Computer-aided Process Planning |
| HM | Hybrid Manufacturing |
| RANSAC | Random Sample Consensus |
| SDM | Squared Distance Minimization |
| CNC | Computer Numerical Control |
| PBF | Powder Bed Fusion |
| DED | Directed Energy Deposition |
| CMM | Coordinate Measuring Machine |
| LiDAR | Light Detection and Ranging |
| CNN | Convolutional Neural Network |
| RGB-D | Red, Green, Blue-Depth |
| PCS | Prominent Cross Section |
| AM | Additive Manufacturing |
| SM | Subtractive Manufacturing |

| | |
|---|---|
| CSG | Constructive Solid Geometry |
| B-rep | Boundary Representation |
| MF | Machining Feature |
| AF | Additive Manufacturing Feature |
| SF | Subtractive Manufacturing Feature |
| ResNet | Residual Network |
| FPN | Feature Pyramid Network |
| IoU | Interest-over-union |
| RoI | Region of Interest |
| AFG | Additive Feature Group |
| SFG | Subtractive Feature Group |
| AFV | Additive Feature Volume |
| SFV | Subtractive Feature Volume |
| MRR | Material Removal Rate |
| PCOSP | Precedence-constrained operation sequencing problem |

# Chapter 1: Introduction

## 1.1 Background

From the World Bank report, currently, about 2.01 billion metric tons of municipal solid waste is produced annually worldwide (reported in 2018) and it estimates overall waste generation will increase to 3.40 billion metric tons by 2050 [1]. Therefore, annual global waste production will increase by 70% if current conditions persist. The increasing economic developments and over-exploitation of resources have been the principal cause of the increase in waste production [2]. The pressure for the environment from the increased waste production can be summarised in three perspectives [3]:

1. It results in the permanent loss of materials and energy;
2. As the current landfill sites are filling up, and it leads to the use of new sites;
3. The waste left in landfill sites leads to the increase of air, water and air pollutions.

To resist this change, the modern industry is required to invest in environmental protection measures and create environmentally friendly manufacturing concepts [4–8].

Figure 1.1 illustrates a conceptual diagram of the product circulation that can be used in environmentally friendly manufacturing. Repair is the most logical approach to extend the product's life while closing the product life cycle. The process is the correction of specified faults or restoring its original form of the product. Remanufacturing also called "reincarnation", is defined as being able to fabricate new products directly from the end-of-life product by enabling the material to be effectively used resulting in reduced waste [9]. It is reported that, compared to conventional manufacturing, the remanufacturing and repairing process reduces cost up to 50%, energy consumption up to 60%, material usage up to 70% and air pollution up to 70% [2,10].
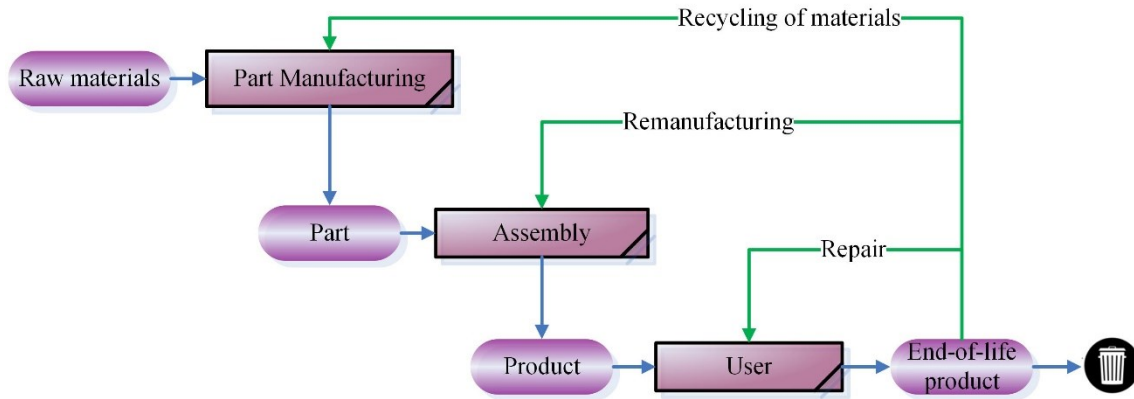
Figure 1.1: The concept of the product life cycle (modified from [3]).

It is worth to mention that, the terms "repairing" and "remanufacturing" have been used as exchangeable words with the burred definitions [3]. In this thesis, to avoid any potential confusion, remanufacturing and repairing processes are distinguished, as repairing rebuilds the part to its original shape, whereas remanufacturing upgrades the part to have new functional features.

## 1.2 Motivation

Although significant benefits can be gained from remanufacturing and repair, there are still numerous challenges to implement them in the industry. One of the reasons is that, compared to the manufacturing process, stochastic returns of used parts and their uncontrollable quality condition result in a high degree of uncertainty for the remanufacturing/repairing process [6]. The uncertainty surrounding the return of the parts complicates the process. To handle these uncertainties, remanufacturing is initialized by inspections to determine the damage type (e.g. crack, dent, scratch, abrasion), damage location and damage degree.    The current visual or manual inspection methods require extensive human intervention, and the quality of the process is hard to be stable. Besides, extraction of the damaged volume is an essential work for remanufacturing. However, research focusing on solving this problem is lacking, especially for a general situation in which the nominal computer-aided design (CAD) model is missing.  Another issue is that the computer-aided process planning software tools are lacking support for automation.

2

For example, feature extraction for hybrid manufacturing (HM) relies heavily on manual operations that lack algorithm support; and the process planning results are non-unique and the quantitative evaluation mechanism is missing to support decision making (e.g., cost-driven decision making). In order to address these problems, this thesis will explore the perspectives of inspection, damaged volume extraction and process planning for remanufacturing and repair.

## 1.3 Thesis Objectives

The objectives of this research are outlined as follow:

- **O1**: Develop an intelligent inspection method to support the automated detection of damage features, and localization of the defects from the damaged part.
- **O2**: Develop an efficient geometric reconstruction method for the damaged part to support the damaged volume extraction;
- **O3**: Develop a cost-driven process planning method for hybrid additive-subtractive remanufacturing processes.

## 1.4 Methodology

The proposed methodology aims to automate and optimize the remanufacturing and repairing processes. The current remanufacturing and repairing processes can be improved in terms of damage inspection, damage volume extraction, and process planning. The contributions of this study in damage inspection are beneficial to both remanufacturing and repairing processes. The contribution of damage volume extraction is aiming to improve the current repairing process. The framework of process planning is focusing on remanufacturing. An overview of the methodology is illustrated in Figure 1.2 and explained next.
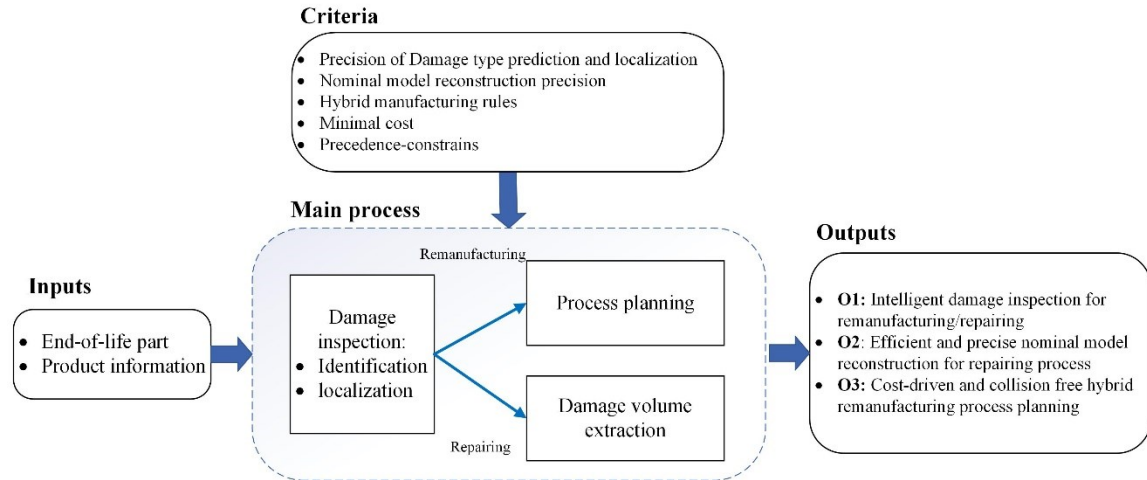
Figure 1.2: Overview of the Methodology.

With the input of the end-of-life part to the system, outputs are following the thesis objectives listed in Section 1.3. The proposed methodology can be divided into three research gaps with proposed solutions, as *damage inspection*, *damage volume extraction* and *process planning.* The more descriptions are given as follows:

- In *damage inspection*, the end-of-part is processed with the intelligent damage inspection system, and the results are beneficial for process planning in remanufacturing and damage volume extraction in repair. The damage inspection system is proposed under the integration of deep learning-based image recognition and spatial localization methods.

- The results of the damage inspection are transiting into the *damage volume extraction*. This module outputs the reconstructed nominal model of the damaged part to support the damaged volume extraction for the repairing process. The proposed nominal model reconstruction method is based on a novel proposed surface fitting approach.

- The module of *process planning* is specifically designed for a hybrid additive-subtractive process in the remanufacturing context. The result of the damage inspection is the starting point of this module and it outputs a cost-driven and collision-free system for hybrid remanufacturing process planning. The methods proposed in this module are including automated additive-subtractive feature extraction, HM rules,

feature-based cost estimation and precedence-constrained operation sequencing optimization.

The outputs of the proposed methodology conform to the three research objectives presented in Section 1.3, listed as follows:

- Intelligent damage inspection for remanufacturing/repairing;
- Efficient and precise nominal model reconstruction for repairing;
- Cost-driven and collision-free process plans for hybrid remanufacturing.

## 1.5 Thesis Outline

Chapter 1 provides the background of remanufacturing/repairing and their relations to the product life cycle. The motivations are summarised from challenges related to the current remanufacturing/repairing technologies. A brief statement on the objectives of this thesis and the overview of the proposed framework are also presented in this chapter.

Chapter 2 is a general state of the art summary on the main topics covered in this thesis, including defect detection, damaged volume reconstruction and hybrid additive-subtractive for remanufacturing/repairing.

Chapter 3 presents a deep learning-based damage inspection and localization method for the remanufacturing/repair process. The proposed approach is divided into two stages: (1) damage recognition and classification; (2) spatial localization for the damaged area. The case study validated the efficiency and precision of the proposed method.

In Chapter 4, a geometric reconstruction method for the damaged model is proposed to address the nominal model missing issues of the damaged part in the repairing process. The proposed method features a novel primitive-based surface fitting approach. This technique combines the StepRANSAC (step random sample consensus) surface fitting and SDM (squared distance minimization) refitting, and this combination shows advantages in

precision and robustness compared with the traditional RANSAC method. Four case studies were conducted to validate the effectiveness of the proposed method.

Chapter 5 describes a cost-driven process planning method for hybrid computer numerical control machining (CNC) and powder bed fusion (PBF) in the remanufacturing context. An automated additive–subtractive feature extraction method is developed, and the process planning task is formulated into a cost-minimization optimization problem to guarantee a high-quality solution. Specifically, an implicit level-set function-based feature extraction method is proposed. Precedence constraints and cost models are also formulated to construct the hybrid process planning task as an integer programming model. Numerical examples demonstrate the efficacy of the proposed method.

Chapter 6 proposed a cost-driven and collision-free process planning method for hybrid CNC and direct energy deposition (DED) for remanufacturing. The feature extraction method is developed under the level set framework, can extract optimal and collision-free additive-subtractive features. A case study was conducted, and the results confirm the correctness and effectiveness of the proposed method.

Finally, Chapter 7 summarizes the work done in this thesis. The limitations and future works are discussed.

# Chapter 2: State of the Art

Remanufacturing and repairing have been attracting attention as an emerging field due to their contributions to the increasing in green manufacturing industries. They have been already been applied to different products such as automobile parts [11], aerospace turbine blades [12,13], printer cartridge [14], machinery [15]. The concept of remanufacturing/repairing is clearly distinguished from recycling and reuse. Recycling is the use of raw materials which is obtained by dissolving or disassembling the end-of-life products. Reuse is defined to use the product again after some simple repairs and cleaning, without a manufacturing process [6]. Remanufacturing/repair is defined as an alternative manufacturing process that allows the end-of-life products to be re-commercialized as new products. In this study, repairing and remanufacturing are clearly distinguished, as repairing rebuilds the part to its original form, whereas remanufacturing upgrades the part to have new functional features.

Summarized from the literature [16–18], the major steps of remanufacturing/repairing processes can be summarized as defect detection, damaged volume reconstruction and HM (see Figure 2.1). The following sections in this chapter are providing comprehensive surveys for each step.
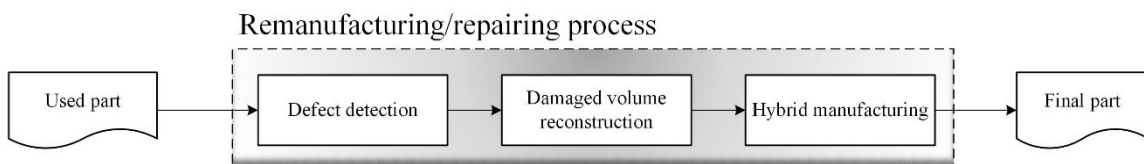


Figure 2.1: The main procedures of remanufacturing/repairing.

## 2.1 Defect Inspection

The main purpose of defect inspection is to detect the damage type, damage location and damage degree, since these three factors play a key role in process planning construction for remanufacturing and repair [2]. However, defect inspection is a challenging task for a human operator, especially when dealing with small defects that are not at all visible to

the naked eye. Therefore, after digitalization the physical used part by data acquisition, quickly and accurately detection damaged area from the digital data could be considered as the starting point for the remanufacturing/repairing process.

There are two categories of damage detections given in recent publication, through collecting point clouds or images from the damaged component. The related works of these two classes of methods are reviewed and summarized as follows.

## 2.1.1 Defect Inspection from Point Clouds

To transform from the physical world to the digital world, reverse engineering starts with geometric information acquisition by collecting the points on the surface of the part. The accumulation of these points is point clouds, that explicitly describing the surface geometric information of the part. In the recent three decades, diverse technologies and systems have been employed in point cloud acquisitions, such as coordinate measuring machine (CMM), triangulation, structured light and stereo scanning [19]. These technologies are gradually replacing manual measurement and facilitating the process of remanufacturing/repairing for accurate and quick collection of the geometric information of the used part. For remanufacturing/repair, as the point clouds of the used part are obtained, it is important to detect and segment the damaged area from the point clouds.

Of the methods surveyed, most defect inspection approaches from point clouds are based on the point cloud segmentation methods. A recent comprehensive review for point cloud segmentation methods is generally categorized them into five classes: edge-based methods, region-based methods, attributes-based methods, model-based methods and graph-based methods [20] (Figure 2.2). Edge-based methods [21–23] detect the boundaries of different regions from the point clouds to segment regions. The principle of these methods is finding the target points which have rapid change in the intensity. Edge-based methods allow fast segmentation, but they have accuracy issues since they are very sensitive to noise and point cloud density unevenness, which usually happens point cloud data [20]. In region-based methods [24–26], neighbourhood information is utilized to

combine nearby points that have similar characterizations to isolate regions and consequently distinguish different regions. Region-based methods are not that sensitive to noise as the edge-based method, however, they have problems with over or under segmentation [20]. Attributes-based methods [27–29] are based on clustering attributes of point cloud data. The limitation of these methods that the quality of derived attributes is highly required. Model-based methods [30–32] use primitives (e.g. plane, cylinder, sphere and cone) for grouping point based on RANSAC (RANdom Sample Consensus) [33] surface fitting. These methods are robust with outliers, but it is inaccurate in dealing with different point cloud sources. Graph-based methods consider the point clouds in terms of a graph, and each point is corresponding to the vertex in the graph. Graph-based methods [34–36] have better results with complex point clouds include noise and outliers, compared to other methods. However, the main limitation of this kind of method is difficult in running in real-time [20].
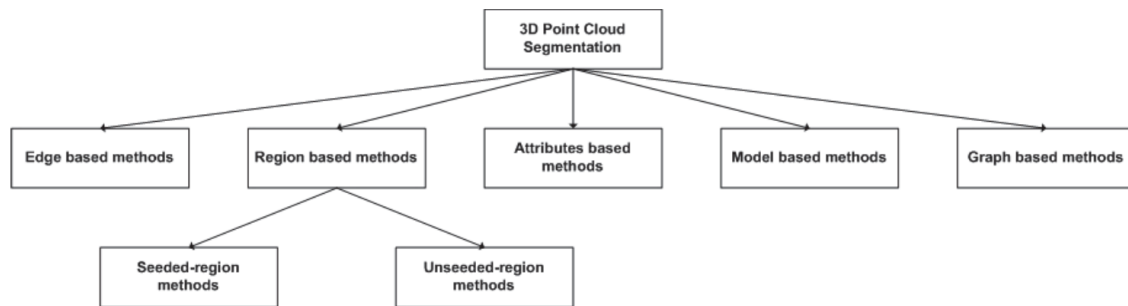


Figure 2.2: Taxonomy of 3D point cloud segmentation methods (from academic research [20]).

Researches have devoted efforts in defect detection from point cloud data by implementing these generic surface segmentation methods. Hitchcox and Zhao [37] have developed an graph-based point cloud segmentation method for interactive defect segmentation from unorganized 3D point cloud data with application to aerospace repair. The algorithm is an adaptation of random walks [38] from image segmentation, and the implementation automatically labels disconnected graph components, which allows for interactive and intuitive use directly on point clouds. This method provides a full pipeline for extracting and quantifying a wide range of surface defects from the complex surface,

9

such as the aerospace turbine blade. Jovančević et al. [39] introduced a novel automatic defect inspection method by analyzing 3D data collected with a 3D scanner. Firstly, the point cloud is pre-processed to remove the errors and outliers. Then, this segmentation algorithm identifies the defects and their positions. This algorithm is based on estimating the differences of curvature and normal information at every point from the neighboring point clouds to identify undesired defects as dents, protrusion or scratches. Borsu et al. [40] developed an integrated method for automated surface deformations detection and marking on automotive body panels. It extracts the damaged region from input point clouds by estimating the standard deviation of the surface normal vector as a metric, which removes uniform surface and remains the patches containing shaper variations of their normal orientations. The positions of the surface defects are provided to support a robotic marking system that handle pose and motion estimation of the part on an assembly line.

3D point clouds-based damage inspection technologies have been also widely applied in other areas such as civil and plant facilities. Kashani & Graettinger [41] introduced a clustering-based feature segmentation method for light detection and ranging (LiDAR) point clouds and applied in detection damages for building roofs. Shinozaki et al. [42] developed an automatic detection method to find scaffolding and wearing on furnace walls from large-scale point clouds.

## 2.1.2 Image-based Damage Inspection

Computer vision sensors have presented an alternative for data acquisition by collecting images from the physical part. Therefore, another damage detection method is based on analyzing the input data of images from the damaged components.

The feature-based inspection method has been widely implemented for extracting the properties of images, including colour, shape and texture [43]. An expert system can be built for further classification based on the extracted features. Iglesias et al. [44] introduced an automated inspection system based on feature extraction and studying the trait and characterization of slat slabs. In [45], a distinct man-made "light and shadow" feature was

developed to extracted to identify weld defects. Aminzadeh and Kurfess [46] proposed a new approach for the threshold selection method to find the threshold value at the boundary of the intensity ranges of defects and background by comparing the histogram modes of the background and defective areas. For the feature-based defect inspection methods, the feature quality heavily relies on the experiences of the system designer. Moreover, the designed feature extractors are constrained to the application scenario, which means ones the scenario changes, the designed feature extractor may not be suitable [43].

Template matching is another methodology applied to defect detection, by matching the images of the defect-free reference and the defective part. In [47], a fast normalized cross-correlation (NCC) computation was used for defect inspection. Crispin and Rankov [48] proposed an improved template-matching approach for defect identification and the search for a template position was conducted by using a genetic algorithm. Kong et al. [49] introduced a unified framework for detecting defects in planar industrial products based on the template matching method through a robust geometric alignment method between the template and test images. The template matching-based methods have shown the efficiency in detecting defects for the products with the prior knowledge of a template or reference image. It has significant potentials to be applied to quality controlling in production. However, this type of method has an intrinsic weakness for defect inspection in the remanufacturing/repairing context, due to the lack of template images.

Deep learning techniques have achieved substantial development in object detection and classification from images in recent years, which uses a series of layers of nonlinear activation functions. With such structure, it enables to integrate feature extraction and classification by optimization, and outputs expected label in the last layer. Benefiting from this effective method, some researchers have been implementing deep learning-based algorithms in defect inspection problems. Masci et al. [50] presented a Max-Pooling Convolutional Neural Network (CNN) method for the classification of 7 different steal defects; however, their work was limited to a shallow neural network. In a modern

implementation of a CNN in image classification, Wang et al. [43] presented a CNN-based vision inspection method to identify and classify defective product with high accuracy. However, image classification cannot achieve all goals of defect inspection, lacking finding the position of the defect area. Many state-of-the-art object detection methods have been developed using the region-based CNN (R-CNN) architecture. Mask R-CNN as an extension of R-CNN enables simultaneously object detection and instance, segmentation [51]. It has two stages: 1. Images are scanned, and the object proposal (bounding box to determine the objects) is generated; 2. The proposal is classified, and the bounding box and mask are generated. Instance segmentation features the potentials to address the localization problems of the defective area in a two-dimensional (2D) aspect. Ferguson et al. [52] introduced an automatic defect detection method to identify casting defects in X-ray images, based on the Mask R-CNN architecture. Zhang et al. developed a vehicle-damage-detection segmentation algorithm based on transfer learning and an improved Mask RCNN. However, their method can only find the damaged area from the images directly in 2D which has a huge error matching to its position in the real world.

With the development of the techniques of RGB-Depth sensors, the semantic segmentation has a great achievement in indoor scenes [53]. By adding the depth map, the RGB-D image gives information about the distance of the objects to the camera. Besides, the RGB and depth map have the corresponding relations in pixels. Gupta et al. [54] developed a two-step method to apply different neural networks to RGB and depth map separately to extract the corresponding features separately and classify by support vector machine in the end. Song and Xiao [55] adopt a directional Truncated Signed Distance Function encoding method to train the RGB-D data in the CNN directly and outputs 3D object bounding boxes.

## 2.1.3 Summary of the Existing Defect Inspection Methods

Over the comprehensive review of the current publications, defects inspection methods from point clouds can offer accurate results based on surface segmentation techniques. However, there are still some limitations of those methods, such as lacking a generalized

algorithm to detect defective regions for all applications, disallowing to classify different classes of damages, performing at low speed due to the computational expense.

In terms of the image-based damage detection methods, the issues of damage detection from point cloud data can be addressed through the deep learning architecture. However, the existing methods mainly focus on object detection or semantic segmentation in 2D senses. The spatial localization of the damaged area is a crucial task in the remanufacturing/repairing process. With the development of the RGB-D hardware technologies and 3D semantic segmentation methods which are more promising to classify objects, it is important to employ these methods for a damage inspection. However, most of the 3D semantic segmentation methods are applied for indoor objects. The great performances of these methods rely on large RGB-D training data [56]. Therefore, developing a deep learning-based damage detection method from RGB-D data is urgently demanded.

## 2.2 Damaged Volume Reconstruction

Damage volume reconstruction is an essential process for the repairing process, as it generates the deposition tool-path for restoring the damaged components to original geometries. There are two categories of damage volume reconstruction methods from recent publications, depending on whether the nominal CAD model is available for the repairing process.

When the nominal CAD model is available, the principle of methods is reconstructing the damaged volume by guidance from the nominal model. In [12], the reconstruction process is conducted by employing point-to-surface-best-fitting technology that puts the point clouds of the damaged part into the nominal CAD model coordinate system. Zhang et al. [57] developed a damage volume extraction method based on aligning the point clouds of a nominal and damaged model and finding the intersection by casting the ray with the nominal and damaged model. In [58], a four steps best-fitting method was proposed to reconstruct the missing volume. However, in the most general case, the

original CAD model is not available because of confidentiality issues, and occasionally, the CAD model may not correspond exactly to the real part [59]. Therefore, the reconstruction of the damaged part is an important step for CAD source-free repairing.

Some research works have been witnessed on reconstruction for CAD source-free repairing. He et al. [60] introduced a curved surface extension approach to reconstruct the missing volume based on continuous curvature for blade repairing. Gao et al. [61] proposed a reverse engineering-based surface extension method to reconstruct the blade tip. The reconstruction method in [62] resolves this issue by sweeping a surface across the defective region. In [13,63,64], a novel algorithm was developed to reconstruct a model of a defective region of a turbine blade. The algorithm implemented the concept of a sectional gauss map to extract prominent cross section (PCS) from a meshed model. Then, the extracted PCS information was used for semi-automated reconstruction of the geometries for the turbine blade. Li et al. [18] extended the PCS algorithm for reconstruction of other industrial parts, such as a worn gear bracket. The accuracy of this method is strongly dependent on the geometry completeness and will reduce with a larger damaged area.

From the review of the current nominal model reconstruction approaches, it can be concluded that they are heavily relying on the surface fitting techniques to construct a nominal surface to fit the point cloud of the damaged area. Therefore, a comprehensive review of surface fitting techniques is given in the following section.

## 2.2.1 Surface Fitting

Surface fitting is still an unresolved problem in reverse engineering and computer graphics [19]. Many research efforts have been devoted to addressing this problem in the last two decades. This section briefly reviews some methods that are related to the proposed algorithm. The surface fitting can be considered as an optimization problem that searches the optimal surface shape and location parameters by minimizing its overall distance to a collection of points. Therefore, the formulation of the distance-based objective function is

critical, which is mainly categorized into four types: (1) algebraic distance; (2) point distance; (3) tangent distance; (4) squared distances [65]. Algebraic distance is straightforward which substitutes the measured points in the corresponding implicit function of the target surface and then calculates the summation of errors. The algebraic distance is unable to reflect the accurate distance, but the calculation speed is fast. Point distance is to calculate the shortest Euclidean distances from the measured points to the target surface. The point distance is popular in computer graphics applications [66] and reverse engineering [67] because the equation is simple and straightforward [65]. However, the convergence is relatively slow, and the result is highly dependent on the quality of the initial guess. The tangent distance-based curve or surface fitting is very popular in the computer vision community due to the faster convergence than the point distance-based method. In terms of squared distance, Wang et al. [68] originally introduced the SDM for B- spline curves, and Wang and Yu [65] applied this method for quadratic curves and surfaces. SDM is a curvature-based quadratic approximation of the squared distances from the point cloud to the target surface. Compared with other distance measurements, the squared distance method can faithfully measure the geometric distance between the points to the target surface. Moreover, the convergence of SDM is more stable and faster than the other mentioned methods.

This non-linear optimization for surface fitting is widely used for reverse engineering. However, it is still a challenge to deal with the noise and outliers in realistic scanning [69]. Additionally, the quality of surface fitting is highly dependent on the results of segmentation and has a high requirement on the initial guess. Fischler and Bolles [70] firstly introduced the basic RANSAC which later became one of the most well-known algorithms to detect surfaces from the data sets that contain noise and outliers. It is an iterative process that randomly samples a subset from the data points in each iteration to estimate the corresponding model parameters. Schnabel et al. [71] developed the seminal paper for applying the RANSAC method in the surface fitting. Li et al. [31] and Le and Duan [72] developed the GlobFit method and the global 3D segmentation, respectively, to improve the robustness of the original RANSAC method by coupling local and global

aspects of the fitting problem. Even though RANSAC has been extensively developed, it is unable to reach high accuracy compared with the non-linear optimization methods.

## 2.2.2 Summary of the Current Damaged Volume Reconstruction Methods

Based on the literature review, it is concluded that the existing reconstruction methods mainly focus on turbine blades or some other specific cases. In most of the available reconstruction methods, the damaged region is assumed to be a regular shape, which might not be true in reality. Accordingly, a damage reconstruction approach for remanufacturing/repairing, including identification of defects and reconstruction of the original model, which is compatible with different types of damage, is urgently needed.

## 2.3 Hybrid Manufacturing for Remanufacturing/Repairing

In the past decade, additive manufacturing (AM) has gained significant attention and has revolutionized the manufacturing paradigm. It is now a sophisticated process for functional metal part fabrication [73–76]. AM has demonstrated various benefits, including greatly enhanced design freedom [77], simplified supply chain management [78], efficient raw material usage, and reduced environmental impact [79]. However, AM techniques have certain limitations, such as long production time, poor dimensional accuracy, and low surface quality [80]. Comparatively, subtractive manufacturing (SM) (usually machining), as a traditional manufacturing process, is still indispensable for producing parts with high surface quality and tight tolerance requirements, even though its capacity for complicated part manufacturing is quite restricted. Therefore, HM has emerged from a mixture of AM and SM to provide a more flexible, capable, and efficient manufacturing approach, which makes full use of the individual processes' advantages. At the same time, HM raises the capability of remanufacturing to a higher level, since features can be flexibly added and removed.

## 2.3.1 AM for Remanufacturing and Repair

As an AM technique, Directed Energy Deposition (DED) has been extensively used for repairing. Different aspects of it have been widely explored, such as laser parameters (e.g., laser power, feed rate, and traversing speed) [81], damaged geometry reconstruction [58,63], energy and environmental impact analysis [8,13], and microstructure and mechanical property analysis [74,82,83]. The PBF technique has also been applied for part repairing [84–86]. In comparison with DED, the capability of PBF for remanufacturing is restricted because of smaller build envelopes and the limited accessibility of new material deposition. For instance, the material can only be deposited on a flat surface but not inside a concave structure. Some of the studies have investigated the feasibility of PBF-based AM technologies for building new features on an existing part [73,84,87]. They have found that new features have fine microstructures and the interfaces between new features and the existing part have good metallurgical bonding. Therefore, part repairing with DED and PBF has both demonstrated high potentials [88].

However, because of the poor dimensional accuracy and reduced surface quality of additively manufactured components, SM is commonly implemented as a post-processing operation to help repaired parts meet tolerance requirements. Recently, HM, combining AM and SM for repairing or remanufacturing, has been actively investigated. Jones et al. [89] reported progress toward an HM machine that integrates laser cladding, machining, and in-process 3D scanning for flexible and lean remanufacturing of turbine blades. Zheng et al. [90] proposed a 3D reconstruction and a ray or triangle intersection algorithm to identify areas of a broken turbine blade that need repairing through HM. Li et al. [18] developed a part repairing method which integrates the functions of 3D scanning, model reconstruction, fine registration, and selection of the repairing method to restore a worn component. Hascoët et al. [59] proposed a method to automate the repairing process of metallic parts partially. In their method, defects were machined into a surface cavity and the cavity was refilled by laser metal deposition with the aid of an inspection system. Newman et al. [9] and Zhu et al. [91] put forward a remanufacturing framework that

consisted of fused filament fabrication, CNC machining, and inspection. The method enabled the remanufacturing of an existing part or even a recycled and legacy part by reincarnating it into a new part with enhanced structural features. Le et al. [88] extended the idea of remanufacturing through a combined (i.e., hybrid) AM–SM strategy. This work focused on HM process planning based on feature extraction and knowledge interpretation. In a subsequent study [79], they investigated the environmental impact of the proposed remanufacturing strategy compared with traditional approaches (material recycling, casting, and machining). Liu et al. [92] developed a design-for-remanufacturing method under a level-set framework, which provides a solution for upgrading broken parts.

## 2.3.2 Process Planning for Subtractive, Additive and Hybrid Manufacturing

Design and manufacturing are two critical phases for product development, and process planning plays an important role in the link between design and manufacturing processes. Process planning accomplishes the tasks of a selection of operation processes, determination the sequence of operations. Most process planning systems for machining are based on feature techniques [93]. The feature-based techniques examine the topology and geometry of a part and determine its definitions under the feature concept. To achieve this, a design model of lower-level entities (lines, points, etc.) is transformed into a feature model of a higher-level entity (holes, pockets, etc.). It leads a machining operation to be an intermediate or final state of a machining feature. In order to perform process planning, several skills are required from process planners, such as understanding the requirements for the manufacturing parts, the interactions between part, manufacturing, quality and cost, knowing machine tools [94]. However, in the modern manufacturing industry, it is very challenging to find a skilled labour force in process planning. Based on this motivation, the automated process planning in machining has been developed in the last three decades [93–100], with typical studies lying on tool selection [98,101,102], setup and fixture planning [103–105], selection of and sequencing operations [94,95,99], and determining machining precedence [100].

Process planning for AM has been concentrated on recently. Unlike the machining process, the AM process generally is a single operation with building part layer-by-layer. Therefore, the issues including tool selection and sequencing in the machining process are not existing in the AM process. The AM process does not require skills for the operator in terms of planning as a machining process. Whereas, with the involvement of support structures, the building direction and tool-path planning are more crucial in the AM process, which has a significant effect on building time and building quality. Most AM process planning research has focused on build direction optimization [106–108] and tool-path planning [109,110].

Recently, HM has gained significant attention, which combines AM's advantages of building complex geometries and SM's benefits of dimensional precision and surface quality. HM is creating huge opportunities in the design and manufacture of the finished part, and also in remanufacturing and repairing of high-value components [111]. It has the ability to add and remove materials that help to address different geometrical challenges, such as internal and overhanging structures, and the part with a high 'buy-to-fly' ratio [112].

Table 2.1: Commercial hybrid machines from industry.

| Product | Company | Additive process | Subtractive process | Ref. |
|---|---|---|---|---|
| Ambit™ | Hybrid Manufacturing Technologies | Directed energy deposition | 5-axis CNC milling | [113] |
| LASERTEC 65/125/4300 3D hybrid | DMG MORI | 5-axis direct energy deposition | 5-axis CNC milling | [114–116] |
| INTEGREX i-400S AM | Mazak | Directed energy deposition | 5-axis CNC milling and turning | [117] |
| VC-500A/5X AM HWD | Mazak | 5-axis hot wire deposition | 5-axis CNC milling | [118] |

| | | | | |
|---|---|---|---|---|
| CybaCast Hybrid | Cybaman Technologies | 6-axis laser powder deposition | 6-axis CNC milling | [119] |
| WFL Millturn | WFL Millturn Technologies | Laser powder deposition | 5-axis CNC turning | [120] |
| MPA 40 | Hermle | 5-axis laser powder deposition | 5-axis CNC milling | [121] |
| OPM250 | Sodick | Laser metal sintering | CNC milling | [122] |
| LUMEX Avance-25/60 | Matsuura | Powder bed fusion | CNC milling | [123,124] |

Table 2.1 lists the commercial hybrid additive-subtractive machines from the industry. It worth to mention that only integrated hybrid machine in a single platform is discussed here and the HM processes which are performed in sperate machines are more common in the industry [111,125]. The HM configurations from academic research are summaries from [111] (see Figure 2.3). The figure shows that SM operations are limited to CNC machining. Similar to industrial machines, the DED process dominates the AM processes, with a small case of PBF and material extrusion. From an academic perspective, it can be witnessed that these systems are largely built upon the existing commercial CNC machine tools, with adaption in the form of DED technologies integration.

HM hardware technologies are striding ahead, however, the process planning tools to support their incredible potential are falling behind [126]. Some commercial process planning software has already been used in industrial hybrid systems, such as Siemens NX used in DMG MoriSeiki, LaserTec 65 3D, and hyperMill used in Replicator and Cybaman [111]. The major limitation of these commercial tools is the poor support for automation. For example, AM and SM feature recognition is manually conducted that highly relies on the user's knowledge. The consequence is that the process planning of complex remanufacturing problems is very tedious, and the quality of the derived process plan can hardly be evaluated. Therefore, the HM rules are not integrated into these software tools.
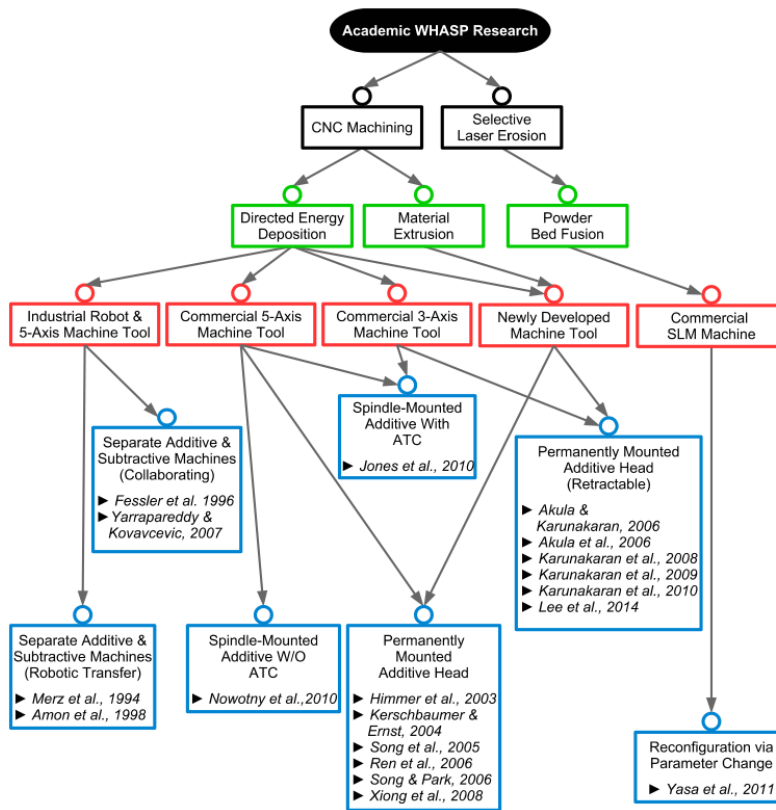
Figure 2.3: A breakdown of the hardware configuration (from academic research [111]).

In recent years, researches have drawn attention to process planning for the HM process. Manogharan et al. [127] introduced an HM process planning method that integrated a visibility analysis of machining, sacrificial fixturing technology for electron beam melting, and tool-path planning. Joshi & Anand [128] presented a novel method for decision-making among AM, SM, and HM, along with optimal part decomposition, where the objective is to minimize manufacturing complexity. Chen et al. [129] observed that complex AM components might have the tool accessibility issue, in which the cutter cannot access the part's interior. They then developed an optimization algorithm for HM process planning, which derived the optimal HM process plan of an arbitrary geometry that was free of machinability issues. Kerbrat et al. [130] developed a new design-for-manufacturing approach, combining AM and SM in a hybrid modular vision. In their work, manufacturability indices were evaluated from the design parameters (geometry,

21

dimensions, material information, and specifications) of the part CAD model. These indices led to the decision on the structural features to be manufactured by AM or SM. Zhu et al. [131,132] and Newman et al. [9] presented a hybrid process planning tool entitled iAtractive, combining CNC machining, fused filament fabrication, and inspection process for complex plastic components including internal structures. The inspection was integrated with the AM and SM operations to provide a closed-loop for the in-situ process plan update. Behandish et al. [126] developed an HM process planning approach that formulated HM processes through logic representations. The method could enumerate all the possible sequences of processes to find the optimal process plan. Recently, ElMaraghy & Moussa [133] presented a method of process planning for HM that included manual feature extraction, product platform design, and process determination.

An increasing level of development in research on HM-based repairing technology has been witnessed by those publications. However, in terms of remanufacturing, there are comparatively fewer studies. In comparison with repairing, remanufacturing requires more decision-making support since the process planning result is not unique, and AM and SM feature extraction relies on algorithms for the automation process. Among the few reported efforts, Newman et al. [9] and Zhu et al. [91] features a remanufacturing framework that consisted of fused filament fabrication, CNC machining, and inspection. The method enabled the remanufacturing of an existing part or even a recycled and legacy part into a new part with new functional features. Le et al. [88] proposed an HM process planning for remanufacturing based on feature extraction and knowledge interpretation. In a subsequent study, they have extended the process planning framework by discussing the environmental impact of the proposed remanufacturing strategy compared with traditional approaches (material recycling, casting, and machining). Liu et al. [134] developed a novel design-for-remanufacturing method under a level-set framework, which provides a solution for upgrading broken parts.

### 2.3.3 Feature modeling for Hybrid Manufacturing

Feature-based technologies have been used successfully for years in computer-aided process planning (CAPP) for the machining process [93]. Feature-based technologies play an important role to bridge CAD and computer-aided manufacturing (CAM). This section offers a review of feature-based implementation in process planning for HM.

Geometric representation modelling is an essential task for feature-based modelling since it stores geometric information of the model. In geometric modelling, constructive solid geometry (CSG) and boundary representation (B-rep) are widely adopted. With CSG modelling, a physical object can be decomposed into multiple primitives and a sequence of Boolean operations. With the B-rep method, the solid is bounded by a set of closed and directional faces, which are bounded by edges and vertices. CSG modelling has the merits of supporting efficient Boolean operations and topology optimization [135]. The B-rep format model is dominant in the machining feature recognition field because it uniquely defines the faces and their topological patterns [136]. However, it has issues to deal with numerical calculations between two solid parts by adopting B-rep models. CSG format shows its potentials in the calculation in multiple solid models. However, to the author's best knowledge, no research works are having to explore the implementation of CSG models for feature extractions for HM or HM in remanufacturing.

The concept of feature-based technology-aided process planning for HM has emerged in recent years [9,88,130,137,138]. Since SM removes material from the part in essence, the definition of SM feature in HM process coincides with the machining feature. In term of AM, from [88], the AM feature is defined as a geometrical shape with associating attributes including geometrical form and dimensions, build directions, starting surface, material, and tolerance. Further, manufacturing rules were applied to associate AM and machining (SM) features to generate the process planning for HM, which is illustrated in Figure 2.4. AM and SM features could also be distinguished to improve manufacturability. Kerbrat et al. [139] developed a hybrid and modular approach to achieve the explicit separation, shown in Figure 2.5. In their research, a CAD model is decomposed into

subtractive and additive modules which is associating with attributes with the dimension, operation direction, and also manufacturability. On top of that, the cost model [140] and the environmental impact model [79] were also investigated to enrich AM and SM features in HM. With the seminal works of proposing the concept of AM and SM in HM, the process planning for HM are becoming similar to the framework of CAPP in the machining process. However, unlike the scenario in machining, process planning for HM is still lacking the algorithm's support for the automation process. Although Le et al. [137,138] proposed the feature extraction method for HM in a remanufacturing context, the approach is highly relying on human intervention. Besides, the collision issues in HM remanufacturing are rarely discussed in the previous studies. In CAPP for machining, feature recognition is an important process of reinterpreting a design model for automating manufacturing operations [136]. Previous works on feature recognition/extraction in machining process planning have been developed for three decades [136,141]. However, it is very challenging to implement these prosperous techniques in the HM or HM for remanufacturing. The main research gap is that the geometrical representation which is widely utilized in machining is difficult to apply in the framework of HM for remanufacturing.
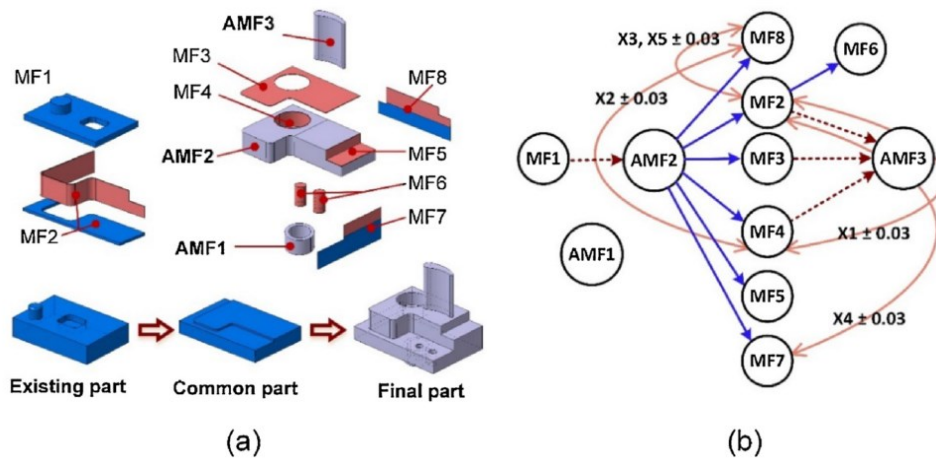


Figure 2.4: Process planning for HM by AM and SM feature-based method: (a) machining features (MFs) and AM features (AMFs) extraction; (b) associations between MFs and AMFs (from academic research [88]).
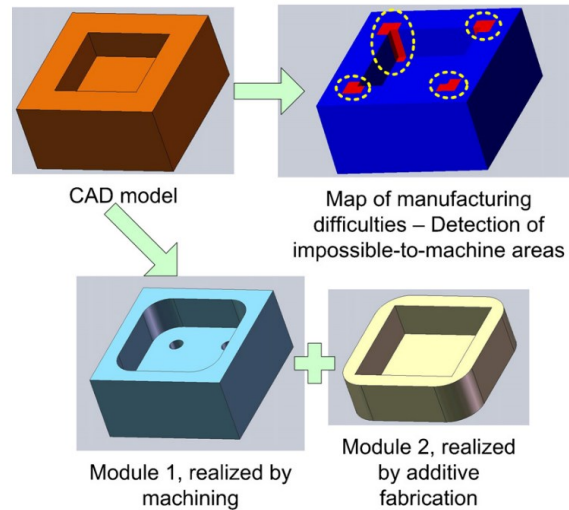
Figure 2.5: Explicit separation of additive and subtractive modules in reducing manufacturing difficulties (from academic research [130]).

## 2.3.4 Summary of the Hybrid Manufacturing for Remanufacturing/Repairing

HM leverages AM's strengths of forming complex geometries and SM's benefits of dimensional precision and surface quality control. This technology shows great potential to support repairing and remanufacturing processes. parts or remanufacture them to new features and functionalities. However, process planning for hybrid remanufacturing is still a challenging research topic. This is because current methods require extensive human intervention for feature recognition and knowledge interpretation, and the quality of the derived process plans are hard to quantify. Besides, other than addressing the process planning rules, little effort has been spent on critical decision-making in the variety of feasible process plans (e.g., finding out the most economical solutions). The concept of AM and SM features was proposed recently, whereas the automation algorithm for feature extraction is missing. Also, the geometric representations are rarely explored for HM or HM in the remanufacturing context.

# Chapter 3: A Novel Deep Learning-based Damage Detection and Localization for Remanufacturing and Repairing

## 3.1 Overview

Although significant benefits can be gained from remanufacturing/repair, there are still numerous challenges to implement it in the industry. The main reason is that, compared to the manufacturing process, stochastic returns of used parts and their uncontrollable quality condition result in a high degree of uncertainty for the remanufacturing and repairing process [6]. The uncertainty surrounding the return of the parts complicates the remanufacturing process. Recently, significant efforts have been devoted to the remanufacturing process plan optimization with uncertainties [2,7]. These optimization frameworks are initialized with characterized and quantified fault features (e.g. crack, dent, scratch, abrasion). The visual or manual inspection determines the fault feature characterization, which indicates damage type, damage location. These two factors play a key role in generating an optimal process plan with different additive operations and subtractive operations with heuristic algorithms. The current visual or manual inspection methods require extensive human intervention, and the quality of the process is hard to be stable. Therefore, an automated inspection approach for remanufacturing/repairing is urgently demanded. For this reason, an increasing level of interest in research on the automated or semi-automated inspection for remanufacturing or repair has been witnessed over recent years, which are reviewed in Section 2.1. By summarizing these research results, to the best of the author's knowledge, an automatic approach that enables damage recognition and spatial localization simultaneously for remanufacturing/repairing has not been discovered. In this chapter, a deep learning-based damage recognition and spatial localization method is introduced, which can classify different damage features and localize in the global three-dimensional coordinate. The localization results show 10% errors and much faster speed compared with the traditional 3D scanning method. The

26

proposed method provides a promising application with a hybrid image and 3D scanning method which can roughly localize the damage and the 3D scanner can approach the target area to acquire a fine scanning result, which will strongly reduce the time for acquisition of point clouds of the damaged area.

## 3.2 Methodology

The main objective of this study is to automatically detect damages from a damaged part. The study proposes a detection strategy based on a deep-learning technique to recognize and localize damages. The flowchart is shown in Figure 3.1. There are three main steps of the process: (1) Data acquisition for the RGB image and depth data by a depth camera; (2) the damage recognition and segmentation using a Mask-RCNN method, providing damage segments with recognized damage type; (3) the localization of the damage determined by the integration of damage segments and a point cloud from the depth data.
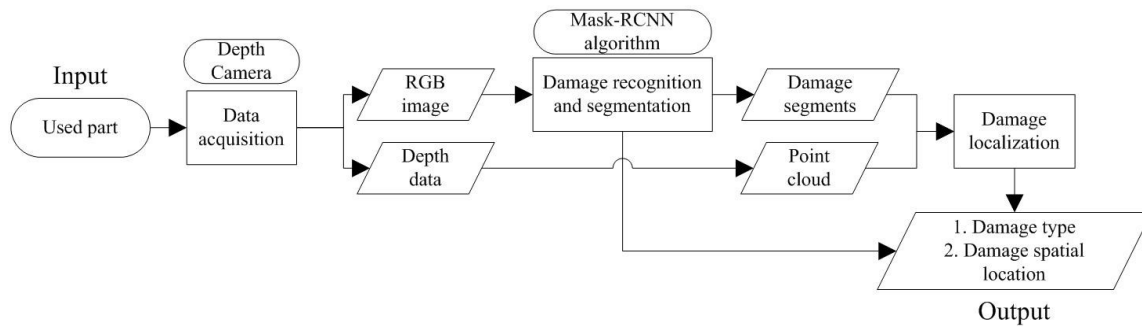


Figure 3.1: The flowchart of the proposed method.

### 3.2.1 Damage Recognition and Classification

In this study, the damage recognition and segmentation method is based on a Mask-RCNN architecture [51]. The proposed damage recognition and segmentation method is illustrated in Figure 3.2. As shown, it is composed of four modules: (1) Input the original image to be processed into a pre-trained convolutional backbone to extract features and to obtain a feature map; (2) the region proposal network (RPN) proposes region of interest (RoI) in the feature map with a set of rectangular object proposals; (3) each RoI generates a fixed-size feature map by RoIAlign layer; (4) the fixed-size feature map goes through

27

two branches of layers for objective classification, frame regression and pixel segmentation.
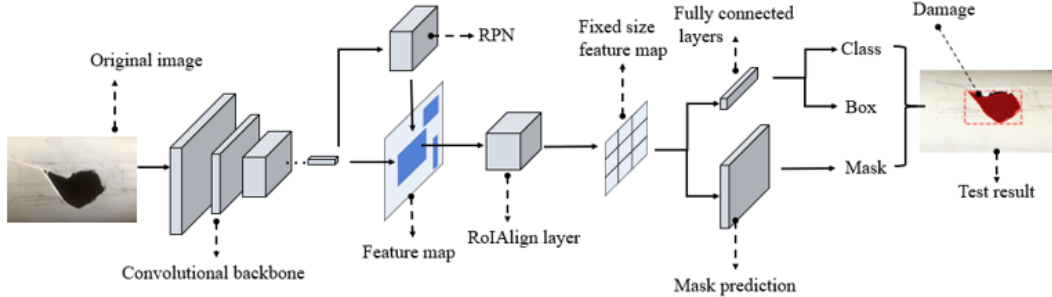


Figure 3.2: The neural network architecture of the proposed damage recognition and segmentation method.

The convolutional backbone is composed of a series CNN to extract feature maps from the image. The properties of a neural network backbone are characterized by the selection and arrangement of different layers. Deeper networks generally allow to extract more complicated features from the input image, meanwhile stacking more layers will result in issues for training, due to the degradation problem. The residual network (ResNet) was designed to address this problem in deeper neural networks (up to 152 layers) [142] by reformulating its layers as residual learning function regarding the layer input.

Generally, the Mask RCNN model adopts ResNet101 as the backbone. It is a very deep network with 101 layers and approximately 27 million parameters. In this study, because the damage category is simple and the dataset is limited, a smaller backbone ResNet50 is used to improve the running speed for training. Feature pyramid network (FPN) [143] uses a top-down architecture with lateral connections to build an in-network feature pyramid, which addresses the multi-scale object recognition problem. Overall, this study uses the combination of ResNet50 and FPN as the backbone for feature extraction.

The second module in the proposed damage detection and recognition is RPN. The original image passes through the ResNet50 and FPN convolutional network and outputs a set of convolutional feature maps. In this study, the algorithm uses nine different sizes

of anchors as (128*128, 256*256, 512*512) with aspect ratios of (1:1, 1:2, 2:1). Positive or negative anchors are computed by considering the interest-over-union (IoU) between the analyzed anchor and ground-truth bounding boxes on the image. The IoU is calculated by Equation (3-1). In this research, positive anchors are those that have an IoU is greater or equal to 0.7 in any ground-truth object, and negative anchors are those that have IoU is smaller or equal to 0.3. The anchors with IoU between 0.3 and 0.7 are not considered for the training objective. The positive anchors are then processed to the proposal classification.

$$\text{IoU} = \frac{A_{overlap}}{A_{union}} \qquad (3\text{-}1)$$

where $A_{overlap}$ is the area of overlap and $A_{union}$ is the area of union.

The multi-tasking loss function of the Mask-RCNN training process is defined in Equation (3-2), where $L$ is the total training loss; $L_{cls}$ is the classification loss, $L_{box}$ is the bounding-box loss, and $L_{mask}$ is the mask loss.

$$L = L_{cls} + L_{box} + L_{mask} \qquad (3\text{-}2)$$

The variables for $L_{cls}$ and $L_{box}$ are defined in [144], as shown in Equation (3-3). Each training RoI is labelled with a ground-truth class $u$ and a ground-truth bounding-box regression target $v$.

$$L_{cls} + L_{box} = L_{cls}(p, u) + \lambda[u \geq 1]L_{loc}(t^u, v) \qquad (3\text{-}3)$$

where $u$ is the label of each training RoI with a ground-truth class; $v$ is a label of each RoI with a ground-truth bounding-box regression target; $t^u = (t_x^u, t_y^u, t_w^u, t_h^u)$ specifies a scale-invariant translation and log-space height/width shift relative to $u$ class; $p = (p_0, \dots, p_K)$ represents the probability distribution over $K + 1$ categories; $[u \geq 1]$ denotes the Iverson bracket indicator function that evaluates to 1 when $u \geq 1$ and 0 otherwise.

The bounding-box regression $L_{loc}(t^u, v)$ is shown in:

$$L_{loc}(t^u, v) = \sum_{i\in\{x,y,w,h\}} \text{smooth}_{L_1}(t_i^u - v_i)$$ (3-4)

where:

$$\text{smooth}_{L_1}(x) = \begin{cases} 0.5x^2 & \text{if } |x| < 1 \\ |x| - 0.5 & \text{otherwise} \end{cases}$$ (3-5)

The $L_{mask}$ is calculated by taking the average cross-entropy of all pixels on the RoI, as:

$$L_{mask} = -\frac{1}{N}\sum [y_i \ln a_i + (1 - y_i)\ln(1 - a_i)]$$

$$y_i = 1/(1 + e^{-x_i})$$ (3-6)

$$a_i = 1/(1 + e^{-b_i})$$

where $x_i$ and $b_i$ are the prediction value and true value of the $i$-th pixel in the positive RoI, respectively, $N$ indicates the number of pixels in the positive RoI.

### 3.2.2 Spatial Localization

Spatial localization of the damaged area is achieved by finding the mapping relations between the 2D coordinates in the image and 3D spatial coordinates by the depth sensor model, as shown in Equation (3-7).

$$z_c \begin{bmatrix} u \\ v \\ 1 \end{bmatrix} = \begin{bmatrix} \dfrac{f_x}{dx} & 0 & u_0 \\ 0 & \dfrac{f_y}{dy} & v_0 \\ 0 & 0 & 1 \end{bmatrix} [R_z R_y R_x \quad T] \begin{bmatrix} X \\ Y \\ Z \\ 1 \end{bmatrix}$$ (3-7)

where:

$$R_x = \begin{bmatrix} 1 & 0 & 0 \\ 0 & \cos\theta_x & -\sin\theta_x \\ 0 & \sin\theta_x & \cos\theta_x \end{bmatrix}$$

$$R_y = \begin{bmatrix} \cos\theta_y & 0 & \sin\theta_y \\ 0 & 1 & 0 \\ -\sin\theta_y & 0 & \cos\theta_y \end{bmatrix} \tag{3-8}$$

$$R_z = \begin{bmatrix} \cos\theta_z & -\sin\theta_z & 0 \\ \sin\theta_z & \cos\theta_z & 0 \\ 0 & 0 & 1 \end{bmatrix}$$

$$T = \begin{bmatrix} t_x & t_y & t_z \end{bmatrix}^{\mathrm{T}}$$
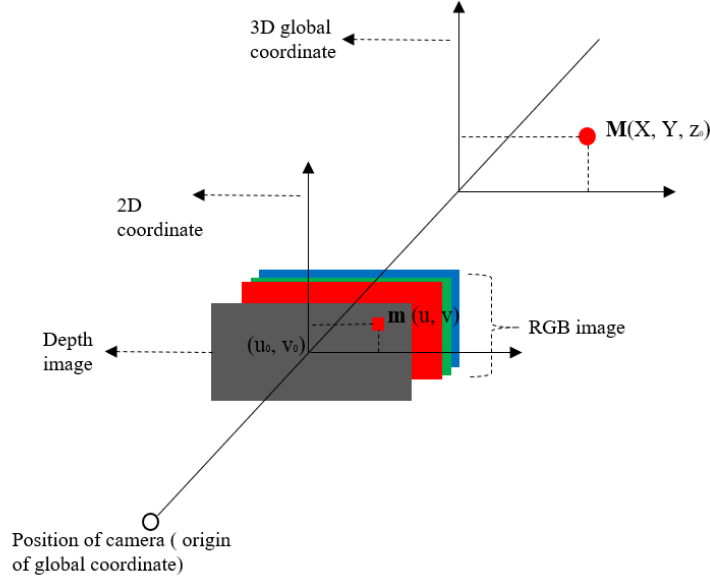


Figure 3.3: An illustration of the mapping of depth and RGB image coordinate to xyz coordinate.

$u$ and $v$ are the 2D image coordinates; $u_0$ and $v_0$ are the origin of the 2D coordinate system; $f_x$ and $f_y$ are the focal length along $x$ and $y$ direction, respectively; $dx$ and $dy$ are scale factors on $x$ and $y$ direction; $R_z R_y R_x$ and $T$ are the rotation matrix and translation matrix from the camera coordinate system to the global coordinate system, $X$ , $Y$ , $Z$ are

the 3D coordinates under global coordinate. **M** and **m** represent the location of the pixel in 3D global coordinate and image, respectively. $z_c$ is the distance of the image to the camera. The illustration is shown in Figure 3.3.

To simplify this problem, the study coincide the camera coordinate system and the global coordinate system and Equation (3-9) can be derived as:

$$z_c \begin{bmatrix} u \\ v \\ 1 \end{bmatrix} = \begin{bmatrix} \dfrac{f_x}{dx} & 0 & u_0 \\ 0 & \dfrac{f_y}{dy} & v_0 \\ 0 & 0 & 1 \end{bmatrix} \begin{bmatrix} 1 & 0 & 0 & 0 \\ 0 & 1 & 0 & 0 \\ 0 & 0 & 1 & 0 \end{bmatrix} \begin{bmatrix} X \\ Y \\ Z \\ 1 \end{bmatrix} \tag{3-9}$$

Then, the 3D coordinates of the damaged area can be calculated as:

$$X = \frac{(u - u_0) z_c dx}{f_x}; Y = \frac{(v - v_0) z_c dy}{f_y}; Z = z_c \tag{3-10}$$

## 3.3 Experimental Results and Analysis

### 3.3.1 Transfer Learning

Deep learning requires a large number of input images as training data, but for some applications, it is very difficult to find enough images. Transfer learning provides an alternative strategy to address this problem. It is possible to reuse a pre-trained CNN weight as a starting point for another training task, instead of building a CNN from scratch. In this study, the training model was initialized using the weights from a ResNet-101 network, which was trained on the COCO dataset [145]. COCO dataset has 330K images with 1.5 million object instances for 80 object categories. Therefore, a good performance pre-trained model can be obtained from this dataset. Using migration learning from the pre-trained model can increase the efficiency of training significantly than starting from scratch.

## 3.3.2 Dataset Building

The images with damaged pipes were collected by a GigE DFK 33GD006 image sensor with TCL 3520 5MP lens with a 35 mm focal length, and the setup is shown in Figure 3.4. The entire dataset includes training, validation and testing datasets with the resolution of 1920*1080 images. The dataset is collected from 30 damaged pipes and each pipe has 3 portions of damage with different sizes. The experiment collected 220 images (160 for the training dataset, 40 for validation dataset and 20 for testing dataset). The training and validation images were annotated according to their damaged areas by polygon shapes using the free annotation software VGG Image Annotator [146]. It labelled the images with the JSON file which contains a class of damage and damage region. Figure 3.5 gives examples of annotated images.



Figure 3.4: Dataset acquisition setup.



a

b
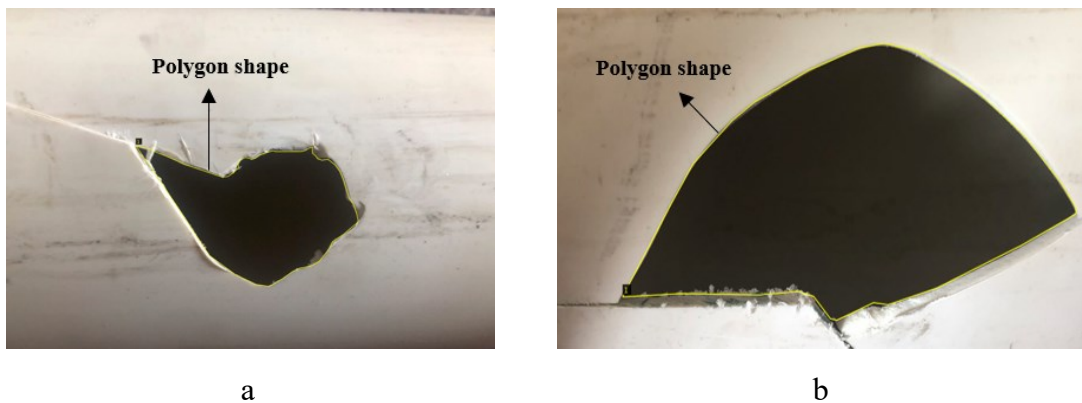
Figure 3.5: Annotation of damaged areas by polygon shapes.

### 3.3.3 Experimental Environment

The experiments were conducted using Mask-RCNN, Matlab2019a, CUDA 10.0, TensorFlow 1.14.0, CuDNN 6.5 on a desktop computer equipped with an Intel Core i5-8600K 3.60 GHz CPU, 16 GB DDR4 RAM, Nvidia GTX 1060 with 6 GB video ram GPU, under an operating system of Ubuntu 16.04 64 bit. The pre-defined parameters for the damage detection and classification model are shown in Table 3.1.

Table 3.1: The pre-defined parameters for damage detection and classification.

| Parameter | Value |
|---|---|
| Batch size | 30 |
| Learning rate | 0.01 |
| Learning Momentum | 0.9 |
| Mask pool size | 14 |
| Pool size | 7 |
| Step per epoch | 200 |
| Detection minimum confidence | 0.9 |
| Number of classes | 2 |
| epoch | 30 |

In this study, Microsoft Kinect V1 was used as the depth camera for testing. The technical specification of it is presented in Table 3.2. It outputted RGB image (640*840*3) and depth image (640*840), as shown in Figure 3.6.

Table 3.2: The pre-defined parameters for damage detection and classification.

| Kinect V1 | Specifications |
|---|---|
| Max. resolution of the colour sensor | 1280*960 |
| Max. resolution of the depth sensor | 640*480 |
| Viewing angle | 43° vertical x 57° horizontal |
| Vertical tilt range | ±27° |
| Frame rate | 30 frames per second (FPS) |

Figure 3.6: RGB image (a) and depth image (b).

By implementation of the Equation (3-9), the point cloud data (defined as *pointcloud*) was calculated from the RGB image and depth image, as shown in Figure 3.7. The data structure of *pointcloud* includes *Location* (480*640*3), *Color* (480*640*3), *Count* (positive integer), *XLimits* (1*2), *YLimites* (1*2), *ZLimites* (1*2). In the data of Location, each entry specifies the x, y, and z coordinates of a point in the 3D coordinate space. Therefore, each pixel in the RGB image can be mapped to the *pointcloud.Location* to find their x, y, z coordinates in the 3D space.
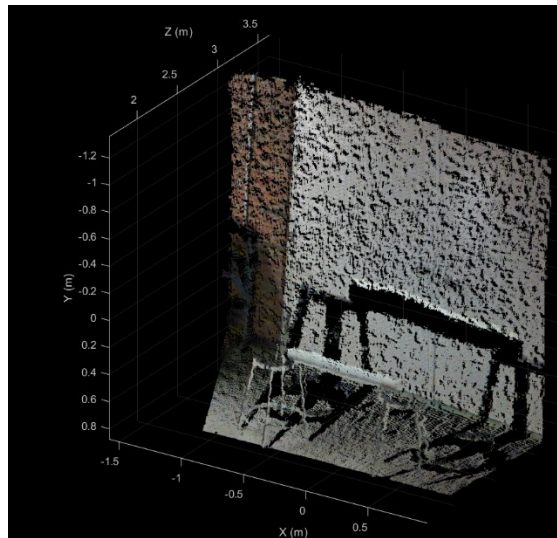


Figure 3.7: Point cloud dataset.

35

### 3.3.4 Results and Analysis

For the damaged area detection and classification algorithm, after 30 epochs of training, the convergence history of the model loss for both training and validation samples are plotted in Figure 3.8. It can be observed that the loss for training and validation achieved 0.1612 and 0.5744, respectively. The accuracies in this study were in segment-wised evolution. The average precision had achieved 99.57% and 87.61% for training and validation datasets. Considering the size of the training dataset, the validation accuracy is acceptable. Different hyperparameters have been tried in this study such as batch size, learning rate, and the activation function to improve the performance of the model but achieved limited benefit. Therefore, in this study, increasing the size of the training dataset would be the most effective method to improve the accuracy further. Some examples from the damaged area detection algorithm are shown in Figure 3.9.

The performance of the 3D localization in the proposed method was tested by calculating the centroid position of the damaged area. The localization error is defined as follows:

$$\Delta = \sqrt{(x_i - x)^2 + (y_i - y)^2 + (z_i - z)^2} \qquad (3\text{-}11)$$

where $x_i$, $y_i$ and $z_i$ are the coordinate of the estimated centroid position; and $x$, $y$ and $z$ are the coordinates of centroid position from manual measurements.

The average relative error is defined as:

$$\sigma = \frac{\sum_{i=1}^{n} \Delta_i}{n\sqrt{x^2 + y^2 + z^2}} \qquad (3\text{-}12)$$
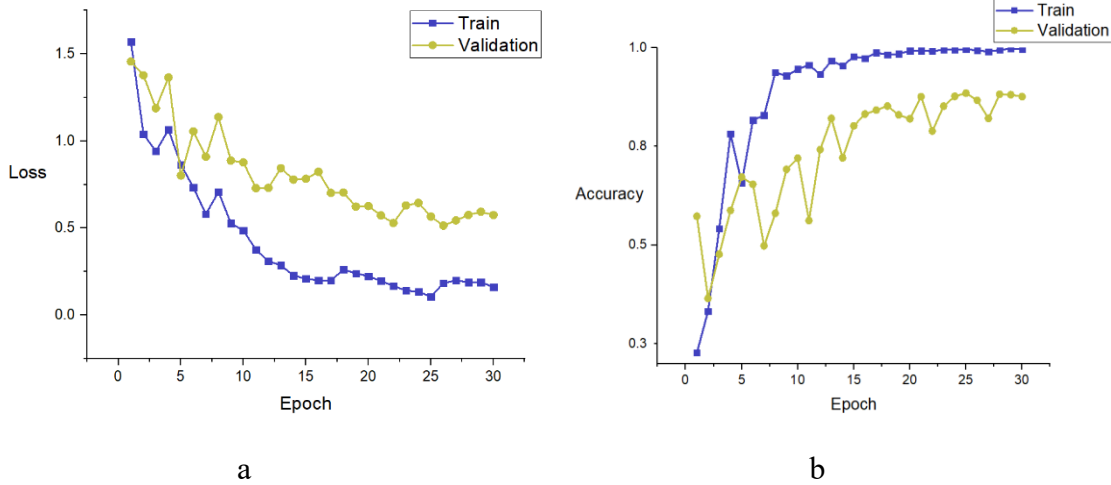
Figure 3.8: Convergence histories for loss (a) and accuracy (b) after 30 epochs.
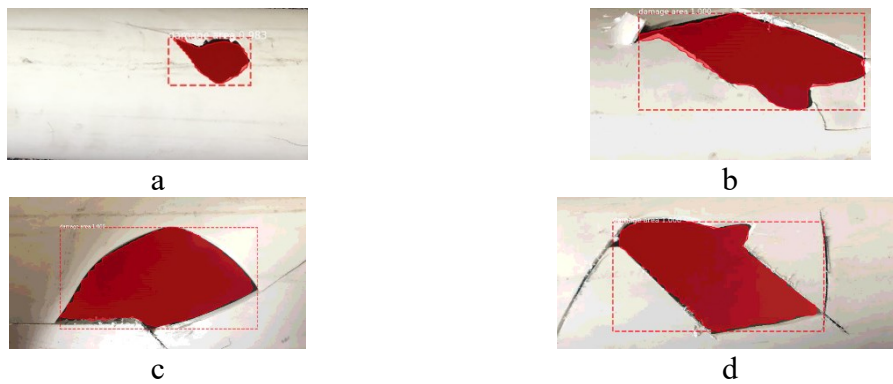


Figure 3.9: Example detections of the damaged area from the pipes.

By conducting measurements for five samples, the manual measurement of the centroid point, estimation of the centroid position by the proposed method were recorded. For each sample, the estimation of the centroid position was calculated by ten times. The results are presented in Table 3.3. From [18], the proposed had achieved higher error than the traditional damage localization method (around 5 mm). However, the traditional damage localization approach costs a few hours in scanning and around 2000 s for registration. Therefore, the proposed method represents a much higher efficiency than the traditional method. The resolution of the depth sensor impacts the accuracy of the results strongly. High-accuracy 3D depth sensor (such as 2540*1600) can be easily used in this study to

acquire a lower error of the damage area localization, which will be revealed in the future work.

Table 3.3: Results of experiments for the 3D localization.

| # | Manual measurement (cm) | Average estimation (cm) | Average speed (s) | Average Error (cm) | Maximum Error (cm) | Relative error (%) |
|---|---|---|---|---|---|---|
| 1 | (8.2, 2.2, 20.1) | (8.8, 2.4, 20.8) | 1.45 | 0.943 | 2.211 | 4.322 |
| 2 | (20.6, 6.8, 20.7) | (19.2, 6.0, 22.2) | 1.48 | 2.202 | 4.131 | 7.344 |
| 3 | (10.2, 4.2, 23.2) | (12.2, 4.8, 25.2) | 1.42 | 2.891 | 3.681 | 11.253 |
| 4 | (16.3, 2.3, 33.2) | (16.5, 2.3, 35.2) | 1.48 | 2.010 | 4.212 | 5.424 |
| 5 | (10.4, 20.2, 18.8) | (11.4, 21.8, 19.8) | 1.47 | 2.135 | 3.068 | 7.244 |

## 3.4 Conclusion

Remanufacturing/repairing has been considered a green manufacturing strategy since it reduces cost, energy, material consumption and air pollution significantly compared to traditional manufacturing. Damage detection is the primary step in remanufacturing to decide a remanufacturing strategy. However, the current damage detection method relies heavily on manual operations which is time-consuming. The motivation of this study is developing a novel damage detection approach, which performs damage classification and 3D localization simultaneously.

To address these problems, this study proposes an efficient deep learning-based damage detection and localization method. In the first step, the RGB image and depth image are acquired by a depth camera. Then, training data and validation data are collected to train the Mask-RCNN-based model to obtain optimized weight. The RGB image acquired processed in the damage recognition and segmentation algorithm, providing damage

segments with recognized damage types. In the last, the 3D position of the damage is determined by the integration of damage segments and a point cloud from the depth data.

The accuracy of the damage detection can be improved by increasing the training data size. And, the error of damage localization can be reduced by implementing a high-accuracy depth sensor, which will be the focus of future work.

The current remanufacturing/repair industry relies on visual inspection to determine the damage type, damage location and damage degree to schedule the process plans. The study has the potentials to perform damage detection to output the damage type, and location. In future work, a systematic method to determine the damage degree can be investigated.

# Chapter 4: A Primitive-based Damaged Model Reconstruction Method for Repairing processes

## 4.1 Overview

In the AM-based repairing process, a critical preparing step is to localize the defect region and determine the repair volume. The localization can be performed by comparing the scanned 3D digital model with the nominal CAD model. However, a general situation is that the nominal CAD model is not available due to confidentiality issues [59]. This makes the reconstruction of the broken part back to the original status quite non-trivial, and there are a few publications in this aspect [13,18]. Therefore, a novel reconstruction method is proposed in this chapter based on primitive surface fitting. This reconstruction is focused on mechanical components that are composed of only primitive features (e.g., plane, cylinder, sphere, cone) because 95% of mechanical components are able to be approximated by primitive features [147]. These involve multiple procedures of this reconstruction. 3D scanning is performed first to acquire the point cloud data of the broken part. Then, the point cloud is modified by identifying and eliminating the points from the damaged regions. The modified point cloud data is fitted by different primitive surfaces using the proposed surface fitting algorithm so that the damaged area can be restored into a primitive surface. Therefore, the reconstruction is completed by deriving a primitive feature-based CAD model as the outcome. The defective volumes can then be trivially localized and quantified by registering the reconstructed CAD model and the defective point clouds. The main contribution of this chapter lies in the new method to reconstruct complex geometric models with defects. This chapter proposes a novel StepRANSAC algorithm integrated with a SDM to improve the precision and robustness of surface fitting. The novel method for surface fitting performs the main direction determination and primitive segmentation by StepRANSAC to increase the robustness compared with the basic random sample consensus (RANSAC) method, especially for the incomplete

scanning data. Meanwhile, the accuracy of surface fitting is strongly enhanced by using SDM algorithm for refitting.

## 4.2 Methodology

A flowchart of the method is illustrated in Figure 4.1. This research is focusing on external damage on the damaged component, and the method will not work for the internal surface damage where lighting cannot approach. The used part is scanned by 3D scanner to acquire point cloud. Then, points inside the damage region are identified and removed from the point cloud. For the remaining points, a novel StepRANSAC algorithm is designed to efficiently and accurately make the segmentation and initial surface fitting. The SDM refitting method is applied to obtain precise parameters of the surface primitives. Finally, modelling operations are performed based on the topological relationship among the primitive surfaces to construct a CAD model. Details about these procedures will be presented in the following sections.
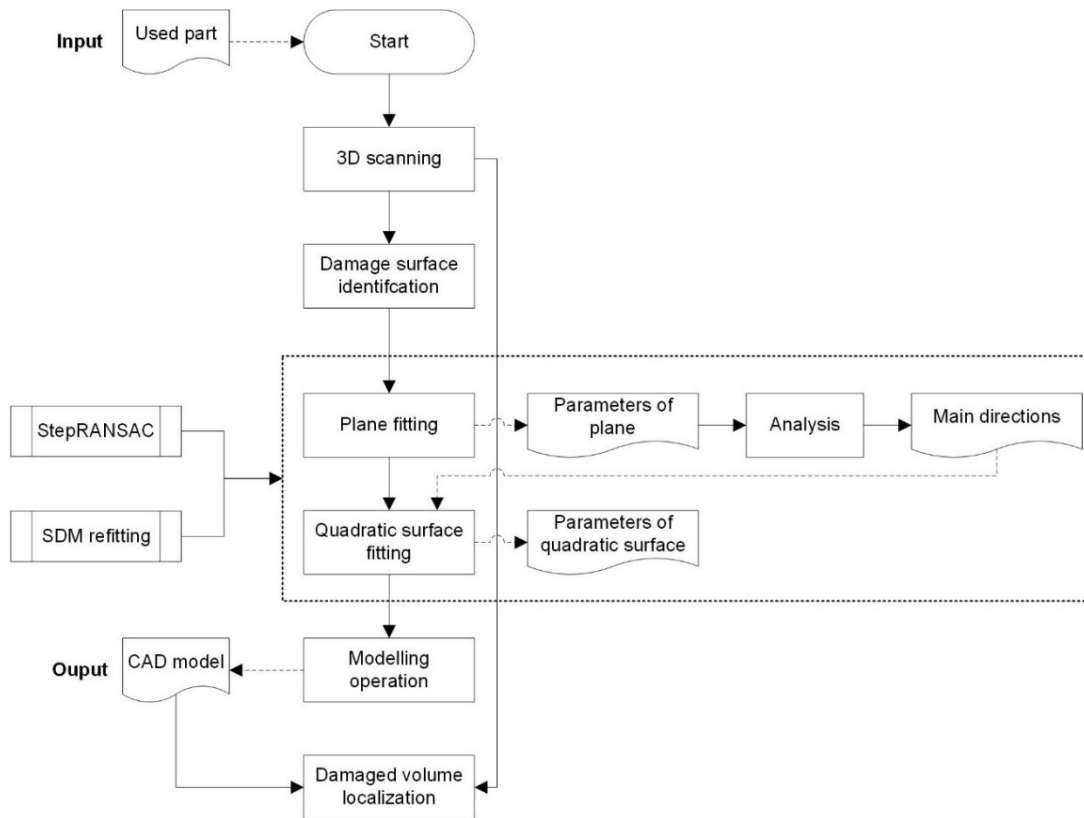
Figure 4.1: A systematic flowchart of the proposed reconstruction method

## 4.2.1 Damage Surface Identification

With the help of 3D scanning techniques, the point cloud is acquired from the used part. Because the defective surface is not smoothly continuous, its Gaussian curvature suddenly increases or decreases in the defective area. Therefore, the damaged region can be identified on the basis of the change of Gaussian curvatures. In this method, the classical principal component analysis (PCA) is adopted for Gaussian curvature estimation [148]. Firstly, the point clouds could be meshed as stereolithography tessellation language (STL) by using commercial CAD software. The curvature of a patch has a difference compared with the curvatures of neighbouring patches. If the absolute value of the difference is higher than a pre-defined threshold, the patch is identified as a defective surface and its corresponding points are recognized as defective points. The defective points are stored in the data set and they are updated through the elimination of the defective points for following the reconstruction process. Figure 4.2 gives an example of defective surface identification from a damaged model.



(a)                                                (b)
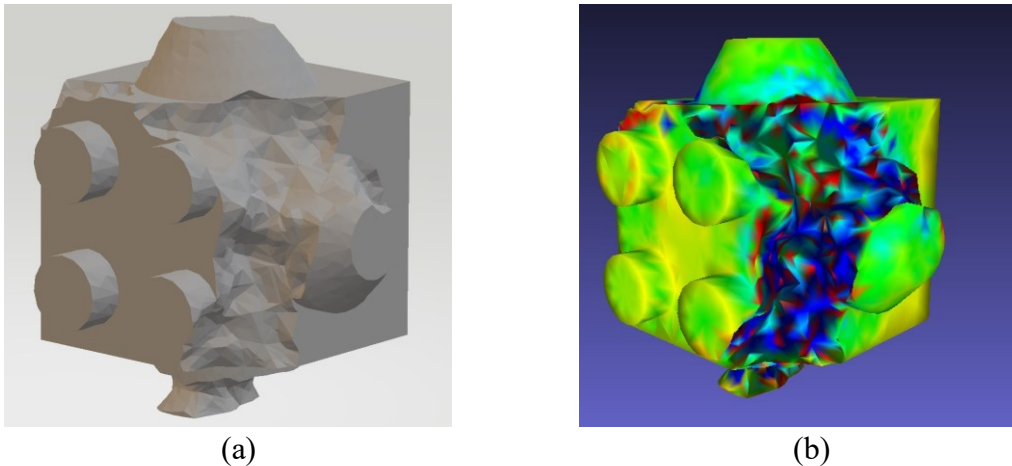
Figure 4.2: (a) A defective model; and (b) surface identification results (the defective surface is distinguished by blue, red and green colour, the intact surface is yellow).

## 4.2.2 StepRANSAC

The RANSAC-based method presents its convenience in its fast calculation in the primitive surface fitting. In the proposed method, a StepRANSAC method is adapted as a prior segmentation and initial estimation for the following refitting. Most of these primitives have their orientations (e.g., normal of plane, axis of cylinder/cone). The orientations have parallel or orthogonal relations with each other, which are called global relations. This main direction confirmation is able to improve the precision of the RANSAC-based method and increase its robustness in noise or incomplete data, especially in the remanufacturing process. In addition, it provides opportunities to decrease the computational expense due to reducing degrees of freedom. StepRANSAC is developed in this method to consider the main directions of a mechanical component. The original RANSAC-based method will be reviewed briefly. Then, after conducting an error analysis of direction estimation for the plane and quadratic surfaces, it can be concluded that error for the plane is much less than that of the quadratic surface. By investigation of the error analysis of the plane and quadratic surface, it could be concluded that the estimation of the normal plane is more reliable for the cylinder/cone axis. Therefore, the planes are detected to estimate the normals. The main directions are determined by solving an optimization problem from normal. Finally, the main directions are employed to guide the cylinder/cone surface fitting.

### 4.2.2.1 RANSAC-based Method

The pseudocode of the RANSAC-based method is presented in Figure 4.3. The input of the algorithm is a point cloud, $P = \{p_i \in \mathbb{R}^3, i = 1, \dots, m\}$. The output $BS$ is a set of parameters of the best shape that is detected, e.g., for cylinder $\{p^*, a, r\}$, where $a$ is the direction of the axis of the cylinder, $p^*$ is a point on the axis, $r$ is the radius.

In the first step, points with minimal numbers that can construct the target shape are randomly selected from the point cloud $P$. These points construct the target shape as a candidate shape. The parameters of the candidate shape are stored in $CS$. In the second

step, algebraic distance (see Equation (4-1)) is calculated as the distance between point clouds and target shape. Then, the number of valid points that have distances is less than the pre-defined threshold $T$ is counted and is stored in $B$. From step 3 to step 6, the better candidate means which have more valid points are accepted in iterations and the best candidate for target shape remains until reaching the maximum iteration times. The parameters of best shape are stored in $\textbf{\textit{BS}}$ and the valid points for the best candidate remain in $\textbf{\textit{VP}}$. It is worth mentioning that the RANSAC-based method has the capability to filter the noises and outliers because only points that have distance below the threshold remain in the process (Figure 4.4).

$$D = \sum_{k=1}^{m} F^2(\textbf{\textit{p}}_k) \tag{4-1}$$

where $F$ is the left-hand side of the implicit representation $F(p) = 0$ of the fitting surface; $\textbf{\textit{p}}_k \in \textbf{\textit{P}}$.

---

**Algorithm 1** RANSAC.

    **Input**: $\textbf{\textit{P}}$: a set of point clouds
    **Output**: $\textbf{\textit{BS}}$: best shape parameters
    $V \leftarrow \textbf{0}$: number of valid points
    **repeat**
        1. $\textbf{\textit{CS}}$=rand($\textbf{\textit{P}}$) ;
        2. $B$=sum(d(CS,$P_i$)<$T$)
        3. **if** $B > V$ **then**
            4. $V \leftarrow B$;
            5. $\textbf{\textit{BS}} \leftarrow \textbf{\textit{CS}}$;
        **end**
    **until** *Reach the maximum iteration times*;
    6. $\textbf{\textit{VP}} \leftarrow$ record($\textbf{\textit{P}}$)

---

Figure 4.3: The pseudocode for RANSAC-based surface fitting.

|   a   |   b   |   c   |
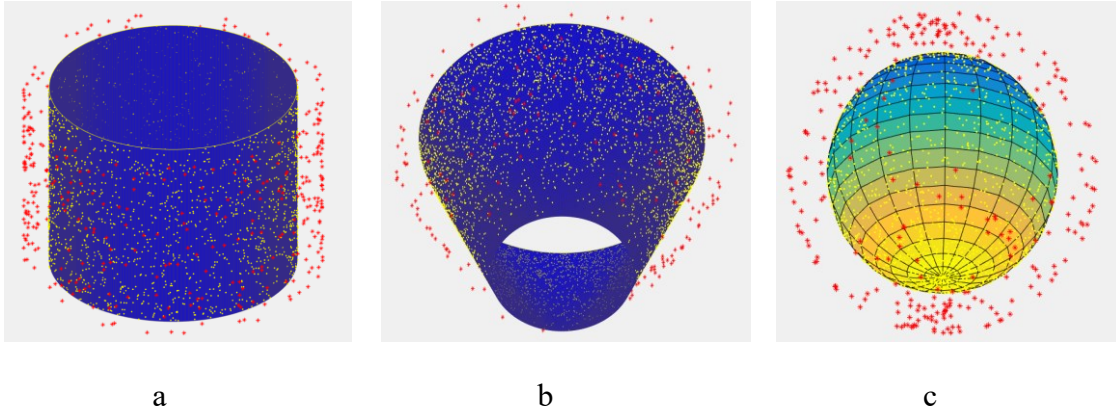
Figure 4.4: (a) RANSAC-based method surface in cylinder fitting; (b) cone fitting; (c) sphere fitting. Valid points (yellow dots) remain and outliers (red stars) are removed in this process.

### 4.2.2.2 Candidate Error Analysis

From the principle of the RANSAC-based surface fitting method mentioned above, point clouds are randomly selected to generate the candidate shape. Then, the distance between the point cloud and the candidate shape is calculated. If the distance falls in the pre-defined threshold, the candidate is determined as a valid shape. The position error is the difference between the real part and scanned point clouds during 3D scanning. Therefore, in the RANSAC-based method, the error is accumulated in shape candidate generation. For different primitive shapes, the quantities of reconstruction errors are not the same.

The position error in measurement of a point $\boldsymbol{p}_i(x_i, y_i, z_i)$ is $\Delta_i(x_\Delta, y_\Delta, z_\Delta)$; error of the normal vector $\boldsymbol{n}_i(nx_i, ny_i, nz_i)$ for this point is $\Delta_{in}(x_\Delta, y_\Delta, z_\Delta)$; The errors in different primitive shapes (plane, cylinder, and cone) construction are investigated in the following sections.

a.  **Plane surface candidate error analysis**: the parameters of a plane can be determined by three points $\boldsymbol{p}_1$, $\boldsymbol{p}_2$ and $\boldsymbol{p}_3$. The point on the plane:

$$\boldsymbol{p}_p = (\boldsymbol{p}_1 + \boldsymbol{p}_2 + \boldsymbol{p}_3)/3 \tag{4-2}$$

The normal vector of the plane:

45

$$n_p = (p_1 - p_2) \times (p_1 - p_3) \qquad (4\text{-}3)$$

The candidate error of plane surface candidate consists of point position error $\Delta_p$ and normal error $\Delta_n$. The point position error:

$$\Delta_p = (\Delta_1 + \Delta_2 + \Delta_3)/3 \qquad (4\text{-}4)$$

The normal error:

$$\Delta_n = \frac{\Delta_1 - \Delta_2}{\|p_1 - p_2\|} \times \frac{\Delta_1 - \Delta_3}{\|p_1 - p_3\|} \qquad (4\text{-}5)$$

The $\|p_1 - p_2\|$, $\|p_1 - p_3\| \gg \Delta_i$; thus $\Delta_i \approx 0$.

b. **Cylinder surface error analysis:** the parameters of a cylinder can be determined by two points $p_1$, $p_2$ and their normal vectors $n_1$, $n_2$.

The direction of axis:

$$n_c = n_1 \times n_2 \qquad (4\text{-}6)$$

The point $p_c$ is the intersection of two parametric lines $p_1 + tn_1$, and $p_2 + tn_2$ projected onto $n_c \cdot p_1$ plane. The radius $r_c$ of the cylinder is the distance between $p_c$ and $p_1$ on the plane. The candidate error of cylinder surface candidate consists of point position error $\Delta_p$ and normal error $\Delta_n$.

$$\Delta_p = (\Delta_1 + r_c\Delta_{1n}) + (\Delta_2 + r_c\Delta_{2n}) \qquad (4\text{-}7)$$

$$\Delta_n = \Delta_{1n} \times \Delta_{2n} \qquad (4\text{-}8)$$

From these analyses, the normal vector error in cylinder candidates is significantly larger than the normal vector errors in plane candidates. The similarity could be found in cone surface generation.

In Figure 4.5a, the cylinder (height, 800 mm; radius, 100 mm) is supported by 800 points; distances of these points to the cylinder are zero. In Figure 4.5b, the plane (length, 300 mm; width, 630 mm) is generated by 800 points; distances between the points and plane are zero. The density of the two sets of points is the same. With $0.05^o$ deflection on the axis of the cylinder and normal of the plane, there are 59.53% of points of cylindrical point clouds that have the distances between the deflected cylinder lower than 0.05 mm. In terms of the plane, 37.5% points have distances lower than 0.05 mm. Therefore, in the same condition of normal errors, there are higher chances to generate the incorrect cylinder/cone surfaces. It could be concluded that, in the RANSAC-based surface fitting method, the normal direction obtained from the plane surface has much higher precision than the axis direction calculated from cylinder/cone surface fitting.



a          b
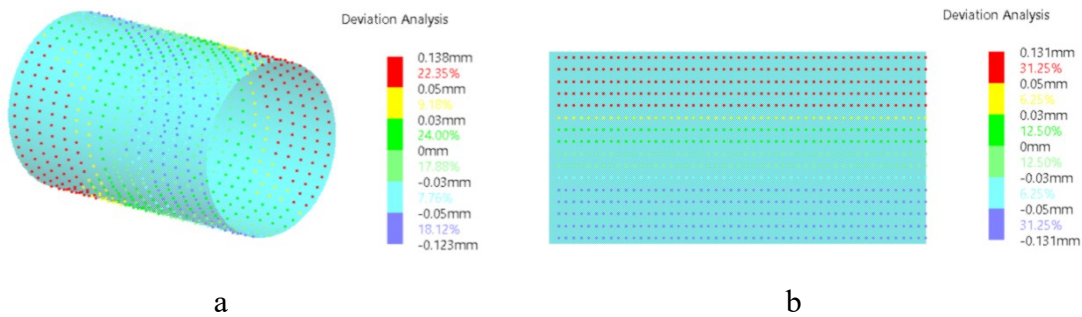
Figure 4.5: Deviation analysis under $0.05^o$ deflection for (a) cylinder and (b) plane.

### 4.2.2.3 Main Direction Estimation

A mechanical part has a common property of having limited primitives or regular shapes, and the axes of these primitives are either parallel or orthogonal. The axes of the primitives reside can be merged as main directions of the mechanical model. In the RANSAC-based method, it is significantly important to consider the global relations of each primitive to increase the precision of surface fitting [31,72]. Therefore, the main direction estimation

is helpful to provide a global view for leading a robust primitive surface fitting. Moreover, information of main directions can highly rise computation efficiency in cylinder/cone fitting because their degrees of freedom reduces if their axes are confirmed. As mentioned before, the normal estimation in plane fitting is much more reliable. Based on that conclusion, the main direction estimation method is developed from the normal of planes.

The process of the proposed method is represented in Figure 4.6. The original RANSAC method is adopted to calculate normal axes of planes from point clouds, $\boldsymbol{n}_i \in \mathbb{R}^3, i = 1,\ldots, \mathrm{m}$. These normal axes are classified based on the angles $\theta_{ij} = cos(|\boldsymbol{n}_i \cdot \boldsymbol{n}_j|)$. If $\theta_{ij} \leq \pi/4$, then normal $\boldsymbol{n}_i$ and $\boldsymbol{n}_j$ are determined as a parallel relation and classified in a group $\boldsymbol{N}_1$; else, they have an orthogonal relation and classified in another group $\boldsymbol{N}_2$. In the proposed method, in order to simplify the problem, the number of main directions is restricted to three $\boldsymbol{MD}_1, \boldsymbol{MD}_2$ & $\boldsymbol{MD}_3$, so that there are three groups of normal sets $\boldsymbol{N}_1 = \{\boldsymbol{n}_{1,i} \in \mathbb{R}^3, i = 1,\ldots, m\}, \boldsymbol{N}_2 = \{\boldsymbol{n}_{2,i} \in \mathbb{R}^3, i = 1,\ldots, n\}$ & $\boldsymbol{N}_3 = \{\boldsymbol{n}_{3,i} \in \mathbb{R}^3, i = 1,\ldots, l\}$. It is trivial to expand the main direction numbers by the proposed method in future work. Then, the estimation of the main direction can be converted to an optimization problem shown as follows:

Objective function:

$$f = \sum_{k}^{3} \boldsymbol{MD}_k \cdot \boldsymbol{N}_k \tag{4-9}$$

Subject to:

$$\boldsymbol{MD}_1 \cdot \boldsymbol{MD}_2 = 0$$

$$\boldsymbol{MD}_1 \cdot \boldsymbol{MD}_3 = 0 \tag{4-10}$$

$$\boldsymbol{MD}_2 \cdot \boldsymbol{MD}_3 = 0$$

The linear objection function with quadratic conditions can be solved in the Lagrange method.
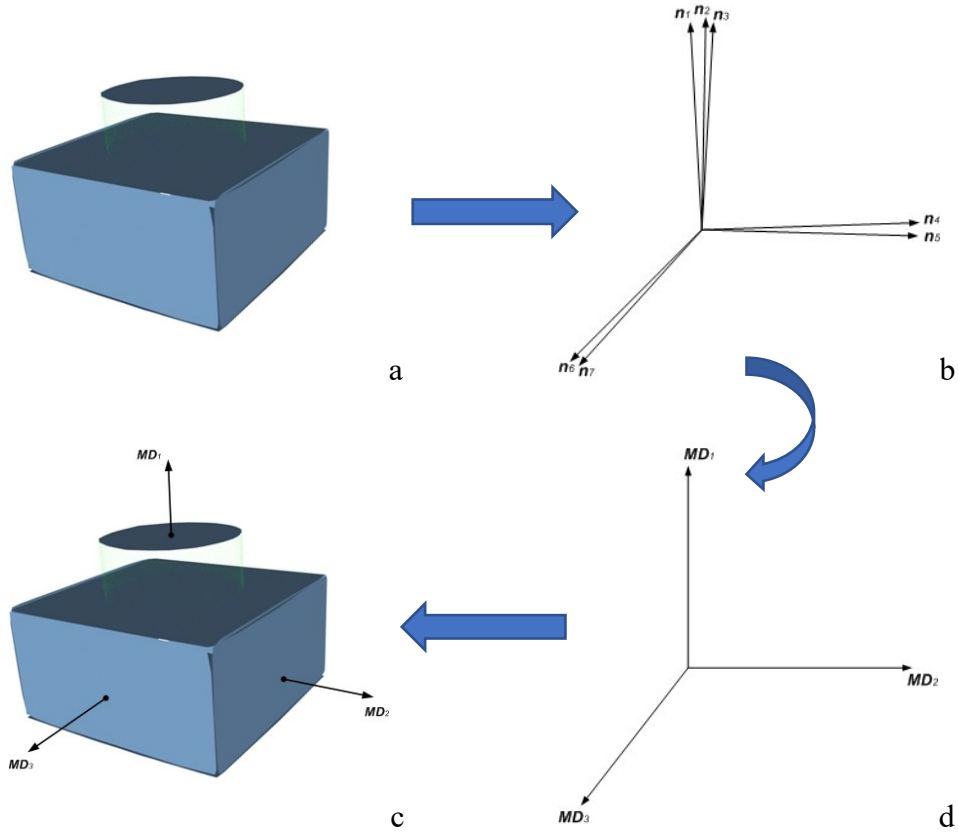


Figure 4.6: The process of main direction determination in the proposed method: (a) plane detection by basic RANSAC; (b) normal extraction from detected planes; (c) main direction optimization; (d) main direction interpolation in the model.

**4.2.2.4 Cylinder and Cone Surface Fitting**

The optimized main directions are used for guiding the following cylinder/cone fitting.

For cylinder fitting, the algorithms of the fitting process are shown as follows:

Table 4.1: the algorithm for cylinder fitting.

| | |
|---|---|
| a | Randomly select three points $\boldsymbol{p}_1, \boldsymbol{p}_2, \boldsymbol{p}_3$ from point clouds $\boldsymbol{P} = \{\boldsymbol{p}_i \in \mathbb{R}^3, i = 1, \ldots, m\}$ with corresponding normals are $\boldsymbol{n}_1, \boldsymbol{n}_2, \boldsymbol{n}_3$; |

| b | Determine the axis from main directions $MD_1, MD_2$ & $MD_3$ by calculating the dot product between point normals and three main directions separately, $cyla_i = n_1 \cdot MD_i + n_2 \cdot MD_i + n_3 \cdot MD_i$. The main direction $MD_i$ which has lowest $cyla_i$ value is determined as the axis for cylinder; |
|---|---|
| c | Project $p_1, p_2, p_3$ on the plane which is orthogonal to $MD_i$ and use these projected points to generate a circle. The center of the circle is the point on the axis of the cylinder and the radius of the circle is the radius of the cylinder. Now, candidate cylinder is constructed; |
| d | Calculate the algebraic distance of each point from point cloud to the candidate cylinder and record the number of valid points which is defined as the point that has distance less than the threshold to the candidate. Find the best candidate after serval iterations, which have the greatest number of valid points; |
| e | Use SDM refitting to optimize the cylinder parameters from segmented valid points. |

The processes of cone fitting are similar to cylinder fitting, which are presented as in Table 4.2.

Table 4.2: the algorithm for cone fitting.

| a | Randomly select three points $p_1, p_2, p_3$ from point clouds $P = \{p_i \in \mathbb{R}^3, i = 1, \dots, m\}$ with corresponding normals are $n_1, n_2, n_3$; |
|---|---|
| b | Determine the axis from main directions $MD_1, MD_2$ & $MD_3$ by calculating $cona_i = |n_1 \cdot MD_i - n_2 \cdot MD_i| + |n_1 \cdot MD_i - n_3 \cdot MD_i| + |n_2 \cdot MD_i - n_3 \cdot MD_i|$. The main direction $MD_i$ which has the lowest $cona_i$ value is determined as the axis for cone. The angle of the cone is $arccos(|n_1 \cdot MD_i|)$; |
| c | Set define planes $pl_1, pl_2, pl_3$ include a point respectively from $p_1, p_2, p_3$ and along its normals $n_1, n_2, n_3$. The apex of the cone is the intersection point of the planes. Now, the candidate cone is constructed; |
| d | Calculate the algebraic distance of each point from point cloud to the candidate cone and record the number of valid points, which is defined as the point has distance less than the threshold to the candidate. Find the best |

candidate after serval iterations, which have the greatest number of valid points;

e    Use SDM refitting to optimize the cone parameters from segmented valid points.

## 4.2.3 SDM Refitting for Quadratic Surface

The RANSAC-based method is barely able to meet the industrial tolerance requirement. In the proposed method, the SDM fitting approach is used for refitting after RANSAC detection. Outliers and noise are efficiently removed, which provide an appropriate condition for non-linear optimization surface fitting. The remaining valid points without outliers are input for the refitting process and the obtained parameters are utilized as the initial value for the iterative process.

The surface fitting problem is converted to an optimization problem as minimizing the objective function of a distance error between the point cloud and fitting shape. As mentioned before, SDM not only measures the distance between the fitting object and point clouds accurately but also leading a faster and more stable convergence in optimization. The objective function of SDM is initialized with the valid points $VP$ and the set parameters $v$ for the best shape $BS$ obtained from StepRANSAC as the initial value.

Then, we discuss the SDM process for each point from point clouds. For a given surface $\phi \subset \mathbb{R}^3$, $p_i$ is a point from a set of point clouds $P = \{p_i \in \mathbb{R}^3, i = 1, \ldots, m\}$. The squared distance $d^2$ is defined as the square of its distance $d$ from this point to its closest point $s$ on surface $\phi$. The surface fitting problem is considered as optimization by minimizing the sum of squared distances between the fitting shape and point clouds.

The Frenet frame of surface $\phi$ two vectors $n_1, n_2$ to determine the principal curvature directions and $n_3$ to determine the normal direction. The principal curvatures $k_j, j = 1,2$ are in the principal curvature direction $n_j$ and the corresponding curvature radii is $\rho_j$. For each point $p_i$, the second-order Taylor approximant $F$ of the squared distance $d^2$ is:

$$F_i = \frac{d_i}{d_i - \rho_{1i}} [\boldsymbol{n}_{1i} \cdot (\boldsymbol{p}_i - \boldsymbol{s}_i)]^2 + \frac{d_i}{d_i - \rho_{2i}} [\boldsymbol{n}_{2i} \cdot (\boldsymbol{p}_i - \boldsymbol{s}_i)]^2$$
$$+ \frac{d_i}{d_i - \rho_{3i}} [\boldsymbol{n}_{3i} \cdot (\boldsymbol{p}_i - \boldsymbol{s}_i)]^2 \tag{4-11}$$

By summation the squared distance of all points, the objective function $F$ is shown as following:

$$F = \sum_{i=1}^{m} \sum_{j=1}^{3} \alpha_{ji}{}^k \{\boldsymbol{n}_{ji}{}^k \cdot [\boldsymbol{p}_i - \boldsymbol{s}_i(\boldsymbol{pv}^{k+1}, \boldsymbol{sv}_i{}^k)]\}^2 \tag{4-12}$$

where $\alpha_{1i} = \frac{d_i}{d_i - \rho_{1i}}$, $\alpha_{2i} = \frac{d_i}{d_i - \rho_{2i}}$, $\alpha_{3i} = 1$.

In Equation (4-12) , $\boldsymbol{s}_i$ is the closest point on the fitting surface related to point $\boldsymbol{p}_i$ Here, $\boldsymbol{s}_i$ consists of parameter vector $\boldsymbol{pv}$ and state vector $\boldsymbol{sv}$. And $\boldsymbol{pv}$ indicates parameter vector of surface $\phi$, $\boldsymbol{pv} = \{pv_i \in \mathbb{R}, i = 1, \ldots, n\}$. For cylinder, $\boldsymbol{pv}_{\text{cyl}} = \{x_0, y_0, z_0, r\}$, where $(x_0, y_0, z_0)$ is a point of the axis of cylinder and r is the radius. For cone, $\boldsymbol{pv}_{\text{con}} = \{x_0, y_0, z_0, \vartheta\}$, where $(x_0, y_0, z_0)$ is apex cone and $\vartheta$ is the semi-opening angle of the cone surface. For sphere, $\boldsymbol{pv}_{\text{sph}} = \{x_0, y_0, z_0, r\}$, where $(x_0, y_0, z_0)$ is the center and $r$ is the radius of the sphere surface. $\boldsymbol{sv}_i$ is the state vector of the quadratic surface from parametric representation, and it determines the $i$-th point on the surface.

Setting the first-order derivative of $F$ to zero and solving the linear equation system is to obtain an updated quadratic surface, as:

$$DF = \left[ \frac{\partial F}{\partial pv_1}, \frac{\partial F}{\partial pv_2}, \ldots, \frac{\partial F}{\partial pv_n} \right] = \boldsymbol{0} \tag{4-13}$$

The parameters of fitting shape are updated by new parameters from solving the set of linear equations. When the surface $\phi$ is updated to a new parameter vector $\boldsymbol{pv}^{k+1}$, the squared distance error is computed again for all data points in Equation (4-12) as the next

iteration. By repeating the steps until a pre-defined incremental change is reached, the parameter vector of the final adapted quadratic surface is obtained. The proposed SDM refitting has strongly increased the fitting precision, and it is evaluated in case studies.

## 4.2.4 Modelling Operation

The void model is obtained after the surface fitting process. A model operation is required to convert the void model to a solid model. A solid model is composed of different solid features. In the conventional modelling method, CAD systems provide functions to create primitive solids such as block, cylinder, cone, sphere, torus and wedges. The parameters of surfaces obtained in the surface fitting process are used to generates their corresponding primitive solids. The solid model could be constructed by combining these primitive solids by basic Boolean operations.

## 4.2.5 Damaged Volume Localization for Remanufacturing/Repairing

The damaged volume can be localized by registering the reconstructed model and defective model (Figure 4.7). The defective volume could be extracted by a Boolean operation. CAD/CAM software can be used for the generation of tool paths for remanufacturing. By applying post-processing on tool paths, G-code can be produced to drive machines for an actual repair process which includes a sequence of machining and AM [18,90].
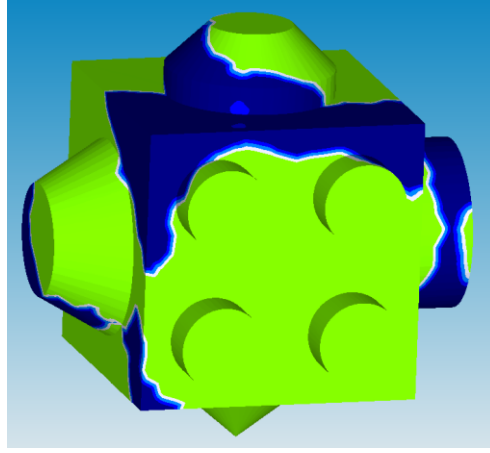
Figure 4.7: Identified damaged space (covered by blue) and intact space (covered by yellow).

## 4.3 Case Studies and Discussion

All algorithms described are implemented in C++. Four tests have been conducted for the validation of algorithms. For comparison purposes, a proven RANSAC-based method [71] is applied for surface fitting on the same data. For the surface fitting quality analysis in case study I, the average surface fitting error and maximum surface fitting are defined as presented in Equation (4-14) and (4-15), respectively. For the reconstruction quality analysis in case study II to IV, the error for each parameter of surface is comparing with the corresponding surface parameter in the nominal CAD model.

$$\text{Error}_{\text{ave}} = \sqrt{\frac{1}{m} \cdot \sum_{i=1}^{m} \|\boldsymbol{p}_i - \boldsymbol{s}_i\|^2} \qquad (4\text{-}14)$$

$$\text{Error}_{\text{max}} = \max\left(\sqrt{\|\boldsymbol{p}_i - \boldsymbol{s}_i\|^2}\right) \qquad (4\text{-}15)$$

### 4.3.1 Case Study I

The first experiment was conducted to test the performance of the basic RANSAC surface fitting and proposed method in the cylinder, cone, and sphere separately. For fitting quality

analysis, the fitting error is defined as the average of distances of each point to the target shape as shown in Equation (4-14). The proposed method and basic RANSAC were evaluated on the cylinder, cone, sphere fitting from 0% noisy point clouds and 10% noisy point cloud.

Table 4.3 gives the comparison results of cylinder fitting from the proposed method and RANSAC. The relative improvement of the proposed method over the RANSAC is averagely less 82% error for 0% noisy point cloud and less 68% for 10% noisy point clouds. Figure 4.8 presents the fitting results of the cylinder in the proposed method.

In terms of cone surface fitting, from Table 4.4, a similar conclusion can be drawn the proposed method shows higher precision than the RANSAC method because the fitting error of the proposed method is 96% less in 0% noisy point clouds and 70% less in 10% noisy point clouds. Figure 4.9 and Figure 4.8 shows the fitting results of the cone in the proposed method.

Table 4.5 shows the fitting results of the sphere fitting in the proposed method and RANSAC. It is important to mention that, because the sphere has no axis parameter, the StepRANSAC cannot provide the accurate axis for sphere fitting. However, the proposed method consistently has better performance than basic RANSAC, where shows 92% less error and 79% less error in 0% and 10% noisy point cloud, respectively. From these results, it can be concluded that the SDM refitting process in the proposed method has a great contribution to improving the precision of surface fitting.

Table 4.3: Performance comparisons of the proposed method and RANSAC in cylinder surface fitting

| Data | 0% noisy point clouds | | 10% noisy point clouds | |
|---|---|---|---|---|
| Fitting method | Proposed method | RANSAC | Proposed method | RANSAC |
| Point on axis | (3.0082, 5.0145,0) | (2.3892, 5.2327,0) | (2.9801, 5.0241,0) | (3.1232, 4.9717,0) |

| | | | | |
|---|---|---|---|---|
| Axis orientation | (0,0,1) | (0.0608, 0.0118, 0.9981) | (0,0,1) | (0.0106, 0.0275, 0.9996) |
| Radius | 8.1323 | 7.8701 | 8.1178 | 7.8701 |
| Ave. fitting error (mm) | 0.0461 | 0.2686 | 0.0851 | 0.2660 |
| Max. fitting error (mm) | 0.2201 | 1.209 | 0.5372 | 1.5581 |
| Ave. improvement | 82% | | 68% | |
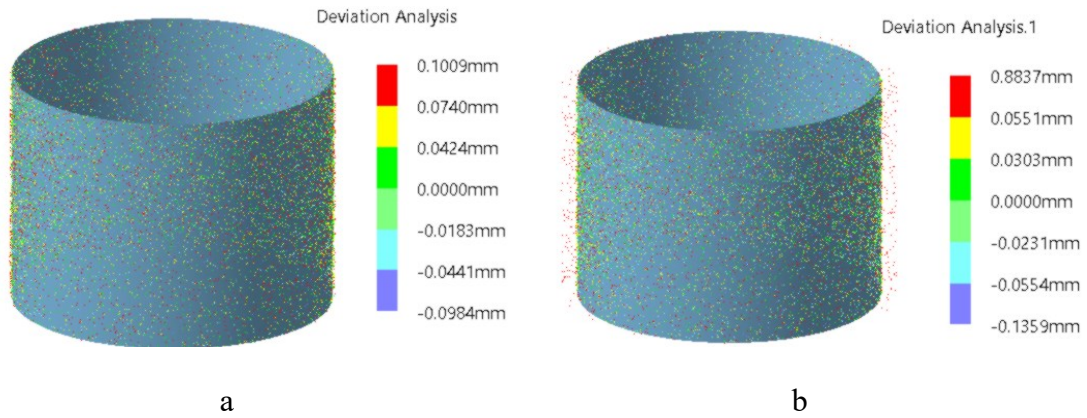


Figure 4.8: cylinder fitting results by the proposed method from (a) 0% noisy point clouds; (b) 10% noisy point clouds.

Table 4.4 Performance comparisons of the proposed method and RANSAC in cone surface fitting.

| Data | 0% noisy point clouds | | 10% noisy point clouds | |
|---|---|---|---|---|
| Fitting method | Proposed method | RANSAC | Proposed method | RANSAC |

| | | | | |
|---|---|---|---|---|
| Apex | (2.9106, 5.0301, 7.0013) | (2.3892, 5.2327, 7.1321) | (2.9983, 4.9997, 7.0347) | (3.4513, 5.7896, 7.5347) |
| Axis orientation | (0,0,1) | (0.0092, 0.0021, 0.8532) | (0,0,1) | (0.1118, 0.0197, 0.9935) |
| Angle | 30.0108 | 32.1251 | 30.1042 | 29.1523 |
| Ave. fitting error (mm) | 0.0101 | 0.2871 | 0.0450 | 0.1514 |
| Max. fitting error (mm) | 0.3607 | 2.129 | 0.4532 | 1.9101 |
| Ave. improvement | 96% | | 70% | |



a                                                    b
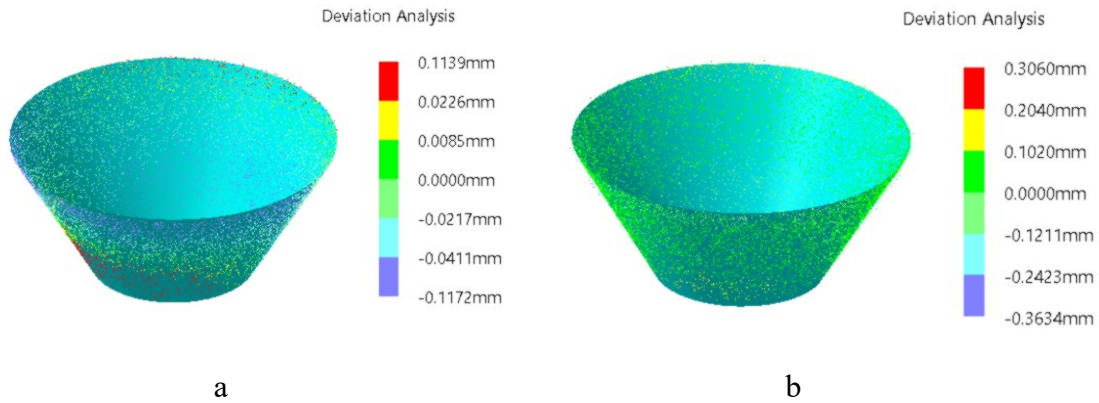
Figure 4.9: Cone fitting results by the proposed method from (a) 0% noisy point clouds; (b) 10% noisy point clouds.

Table 4.5: Performance comparisons of the proposed method and RANSAC in sphere surface fitting.

| Data | 0% noisy point clouds | | 10% noisy point clouds | |
|---|---|---|---|---|
| Fitting method | Proposed method | RANSAC | Proposed method | RANSAC |

| | | | | |
|---|---|---|---|---|
| Central point | (2.9956, 4.9876, 7.0018) | (2.7292, 5.1327, 7.1321) | (2.9946, 4.9802, 7.0756) | (2.8102, 5.6128, 6.9321) |
| Radius | 6.0436 | 5.946 | 6.0742 | 6.1051 |
| Ave. fitting error (mm) | 0.0170 | 0.2021 | 0.0502 | 0.2376 |
| Max. fitting error (mm) | 0.1415 | 1.7818 | 0.2175 | 1.3299 |
| Ave. improvement | 92% | | 79% | |
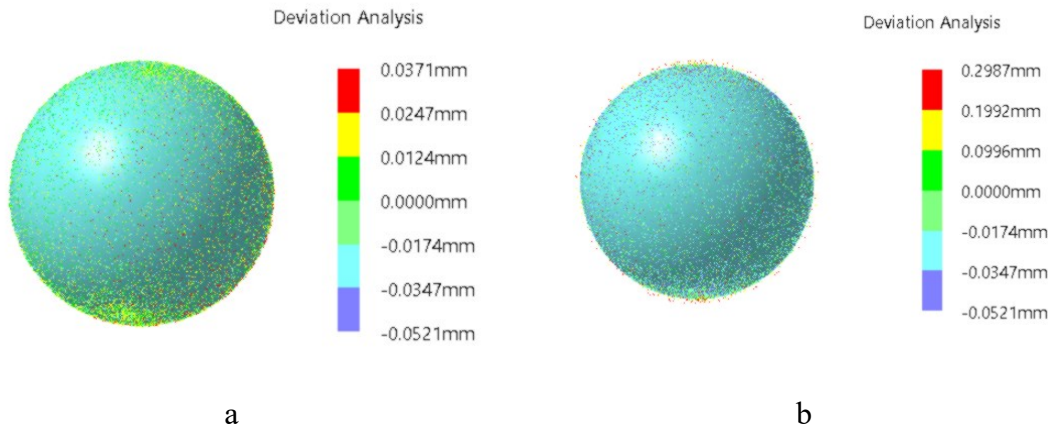


Figure 4.10: Sphere fitting results by our method from (a) 0% noisy point clouds; (b) 10% noisy point clouds.

## 4.3.2 Case Study II

In the second experiment, the proposed method is validated through a synthetic model (Figure 4.11a) which is composed of planes, cylinders and cones. A damaged structure is constructed from this model (Figure 4.11b). In order to simulate the data acquisition process, the defective model was scanned to point clouds in a scanning simulation software (Blensor) (Figure 4.11c). The uniform scanning data is integrated with Gaussian noise ($\sigma$ =0.4). The surface fitting results of the traditional RANSAC method and the proposed

method are shown in Figure 4.12 and Figure 4.13 respectively. In these figures, grey is for plane, green is for cylinder, and purple is for cone. From Figure 4.12, the surface fitting deviation with the traditional RANSAC-based method can be observed in the naked eye.

Table 4.6 gives the comparison results of the error in the proposed method and the RANSAC method. By comparing two methods, one can observe that the relative improvement of the proposed method over the basic RANSAC method is averagely less 81%, 91%, 90.6% for the plane, cylinder, cone fitting respectively. It can strongly prove that the proposed method is accurate. The reconstructed CAD model is shown in Figure 4.13c.



| a | b | c |
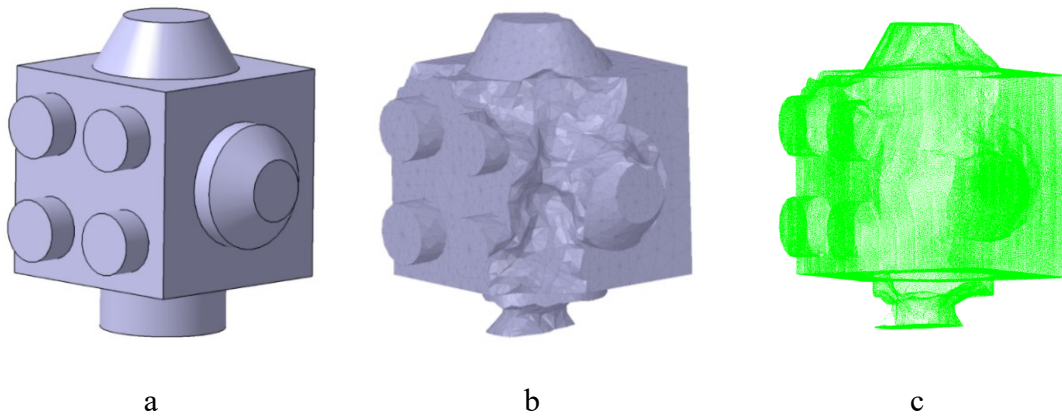
Figure 4.11: (a) Original model, (b) defective model, (c) point clouds from defective model.



| a | b |
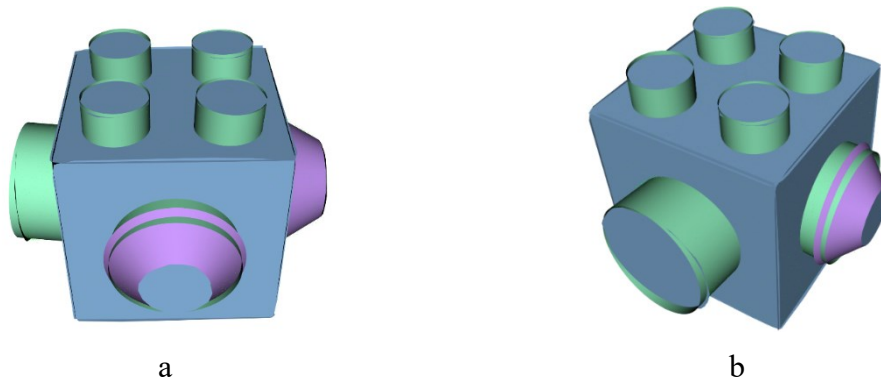
Figure 4.12:Traditional RANSAC surface fitting result: (a) view 1; (b) view 2.
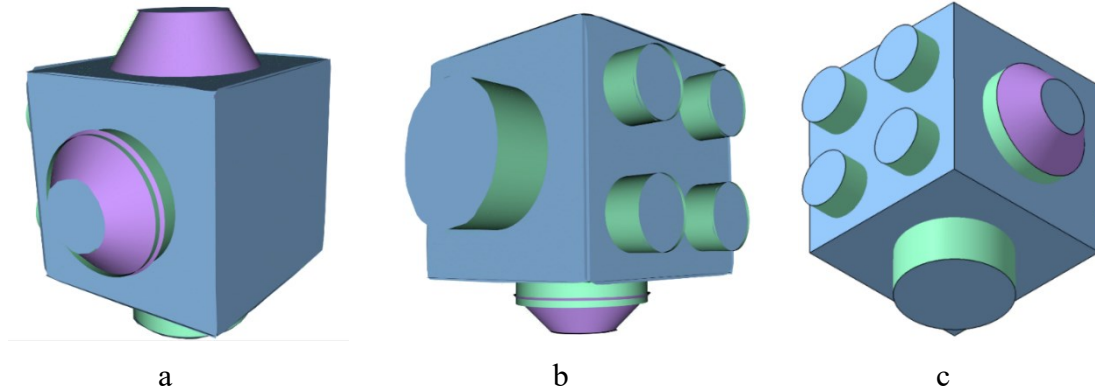
Figure 4.13: Our method surface fitting result: (a);view 1; (b) view 2; (c) The reconstructed CAD model.

Table 4.6: Error analysis of the proposed method and RANSAC method synthetic model fitting results.

| Plane fitting | #planes | Normal error | Distance error | Ave. improv. | |
|---|---|---|---|---|---|
| Proposed method | 13 | 0.0156 | 0.1232 | 82% | |
| RANSAC | 13 | 0.0526 | 2.2861 | | |
| Cylinder fitting | #cylinder | Axis error | Central point error | Radius error | Ave. improv. |
| Proposed method | 6 | 0.1451 | 0.1007 | 0.0212 | 91% |
| RANSAC | 6 | 1.4459 | 1.2107 | 0.3105 | |
| Cone fitting | #cone | Axis error | Apex error | Angle error | Ave. improv. |
| Proposed method | 3 | 0.0208 | 0.1121 | 0.0286 | 90.6% |
| RANSAC | 3 | 0.3208 | 0.8021 | 0.4270 | |

## 4.3.3 Case Study III

In the third experiment, a virtual damaged bracket (Figure 4.14a) is tested. The defective model was scanned to point clouds with Gaussian noise ($\sigma$ =0.4) in a scanning simulation software (Blensor) (Figure 4.14b). From Table 4.7, the relative improvement of the proposed method over the basic RANSAC method is averagely less 62%, 80.6% for the

plane, cylinder fitting respectively, providing strong evidence that the proposed method is promising in the primitive surface fitting. The reconstructed bracket model is presented in Figure 4.16b.



a                                    b
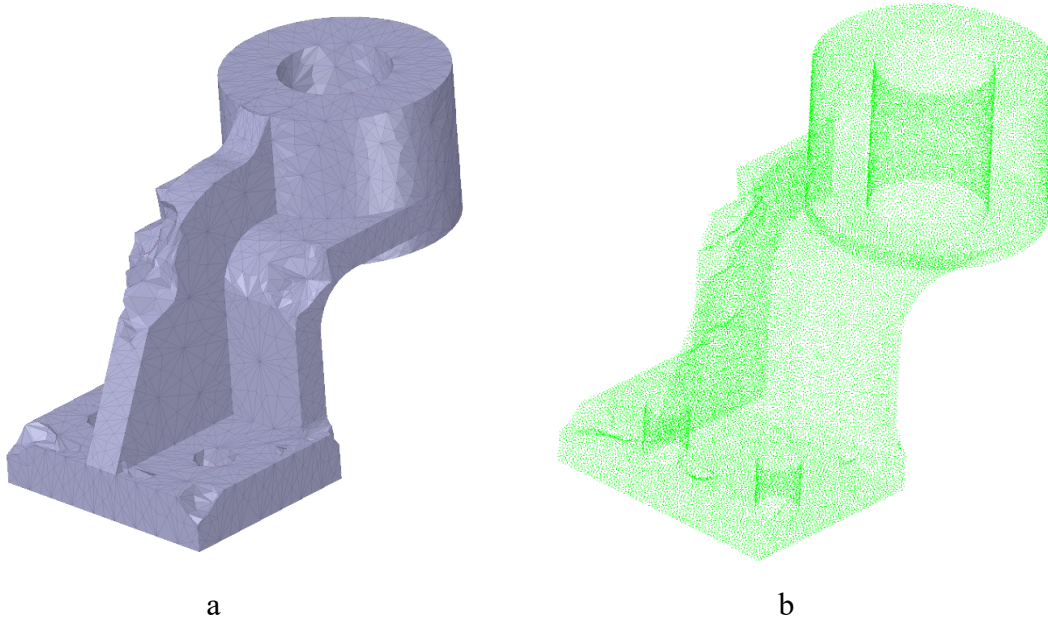
Figure 4.14: Bracket models: (a) defective model; (b) point clouds from the defective model.
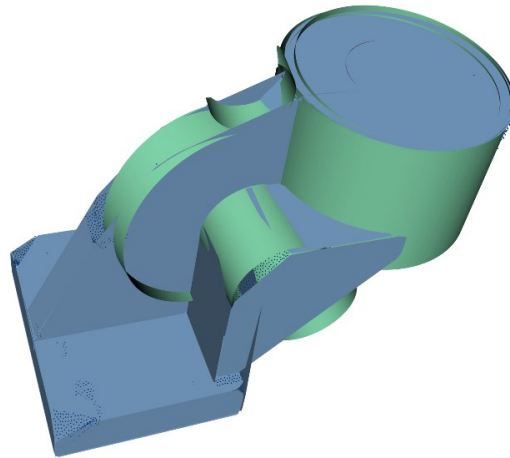


Figure 4.15: Traditional RANSAC surface fitting result for the bracket.

a                                          b
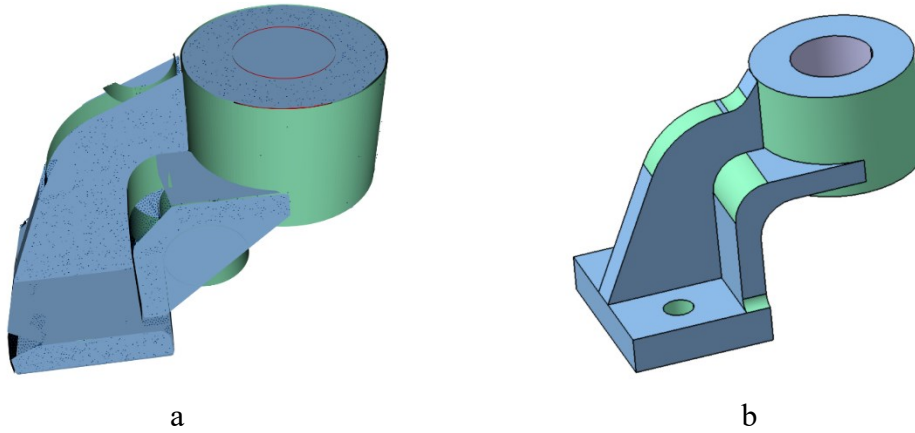
Figure 4.16: (a) The proposed surface fitting result for the bracket ; (b) reconstructed CAD model.

Table 4.7: Error analysis of the proposed method and RANSAC method bracket model fitting results.

| Plane fitting | #planes | Normal error | Distance error | Ave. improv. | |
|---|---|---|---|---|---|
| Proposed method | 17 | 0.0626 | 0.0816 | 62% | |
| RANSAC | 17 | 0.0912 | 1.2089 | | |
| Cylinder fitting | #cylinder | Axis error | Central point error | Radius error | Ave. improv. |
| Proposed method | 9 | 0.0751 | 0.0907 | 0.1205 | 80.6% |
| RANSAC | 9 | 1.2195 | 0.9333 | 0.3001 | |

## 4.3.4 Case Study IV

In the fourth case study, a damaged bracket (see Figure 4.17) was used in the evaluation of the proposed method. An OKIO-E non-contact 3D scanner was employed in this study to acquire the point clouds of the surface of the object (as shown in Figure 4.18). The parameters of the scanner are found in Table 4.8.

Before scanning, one crucial step was to spray an imaging agent on the object since its surface is very reflective. To determine the position of each scan, 34 monochrome paper

mark points were attached to the object randomly. Then, the position and distance of the scanner from the object were adjusted to make the object to be located in the center of the view. For each scan to be valid, a minimum of four mark points needs to be in the scanning view. To minimize the effect of uncertainty of point clouds, the number of measurements for the object had been determined to 3 after a series of experiments. The scanned point clouds of the object were 2,760,000. These scanned points were imported into Geomagic Wrap to be processed. After a set of processing steps, the point clouds of the object can be exported.



     a             b         c         d
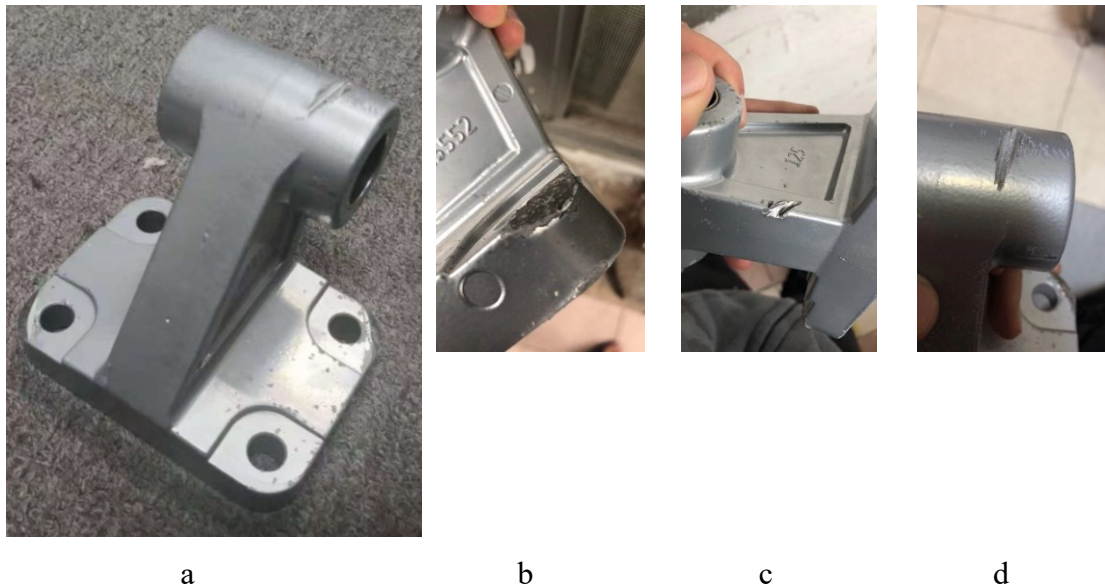
Figure 4.17: A damaged bracket, (a) overall view; (b) damage in bottom; (c) damage in rib; (d) damage in cylinder holder.
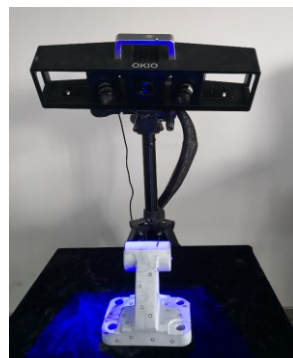


Figure 4.18: The digitalization process of the bracket by the 3D scanner.

Table 4.8: Parameters of the 3D scanner

| | |
|---|---|
| Measurement Range | $400*300mm^2$—$100*75mm^2$ |
| Measurement Resolution | 0.035mm—0.015mm |
| Average Distance of Samples | 0.31mm—0.07mm |
| Pixels | 1.3 Mega |
| Scanning Time | ≤5s |
| Scanning Mode | Non-contact，Camera-based |
| Splice Mode | Automatic splicing based on mark points |
| Output Format | ASC, STL, etc. |

After obtaining the digital model of the damaged bracket, the proposed algorithms are applied in the model. Figure 4.19a and Figure 4.19b represent the surface fitting results of the RANSAC method and the proposed method, respectively. For fitting quality analysis, the fitting error is defined as the average of distances of each point to the target shape. From Table 4.9, the relative improvements of the proposed method over the basic RANSAC method are on average 79% and 80% for the plane and cylinder fitting respectively. It proves that the proposed method is also robust and precise in the real case study.



a                                                      b
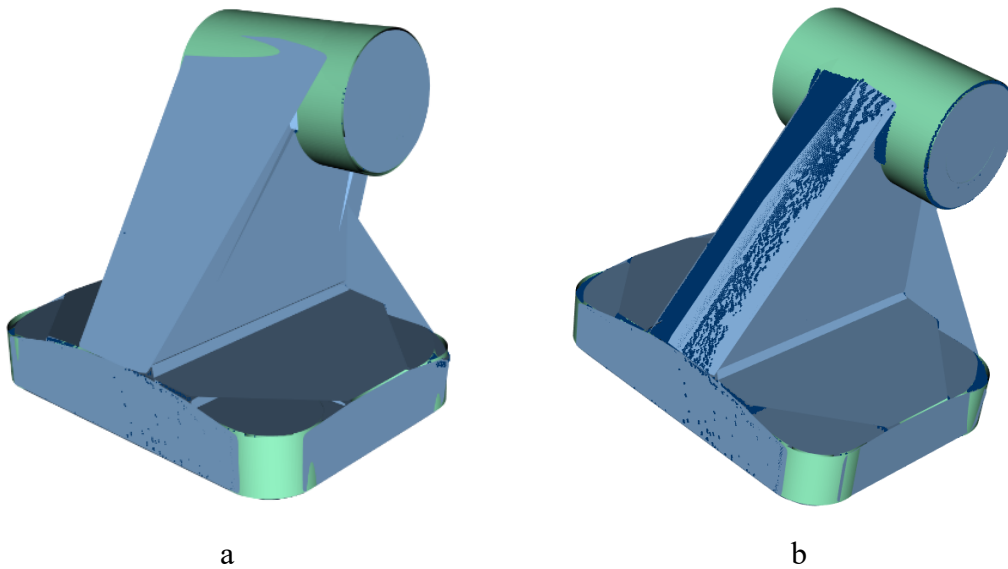
Figure 4.19: (a) The proposed surface fitting result for the bracket ; (b) reconstructed CAD model.

Table 4.9: Error analysis of the proposed method and RANSAC method damage bracket model fitting results.

| Plane fitting | #planes | Normal error | Distance error | Ave. improv. | |
|---|---|---|---|---|---|
| Proposed method | 63 | 0.0931 | 0.1216 | 79% | |
| RANSAC | 63 | 0.3012 | 1.3019 | | |

| Cylinder fitting | #cylinder | Axis error | Central point error | Radius error | Ave. improv. |
|---|---|---|---|---|---|
| Proposed method | 12 | 0.1223 | 0.2007 | 0.2015 | 80% |
| RANSAC | 12 | 1.0213 | 1.2032 | 0.7021 | |

## 4.4 Conclusion and Perspectives

Reconstruction of the nominal CAD model of a damaged part from the incomplete scanning data is a critical technique for the repairing process. So far, most of the related publications have been focusing on applications of turbine blades with prior information such as it is a continuous and closed freeform surface, while the reconstruction of general mechanical components which consists of varies types surfaces is much less concentrated. Therefore, to fill this gap, this chapter demonstrates a successful reconstruction method which includes processes of 3D scanning, damage surface identification, StepRANSAC surface fitting, SDM refitting, modelling, damage volume localization, and extraction. As for the main contribution, the remanufacturing does not require a priori information of the nominal CAD model. Additionally, the combination of StepRANSAC and SDM has proven a 60–90% improvement in precision compared with the traditional RANSAC method.

On the other hand, this work is still incomplete since free-form surface reconstruction is not involved. Given the fact that free-form surfaces are playing an increasingly more important role in mechanical design, this aspect will be highly focused in the future.

# Chapter 5: A Cost-driven Process Planning Method for Hybrid CNC-PBF Remanufacturing

## 5.1 Overview

From the literature review in Section 2.3, an increasing level of interest in research on HM-based remanufacturing has been witnessed over recent years. By summarizing these research results, it can be identified that a few challenging problems that have rarely been addressed. For example, AM and SM feature extraction relies heavily on manual operations that lack algorithm support; the process planning result is non-unique, and a quantitative evaluation mechanism is missing to support decision-making (e.g., cost-driven decision-making). Therefore, addressing these two challenging issues is the primary motivation of this chapter. Specifically, the study in this chapter is focusing on the hybrid technologies of using CNC and PBF in sperate machines. Under this environment, a cost-driven process planning method for HM is proposed. It features automated AM–SM feature extraction. A precedence-directed graph is used to represent the process sequences and an integer programming model is formulated to derive the optimal process plan that minimizes the overall remanufacturing cost.

## 5.2 Methodology

In this study, an "end-of-life" part (or an existing part) is used as the raw workpiece for fabricating the new part with HM technology. With AM, metal materials are deposited on the workpiece to create new features; with SM, redundant features of the existing part are removed through the subtractive process. Because of the flexibility of combining processes, HM-based remanufacturing can be performed with different process plans to achieve an identical effect; therefore, optimizing the process plans on the basis of global objectives (such as cost or environmental impact) to find the optimal solution would be necessary, which is also a challenging task. Therefore, a significant innovation of this

study is to develop a cost-based optimization algorithm to find the most economical HM process plan.
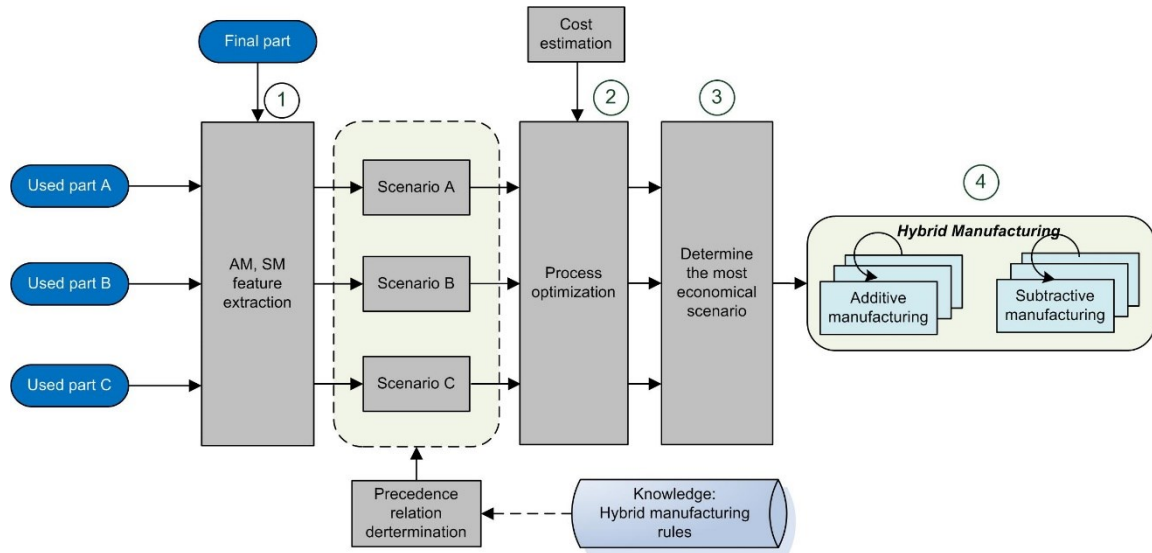


Figure 5.1: A framework of the proposed cost-driven decision system for hybrid remanufacturing process planning.

This study focuses on the PBF process for AM and three-axis CNC machining for SM, and 2.5D features are investigated. A framework of the proposed method is presented in Figure 5.1. It can be assumed that several used parts can potentially be used for remanufacturing. (1) Based on the geometric information of the new part, a feature extraction algorithm is implemented to recognize the AM and SM features. Here, one point to mention is that an automated feature extraction algorithm has been developed in this work based on the level-set method. (2) With the manufacturing feature information and HM process planning rules, a partially determined process plan is determined for each used part. The undetermined sequences can be decided through a solution calculated by an integer programming model. The process plan for each scenario is then optimized locally. (3) The most economical scenario can easily be selected by comparing the manufacturing costs among each optimized scenario. (4) Finally, the HM process follows the most cost-effective process plan.

## 5.2.1 Additive and Subtractive Feature Extraction

Feature recognition and extraction for machining processes have been extensively studied. In machining, automatic feature recognition and extraction of a 3D part is an essential step of process planning. However, these algorithms cannot be directly applied in remanufacturing or HM processes because the B-rep format model is dominant for the machining feature recognition [136]. Nevertheless, B-rep has difficulty dealing with numerical calculations involving two solid parts. Moreover, based on our extensive review, the existing feature extraction methods for HM rely heavily on manual operations that lack algorithm support. Therefore, in this research, an implicit level-set function-based method is developed to represent the 3D parts, which automated feature extraction for remanufacturing and fully addressed the manufacturing constraints of PBF technology.

The idea of the additive feature (AF) and subtractive feature (SF) extraction method is inspired by [137,138], which is illustrated in Figure 5.2. There are three main steps of this process: (1) intersection part extraction, (2) intersection part modification, and (3) feature extraction. In this study, a systematic flowchart of the proposed level-set function-based method is given in Figure 5.3, wherein the steps with referencing equations are demonstrated in detail. Firstly, the modeling history is extracted from the CAD models and Constructive Solid Geometry (CSG) of the used part and the final part are modeled via the level-set function-based method. The intersection volume is then obtained by optimally overlapping the used part and the final part. The intersection part is then modified on the basis of the AM constraints. Finally, the subtractive feature group (SFG) can be extracted through subtraction of the modified intersection part from the used part. Similarly, the additive feature group (AFG) is obtained by subtracting the modified intersection part from the final part. Individual SF and AF are then identified from their corresponding feature group by feature recognition algorithms.
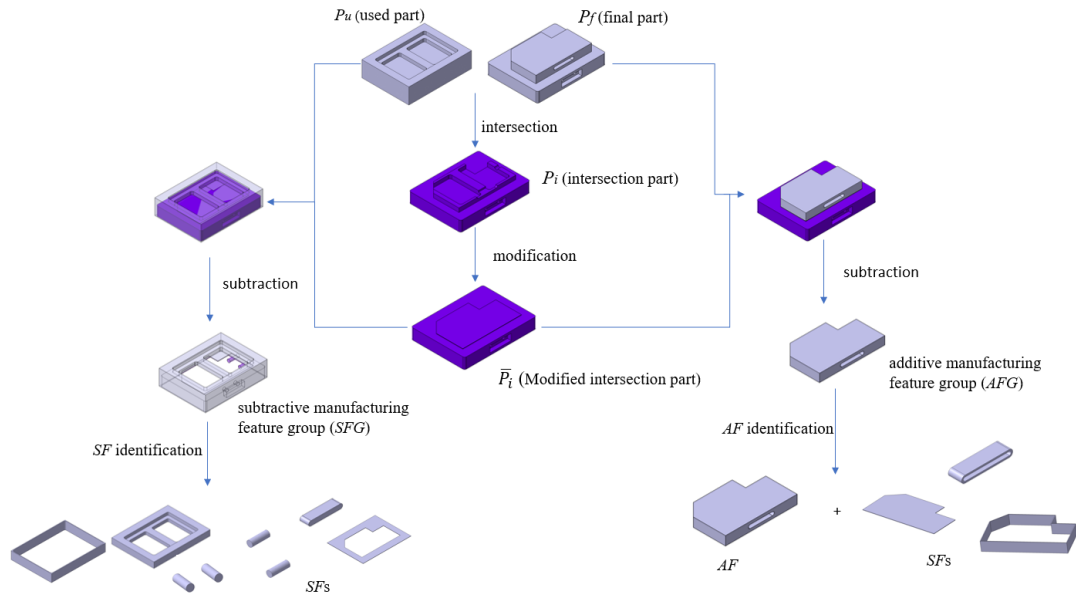
Figure 5.2: An illustration of the feature extraction process.
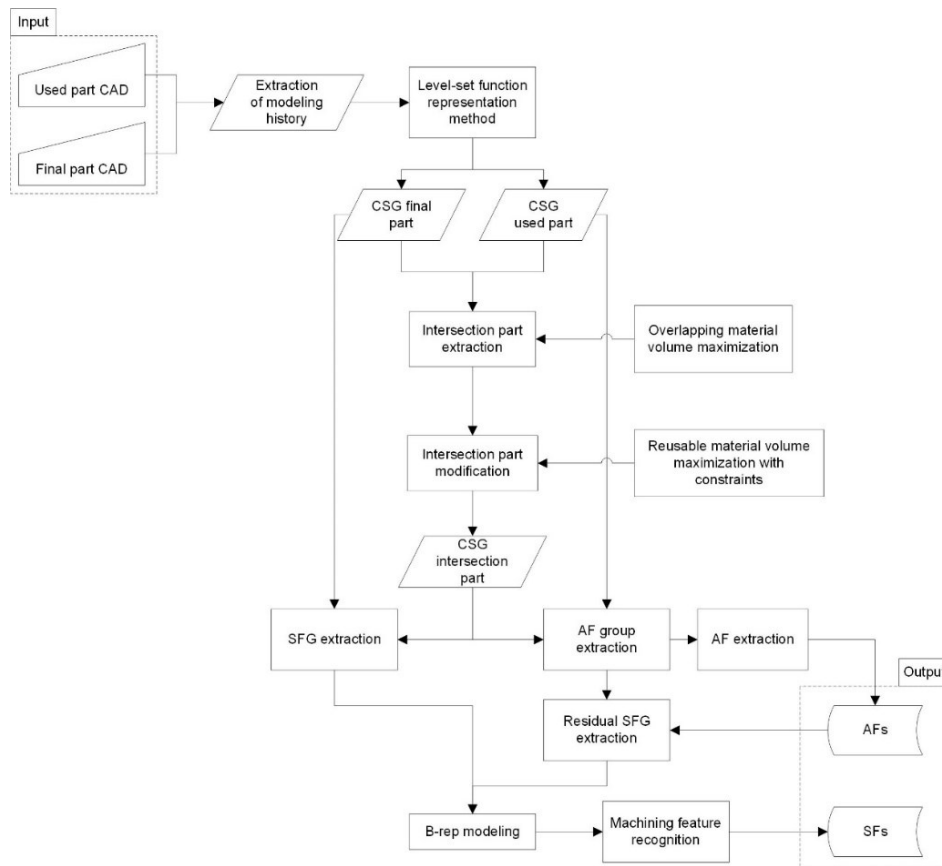


Figure 5.3: A systematic flowchart of the proposed feature extraction method.

69

**5.2.1.1 Feature Modeling**

Before implementing feature extraction, the specific feature modeling approach needs to be determined. CSG and B-rep are the two most commonly used solid modeling approaches. With CSG modeling, a physical object can be decomposed into multiple primitives and a sequence of Boolean operations. With the B-rep method, the solid is bounded by a set of closed and directional faces, which are bounded by edges and vertices. CSG modeling has the merits of supporting efficient Boolean operations and topology optimization. B-rep is dominant in feature recognition areas because it uniquely defines the faces and their topological patterns [136]. Currently, many commercial CAD modelers have a hybrid data structure, using both CSG and B-rep at the same time to facilitate CAD and CAM integration [149]. In this work, both CSG and B-rep are adopted to represent features, leveraging both methods' strengths. The specifications of the two methods are presented in the following sections.

*CSG modeling*

In this work, CSG models are built with level-set functions to represent the features in an implicit form (i.e., the part is implicitly represented by the level set function Φ). For the readers' convenience, the level-set function for implicit geometric modeling is shown in Equation (5-1) :

$$\begin{cases} \Phi(\mathbf{X}) > 0, \ \mathbf{X} \in \Omega/\partial\Omega \\ \Phi(\mathbf{X}) = 0, \ \mathbf{X} \in \partial\Omega \\ \Phi(\mathbf{X}) < 0, \ \mathbf{X} \in D/\Omega \end{cases} \qquad (5\text{-}1)$$

The areas with a positive sign represent the material domain $\Omega/\partial\Omega$, the areas with a negative sign represent the void $D/\Omega$, and the zero-contour represents the structural boundary $\partial\Omega$. For example, the level-set functions for a cube and sphere in $\mathbb{R}^3$ can be represented by Equation (5-2) and Equation (5-3) respectively.

$$\Phi_{\text{cube}}(\mathbf{X}) = \min\left\{\frac{Hx}{2} - (x - x_0), \frac{Hx}{2} + (x - x_0), \frac{Hy}{2} - (y - y_0), \frac{Hy}{2}\right.$$
$$\left. + (y - y_0), \frac{Hz}{2} - (z - z_0), \frac{Hz}{2} + (z - z_0)\right\} \tag{5-2}$$

$$\Phi_{\text{sphere}}(\mathbf{X}) = R^2 - [(x - x_0)^2 + (y - y_0)^2 + (z - z_0)^2] \tag{5-3}$$

in which $(x_0, y_0, z_0)$ are the center coordinates of the cube, $(Hx, Hy, Hz)$ is the length on the $x,y,z$ axis; $(x_0, y_0, z_0)$ are the center coordinates of the sphere, and $R$ is the radius.

The overall geometry can be constructed through Boolean operations on the individual level-set functions [135], as follows:

$$\text{Unite: } \Phi_1 \cup \Phi_2 = \max(\Phi_1, \Phi_2)$$
$$\text{Intersect: } \Phi_1 \cap \Phi_2 = \min(\Phi_1, \Phi_2) \tag{5-4}$$
$$\text{Subtract: } \Phi_1 \setminus \Phi_2 = \min(\Phi_1, -\Phi_2)$$

The parametric level-set presentation can be numerically discretized onto a fixed Cartesian mesh. The model can be visualized by distinguishing the solid and void areas. An example of CSG modeling is shown below. The CAD model is composed of four primary solids (spheres, cones, cylinders, and cubes) combined by a union operation. The example of implicit level-set function representation is given in Figure 5.4 and Table 5.1.
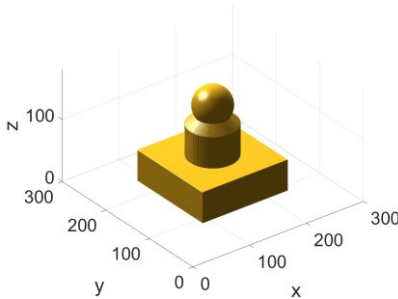


Figure 5.4: An example of a discrete level-set representation.

Table 5.1: The discrete level-set functions.

$$\Phi = \Phi_{\text{sphere}} \cup \Phi_{\text{cone}} \cup \Phi_{\text{cylinder}} \cup \Phi_{\text{cube}}$$

$$\Phi_{\text{cube}} = \min\{75 - x, x - 75, 75 - y, y - 75, 60 - z, z - 10\};$$

$$\Phi_{\text{sphere}} = 30^2 - (x - 150)^2 - (y - 150)^2 - (z - 150)^2;$$

$$\Phi_{\text{cone}} = \min\{(z - 150)^2 - (x - 150)^2 - (y - 150)^2, 130 - z, z - 110\};$$

$$\Phi_{\text{cylinder}} = \min\{37^2 - (x - 150)^2 - (y - 150)^2, 110 - z, z - 60\}.$$

### B-rep modeling

B-rep data records both the surface geometry and the topological relationships among these surfaces. The B-rep information can be directly read from the CAD model or reconstructed from the 3D point cloud. The former is trivial but the latter method includes the steps of (1) primitive surface extraction [150]; (2) determination of the relationships among all the extracted geometric primitives [151]; (3) B-rep construction by combining information from the two previous steps. The process is illustrated in Figure 5.5.
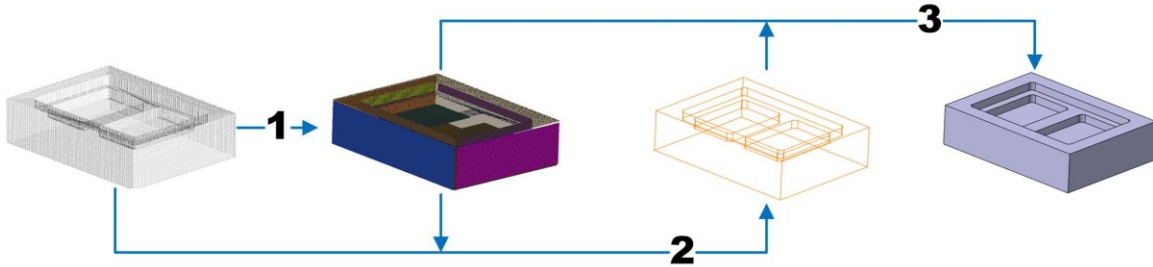


Figure 5.5: Illustration of the B-rep reconstruction method: Step 1: primitive extraction; Step 2: wire construction; Step 3: B-rep construction.

### 5.2.1.2 Intersection Part Extraction

For a given pair $(P_u, P_f)$ where $P_u$ represents the used part and $P_f$ represents the final part to manufacture, the first step is to identify the relative position between $P_u$ and $P_f$ to prepare for feature extraction. The principle is to maximize the overlapping material

volume; the cost of AM is severely affected by the volume of the new material to deposit; see Equation (5-5):

$$\max. \quad V(P_i = P_u \cap P_f) \tag{5-5}$$

In Equation (5-5), $P_i$ represents the intersection part and $V$ is the material's volume. A geometric optimization problem is formulated, where the orientation and spatial positions of $P_u$ and $P_f$ will be optimized.

It can be assumed that $\Phi_u$ and $\Phi_f$ are the implicit representations of the used part and the final part, respectively, within the global coordinate system $\mathbf{X} = (x, y, z)$. $\widetilde{\mathbf{X}}$ is the local coordinate system attached to the used part. Through Equation (5-6), an optimization problem can be formulated to find out the translation ($\mathbf{T}$) and rotation ($\boldsymbol{\theta}$) of the local coordinate system ($\widetilde{\mathbf{X}}$) needed to maximize the overlapping volume between $\Phi_u$ and $\Phi_f$.

$$\begin{bmatrix} \widetilde{\mathbf{X}} \\ 1 \end{bmatrix} = \begin{bmatrix} \mathbf{R}_z \mathbf{R}_y \mathbf{R}_x & \mathbf{T} \\ \mathbf{0} & 1 \end{bmatrix} \begin{bmatrix} \mathbf{X} \\ 1 \end{bmatrix} \tag{5-6}$$

where $\quad \mathbf{R}_x = \begin{bmatrix} 1 & 0 & 0 \\ 0 & cos\theta_x & -sin\theta_x \\ 0 & sin\theta_x & cos\theta_x \end{bmatrix} \quad ; \quad \mathbf{R}_y = \begin{bmatrix} cos\theta_y & 0 & sin\theta_y \\ 0 & 1 & 0 \\ -sin\theta_y & 0 & cos\theta_y \end{bmatrix} \quad ; \quad \mathbf{R}_z =$

$\begin{bmatrix} cos\theta_z & -sin\theta_z & 0 \\ sin\theta_z & cos\theta_z & 0 \\ 0 & 0 & 1 \end{bmatrix}; \mathbf{T} = \begin{bmatrix} t_x \\ t_y \\ t_z \end{bmatrix}$; and $t_x, t_y, t_z$ are the translations in the $x, y, z$ directions,

respectively; $\boldsymbol{\theta} = \begin{bmatrix} \theta_x \\ \theta_y \\ \theta_z \end{bmatrix}$; and $\theta_x, \theta_z, \theta_y$ are the rotation angles around the $x, y, z$ axes,

respectively.

The used part $\Phi_i(\mathbf{T}, \boldsymbol{\theta})$ has a translation variable and a rotation variable. The final part is fixed by $\Phi_f$. The intersection part ($\Phi_i$) is the intersection of the used part and the final part, given as:

$$\Phi_i(\mathbf{T}, \boldsymbol{\theta}) = \Phi_u(\mathbf{T}, \boldsymbol{\theta}) \cap \Phi_f = \min(\Phi_u(\mathbf{T}, \boldsymbol{\theta}), \Phi_f) \tag{5-7}$$

Therefore, the optimization problem of maximizing the intersection part can be mathematically formulated by optimizing $\mathbf{T}$ and $\boldsymbol{\theta}$ by minimizing the volume of intersection part with a negative sign, as shown in Equation (5-8):

$$\text{min.} \ \ f = -\int_\Omega H(\Phi_i(\mathbf{T}, \boldsymbol{\theta})) \, d\Omega \tag{5-8}$$

where $\Phi_i(\mathbf{T}, \boldsymbol{\theta}) = \Phi_u(\mathbf{T}, \boldsymbol{\theta}) \cap \Phi_f$ . Note that H() means the Heaviside function, which is defined as:

$$\begin{cases} H(\Phi) = 1 & \Phi \geq 0 \\ H(\Phi) = 0 & \Phi < 0 \end{cases} \tag{5-9}$$

The sensitivity is a part of the gradient for a single variable. For example a sensitivity $\frac{\partial f}{\partial t_x}$ of the objective function is derived through Eq. (5-10); others can be calculated similarly.

$$\frac{\partial f}{\partial t_x} = -\int_\Omega \frac{\partial H(\Phi_i(\mathbf{T}, \boldsymbol{\theta}))}{\partial \Phi_i} \frac{\partial \Phi_i}{\partial t_x} d\Omega = -\int_\Omega \delta(\Phi_i(\mathbf{T}, \boldsymbol{\theta})) \frac{\partial \Phi_i}{\partial t_x} \, d\Omega \tag{5-10}$$

$\delta()$ is the Dirac delta function, which is defined as:

$$\begin{cases} \delta(\Phi) = 0 & \Phi \neq 0 \\ \delta(\Phi) = +\infty & \Phi = 0 \end{cases} \qquad \int_{-\infty}^{+\infty} \delta(\Phi) \, d\Phi = 1 \tag{5-11}$$

This problem can be solved with a gradient-based optimization solver; the algorithm for this is shown in Table 5.2.

Figure 5.6 demonstrates an example of the intersection part extraction. The used part and the final part are represented by its level set function $\Phi_u$ and $\Phi_f$ respectively.

74

Equation (5-8) helps to find the optimal transformation to transform $\Phi_u$ to $\tilde{\Phi}_u$ with the optimized rotation angle ( $\theta_x = -90^o, \theta_y = 0^o, \theta_z = 0^o$ ) and translation ( $t_x = -20.1, t_y = -110.7, t_z = 15$). The intersection part $\Phi_i$ (Figure 5.6c) can be obtained by $\tilde{\Phi}_u \cap \Phi_f$.

Table 5.2:Algorithm of the intersection part extraction problem.

---

1. Start $\mathbf{T} = [0,0,0]^T$ and $\mathbf{\theta} = [0,0,0]^T$ as initial values and set a convergence value;

2. Calculate the sensitivity information $\frac{\partial f}{\partial t_x}, \frac{\partial f}{\partial t_y}, \frac{\partial f}{\partial t_z}, \frac{\partial f}{\partial \theta_x}, \frac{\partial f}{\partial \theta_y}, \frac{\partial f}{\partial \theta_z}$ at current point by Eq.(5-10);

3. Update each variable, as $t_x^{(k+1)} = t_x^{(k)} - \eta \frac{\partial f}{\partial t_x}$ ,where $\eta$ is the step;

4. Check for convergence. If none, go back to Step 2.

---
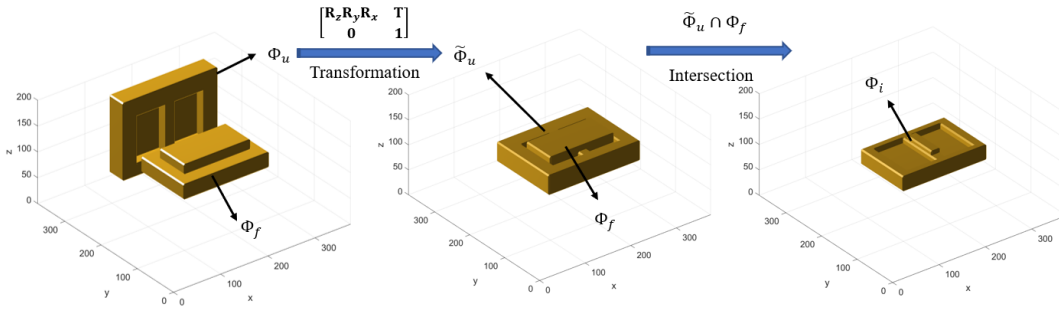


Figure 5.6: An illustration of the intersection part extraction: (a) the original used part $\Phi_u$ and final part $\Phi_f$; (b) the transformed used part $\tilde{\Phi}_u$ and final part $\Phi_f$ ; (c) the intersection part $\Phi_i$.

**5.2.1.3 Intersection Part Modification for Collision-free Remanufacturing**

The next step is to manufacture $P_u$ into $P_i$ subtractively and then deposit new materials on top to form $P_f$. However, with the PBF process, the build surface must be flat to avoid collisions between powder recoater and the part. As shown in Figure 5.7, $P_i$ should be adjusted to form a new $\overline{P_i}$ that provides a large enough flat platform to support complete

75

material deposition from $\overline{P_l}$ to $P_f$. The principle is to minimize the perturbation on $P_i$ to maintain the largest reusable material volume; see Equation (5-12).

$$\text{min.} \quad V(P_i \setminus \overline{P_l}) \tag{5-12}$$
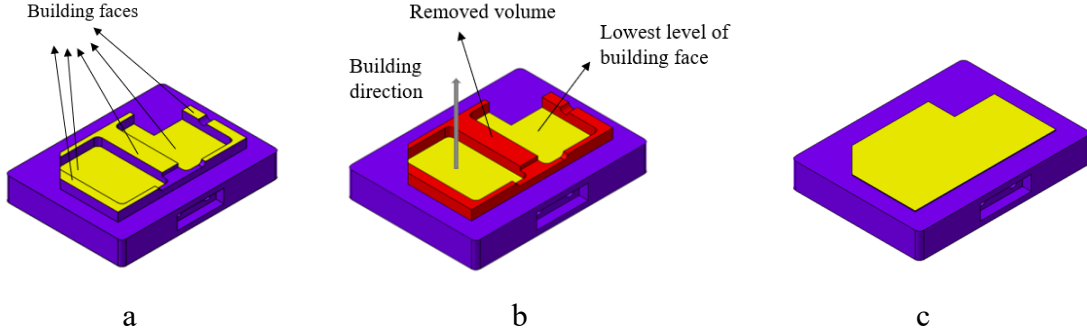


Figure 5.7: An illustration of intersection part modification: (a) the yellow areas are building faces derived by directly intersecting $P_u$ and $P_f$ ; (b) the red volume is removed for intersection part modification; (c) modified intersection part $\overline{P_l}$ with a flat build surface.

For SM and AM, assuming that the principal axis of the cutter or the laser head can only be aligned in the $\pm x, \pm y, \pm z$ directions within the global coordinate system, so that the feature recognition can be conducted within reasonable computation time. With this assumption, Equation (5-12) can be reformulated by optimizing $\overline{z}, \underline{z}, \overline{y}, \underline{y}, \overline{x}, \underline{x}$ by maximizing the bounding plane on $\pm x, \pm y, \pm z$ directions. The constraint ensures that the volume of subtracting the final part by intersection part in the boundary is less than $\varepsilon$:

$$\text{min.} \quad g = -(\overline{z} - \underline{z} + \overline{y} - \underline{y} + \overline{x} - \underline{x})$$
$$\text{s.t.} \quad \int_{\underline{x}}^{\overline{x}} \int_{\underline{y}}^{\overline{y}} \int_{\underline{z}}^{\overline{z}} H(\Phi_f / \Phi_i) \, d\Omega \leq \varepsilon \tag{5-13}$$

where $\overline{z}, \underline{z}, \overline{y}, \underline{y}, \overline{x}, \underline{x}$ indicate the coordinate bounds of the modified intersection part. $\varepsilon$ is defined as a very small positive number to improve numerical robustness.

Lagrange formulation of the optimization problem is defined in Equation (5-14):

$$L = -(\overline{z} - \underline{z} + \overline{y} - \underline{y} + \overline{x} - \underline{x})$$
$$+ \lambda \left[ \left[ \int_{\underline{x}}^{\overline{x}} \int_{\underline{y}}^{\overline{y}} \int_{\underline{z}}^{\overline{z}} H\left(\min(\Phi_f, -\Phi_i)\right) dxdydz - \varepsilon \right] \right] \qquad (5\text{-}14)$$

The gradient of the Lagrange formulation is given as:

$$\nabla L = \left[ \frac{\partial L}{\partial \overline{z}}, \frac{\partial L}{\partial \underline{z}}, \frac{\partial L}{\partial \overline{y}}, \frac{\partial L}{\partial \underline{y}}, \frac{\partial L}{\partial \overline{x}}, \frac{\partial L}{\partial \underline{x}}, \frac{\partial L}{\partial \lambda} \right]^T \qquad (5\text{-}15)$$

where $\frac{\partial L}{\partial \overline{z}}$ and $\frac{\partial L}{\partial \lambda}$ are calculated in Equations (5-16) and (5-17). The other directions of the gradient can be easily obtained, as these have similar forms to Equation (5-16).

$$\frac{\partial L}{\partial \overline{z}} = -1 + \lambda \left[ \left[ \int_{\underline{x}}^{\overline{x}} \int_{\underline{y}}^{\overline{y}} H\left(\min(\Phi_f, -\Phi_i)\right) dxdy \right] \right]_{z=\underline{z}} \qquad (5\text{-}16)$$

$$\frac{\partial L}{\partial \lambda} = \int_{\underline{x}}^{\overline{x}} \int_{\underline{y}}^{\overline{y}} \int_{\underline{z}}^{\overline{z}} H\left(\min(\Phi_f, -\Phi_i)\right) dxdydz - \varepsilon \qquad (5\text{-}17)$$

The variables $\overline{z}, \underline{z}, \overline{y}, \underline{y}, \overline{x}, \underline{x}, \lambda$ can be solved with a gradient-based optimization algorithm (Table 5.3).

Table 5.3:Algorithm of the intersection part modification problem.

---

1. Select the boundary of $\Phi_i$ as the starting point for $\overline{z}, \underline{z}, \overline{y}, \underline{y}, \overline{x}, \underline{x}$ , and select an initial value for $\lambda$.

2. Calculate the sensitivity information at the current point by Eq. (5-15).

3. Update each variable, as $\overline{z}^{(k+1)} = \overline{z}^{(k)} - \eta \frac{\partial L}{\partial \overline{z}}$ , where $\eta$ is the step.

4. Check for convergence. If none, go back to Step 2.

---

After the optimal $\bar{z}, \underline{z}, \bar{y}, \underline{y}, \bar{x}, \underline{x}$ have been obtained, the modified interaction part $\widetilde{\Phi}_i$ can be represented by:

$$\widetilde{\Phi}_i = \Phi_i \cap \Phi_b$$

$$\Phi_b = \min\left\{\bar{x} - x, x - \underline{x}, \bar{y} - y, y - \underline{y}, \bar{z} - z, z - \underline{z}\right\}$$

(5-18)

Figure 5.8 demonstrates the process of modifying the intersection part in Figure 5.6. In this case, $\bar{z}$ is the only variable being updated during optimization and the optimal $\bar{z}$ is 20 mm. The level-set function of the optimized intersection part is $\widetilde{\Phi}_i = \min\{\Phi_i, 180 - x, x, 120 - y, y, 20 - z, z\}$.
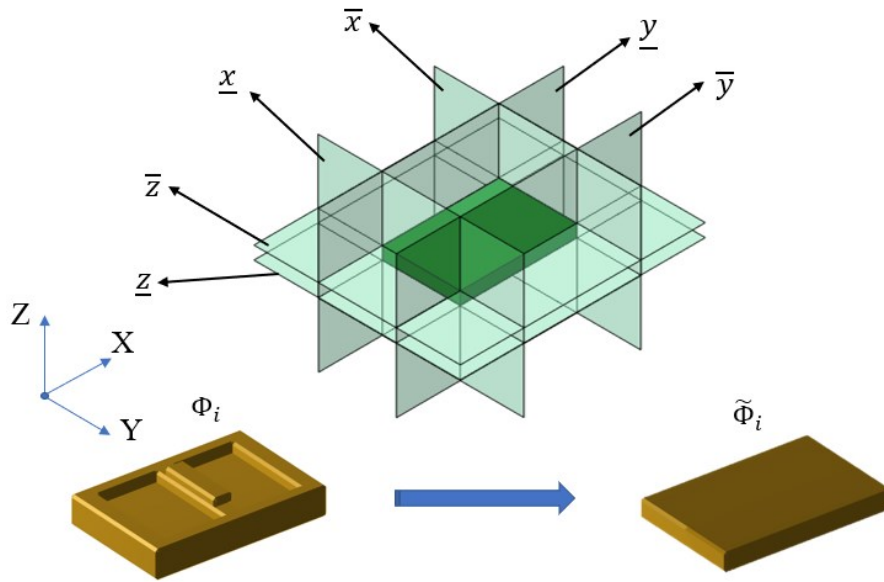


Figure 5.8: An example of modifying the intersection part.

### 5.2.1.4 Feature Extraction

A subtractive manufacturing feature group (SFG) and an additive manufacturing feature group (AFG) can be obtained by Boolean subtraction of the modified intersection part ($\widetilde{\Phi}_i$) from used part ($\Phi_u$) and final part ($\Phi_f$) respectively, via Equation (5-19).

$$\Phi_{SFG} = \Phi_u \setminus \widetilde{\Phi}_i$$

$$\Phi_{AFG} = \Phi_f \setminus \widetilde{\Phi}_i$$

(5-19)

Individual features then need to be recognized and extracted from their feature groups. Machining feature recognition comprises a large body of the literature [136]. Hence, this research does not focus on developing new machining feature recognition technology. With the help of B-rep data, the SFs can be decomposed from the SFG by a graph-based feature recognition method that is implemented in most commercial feature recognition systems; see Equation (5-20).

$$\Phi_{SFG} \rightarrow \{SF_1, SF_2, SF_3, \ldots SF_n\}$$

(5-20)

AFG is composed of both AFs and SFs. Because of the limitations of AM, it is necessary to leave sufficient over-thickness for the finishing operation to meet the tolerance and surface roughness requirements. The over-thickness is defined as the extra offset value for each deposition layer of the profile for AM process, which is left for finishing operation of SM process to meet the tight tolerance requirement and surface roughness. The over-thickness value is estimated by the required specifications of the final feature, the surface roughness generated by the AM processes and the machining conditions [88]. As a result, the modified additive feature group ($\overline{AFG}$) is updated by considering over-thickness. The $\overline{AFG}$ can be derived via Equation (5-21), where t represents the over-thickness value. The residual subtractive feature group ($\overline{SFG}$) is obtained via Equation (5-22). Similarly, the individual SFs could be recognized by a graph-based feature recognition method by Equation (5-23).

$$\Phi_{\overline{AFG}} = (\Phi_{AFG} + t) \setminus \widetilde{\Phi}_i$$

(5-21)

$$\Phi_{\overline{SFG}} = \Phi_{\overline{AFG}} \setminus \Phi_{AFG}$$

(5-22)

$$\Phi_{\overline{\mathrm{SFG}}} \rightarrow \{\mathrm{SF}_{n+1}, \mathrm{SF}_{n+2}, \mathrm{SF}_{n+3}, \ldots \mathrm{SF}_{n+m}\} \qquad (5\text{-}23)$$

## 5.2.2 Precedence Constraints

A large group of AM and SM features can be extracted from the feature recognition algorithm; however, the sequences of some operations are forced because of the topological relationship among features and also the hybrid process planning rules. Therefore, this part of deciding the process sequence is fixed without any degrees of design freedom, which should be formulated as precedence constraints in the global process sequence optimization problem. A list of rules needed to form the precedence constraints can be summarized from [88,100] and this list is given in Table 5.4.

Table 5.4: Manufacturing rules for HM.

| | |
|---|---|
| *Rule 1: "Opens-into" relationships between an additive feature and a subtractive feature*<br><br>If a subtractive feature is embedded in an additive feature, the process should have the precedence constraint of AF first and then SF. |  |
| *Rule 2: Two additive features interact with a subtractive feature*<br><br>The building and finishing sequences are related to precedence relations between two AFs and one SF. As an example, $AF_1$ interacts with the SF, and the SF interacts with $AF_2$. Because of machining tool accessibility, the SF needs to be created after building $AF_1$ and before building $AF_2$. |  |
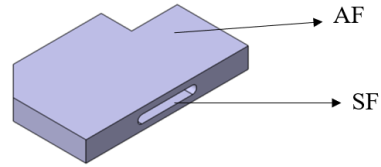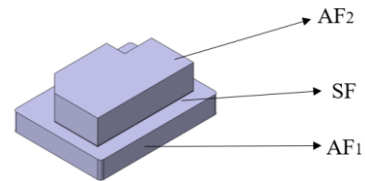
*Rule 3: "Opens-into" relationships between two subtractive features*

If a subtractive is nested in another feature, the top (nesting) feature should be machined before the bottom (nested) feature.
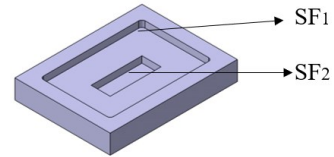
*Rule 4: Building collision*

This constraint controls the sequence between an SF and AF. For the PBF process, the build surface must be flat to avoid collision between the powder recoater and the part. Thus, AF needs to be made after SF.
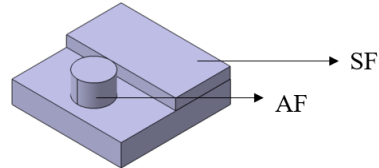
*Rule 5: Hole deburring*

This constraint controls the quality of a machined hole. After drilling a hole, burrs may remain after the operation. If the hole feature interacts with another subtractive feature, the burrs can be removed after machining. If a hole feature $SF_2$ interacts with a pocket feature $SF_1$, then the hole feature should be machined first.
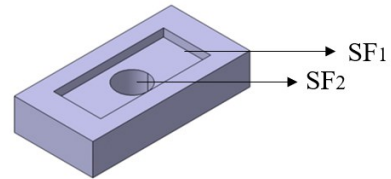
*Rule 6: Instability caused by an SF*

If the process of an SF causes instability of the part in the setup of the AM operation, then the SF must be machined after the AF process.
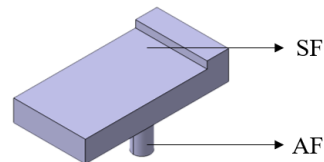
*Rule 7: Tight tolerance constraint between two SFs*

If SFs ($SF_1$, $SF_2$) are constrained by a tight tolerance relationship, they should be arranged in the same setup to eliminate system fixture errors. If this is impossible, the setup of $SF_1$ (respectively $SF_2$) requires the machine surfaces
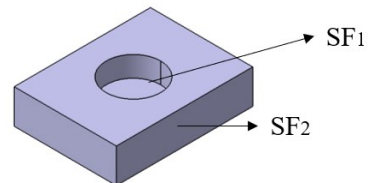
of $SF_2$ (respectively $SF_1$) to be used as locating
surfaces to position the part.

## 5.2.3 Cost Model Estimation

So far, some process sequences are still undetermined. Therefore, to facilitate global
process sequence optimization and decision-making to choose the most economical hybrid
process plan, a cost model for each feature is proposed. In this section, the cost model is
divided into the cost of SF, cost of AF and cost of change.

### 5.2.3.1 Cost of subtractive feature

The cost of SF aims to investigate the cost of each subtractive operation (e.g., roughing,
finishing). The cost includes operation cost and tool cost as follows:

$$C_{SF} = C_{hs} * t_{SF} + C_{tool} * n_{tool} \qquad (5\text{-}24)$$

where $C_{SF}$ is the total cost of an SF, $C_{hs}$ is the hourly operation cost for the machining
process, $t_{SF}$ is the machining time for the SF, $C_{tool}$ is the cost of each cutting tool, and
$n_{tool}$ is the number of tool changes.

The machining time is determined based on the material removal rate (MRR) which is
highly dependent on the cutting parameters. The cutting parameters under roughing and
finishing are different. Roughing operations aim to remove the bulk materials rapidly to
shape the workpiece approximately towards the finished form. Finishing operations are
executed after roughing or AM to improve surface quality or to meet tolerance and surface
finish requirements. Moreover, milling and drilling operations have different equations for
calculating the MRR. The following equations are proposed for machining time with
constant cutting parameters:

$$t_{SF} = \frac{V_{SF}}{MRR}$$

$$MRR_m = \frac{a_p * a_e * v_f}{60 * 10^3}$$ (5-25)

$$MRR_d = \frac{(\pi * D^2/4) * v_f}{60 * 10^3}$$

where $V_{SF}$ is the volume for the SF, $a_p$ is the axial depth of the cut, $a_e$ is the radial depth of the cut, $v_f$ is the feed rate of machining, D is the diameter of the cutting tool, and $MRR_m$ and $MRR_d$ are the material removal rates for milling and drilling, respectively.

### 5.2.3.2 Cost of additive feature

Out of the many AM technologies, the AF cost model in this article is proposed for PBF technology. Generally, PBF processes can be divided into material deposition and post-processing. For remanufacturing, the separation process can be eliminated, since the part is not built on top of a substrate. Therefore, the post-processing cost can be ignored. The study only need to consider the cost of building and of material consumption for an AF, as shown below:

$$C_{AF} = C_{ha} * t_{AF} + C_{m-AF}$$ (5-26)

where $C_{AF}$ is the total cost of an AF, $C_{ha}$ is the hourly operation cost for the AM process, $t_{AF}$ is the building time of the AF, and $C_{m-AF}$ is the cost of material consumption. Instead of adopting a build time estimator integrated with commercial AM software, this study uses a generic formula for calculating build times by using a linear regression model [152], as shown in Equation (5-27).

$$t_{AF} = a_0 + a_1 * N_L + a_2 * V_{AF} + a_3 * S_{AF}$$

$$N_L = \frac{H_{AF}}{T_L}$$ (5-27)

where $N_L$ is the number of layers built, $H_{AF}$ is the height of the AF, $T_L$ is the pre-defined layer thickness, and $V_{AF}$ and $S_{AF}$ are the volume and surface area for the AF, respectively. The material cost is calculated by the material consumed for building the AF part and its support structure, as:

$$C_{m-AF} = (V_{AF}\rho + V_{AF-s}\overline{\rho})C_{material}^{unit} \qquad (5\text{-}28)$$

where, $V_{AF}$ is the volume of the AF, $V_{AF-s}$ is the volume of the support structure for the AF part, $\rho$ is the material density, $\overline{\rho}$ is the material density of the support structure, and $C_{material}^{unit}$ indicates the price per unit of metal powder.

### 5.2.3.3 Cost of Change

The cost of change is incurred by machine changes, orientation changes, or tool changes between two consecutive operations. The machine, candidate orientation, and candidate tool information for each operation are given in advance to enable estimation of the change costs between any two operations. CM, CS and CT indicate the machine change cost, the re-orientation cost, and the tool change cost respectively, and the details are given below:

*Machine change cost:*

When the machine needs to be changed between two consecutive operations, the machine setup of the subsequent operation is required. For a PBF machine, the setup process consists of uploading the building file to the machine, setting the process parameters, and filling the machine with argon gas. For a CNC machine, the setup process includes tool loading, workpiece fixing, and warming up the machine. The machine change costs for PBF and CNC are formulated as follows:

$$CM_{PBF} = C_{ha} * t_{PBF-setup} + C_{argon}$$
$$CM_{CNC} = C_{hs} * t_{CNC-setup} \qquad (5\text{-}29)$$

where $C_{ha}$ is the hourly operation cost for the PBF process, $t_{PBF-setup}$ is the setup time for the PBF machine, $C_{argon}$ is the argon gas cost, $C_{hs}$ is the hourly operation cost for the CNC process, and $t_{CNC-setup}$ is the setup time for the CNC machine.

In the proposed method, a machine set $p \in P = \{1,2,\ldots,P\}$ (p indicates the index of the machines) is mapped to a set of machine change costs (CM) and the element $(CM_p)$ represents the setup cost of the $p^{th}$ machine. The machine change set can be represented as follows:

$$CM = [CM_1 \quad \cdots \quad CM_p], \text{ where } p \in P = \{1,2,\ldots,P\} \tag{5-30}$$

For example, a CNC machine (index 1) and a PBF machine (index 2) are used in a hybrid process. $CM_1$ represents the cost incurred in the PBF machine's setup, which is \$180. $CM_2$ is \$12.5, which is the cost of setting up the CNC machine. In this case, the machine set is $P = \{1,2\}$, and the machine cost set is $CM = [180 \quad 12.5]$.

*Re-orientation cost:*

A re-orientation change occurs when the orientation of the workpiece is switched within the same machine. The re-orientation for a PBF machine also requires machine setup processes, so it incurs the same cost as a machine change. For a CNC machine, the re-orientation requires workpiece fixing (see Equation (5-31)).

$$CR_{PBF} = CM_{PBF}$$
$$CR_{CNC} = C_{hs} * t_{CNC-re} \tag{5-31}$$

where $t_{CNC-re}$ is the re-orientation time for the CNC machine. Similarly, the re-orientation cost for different machines can be calculated via Equation (5-32).

$$CR = [CR_1 \quad \cdots \quad CR_p], \text{ where } p \in P = \{1,2,\ldots,P\} \tag{5-32}$$

Suppose that a CNC machine (index 1) and a PBF machine (index 2) are used in a hybrid process. $CR_1$ represents the cost incurred by the PBF machine's setup, which is $180. $CR_2$ is $4, which is the cost of setting up the CNC machine. Therefore, the re-orientation cost set is $CR = [180 \quad 4]$.

*Tool change cost:*

Tool changes happen between two adjacent operations with the same SM machine and the same orientation. It is worth noting that, tool changes never happen in a PBF machine. In order to keep the optimization formulas consistent, the tool change cost is set as an infinite value. It can avoid processing invalid tool changes in the PBF machine during solving the optimization problem. For CNC machining, the tool change cost is formulated as:

$$CT_{CNC} = C_{hs} * t_{CNC-tc} \tag{5-33}$$

where $t_{CNC-tc}$ is the tool change time for the CNC machine. The tool change cost set is formulated as the following equation:

$$CT = [CT_1 \quad \cdots \quad CT_p], \text{ where } p \in P = \{1,2,\ldots,P\} \tag{5-34}$$

For instance, a CNC machine (index 1) and a PBF machine (index 2) are used in a hybrid process. $CT_1$ represents the tool change cost, which is represented as a very large positive number. $CR_2$ is $4, which is the cost of the CNC machine's tool change. Therefore, the tool change cost set is $CR = [\infty \quad 4]$.

## 5.2.4 Sequence Optimization

The global process sequence optimization problem is formulated as an integer programming model. A general formulation of the precedence-constrained operation sequencing problem (PCOSP) [99] is modified in the proposed method to optimize the HM process sequence. The definitions of parameters and decision variables in the model are given in Table 5.5.

Table 5.5: Definitions used in sequence optimization.

*Parameters*:

N  The feature set $i, j \in N = \{1, 2, \ldots, N\}$

P  The machine set $p \in P = \{1, 2, \ldots, P\}$

Q  The tool set $q \in Q = \{1, 2, \ldots, Q\}$

R  The TAD set $r \in R = \{1, 2, \ldots, R\}$

F  The feature set, where $i, j \in F = \{1, 2, \ldots, F\}$ in any feasible sequence

$M^p$  The machine operation cost index; for example, $M_i^p$ indicates machine operation cost for feature $i$ using machine p

$T^q$  The tool cost index; for example, $T_i^q$ indicates tool cost for feature $i$ using tool $q$

CM  The machine change cost set

CR  The re-orientation cost set

CT  The tool change cost set

*Decision variables:*

$m_i^p$  Selected machine for the feature; for example, $m_i^p = 1$ if machine $p$ is used for feature $i$ and $m_i^p = 0$ otherwise

$t_i^q$  Selected tool for the feature; for example, $t_i^q = 1$ if tool $q$ is used for feature $i$; $t_i^q = 0$ otherwise

$d_i^r$  Selected TAD for the feature; for example, $d_i^r = 1$ if TAD $q$ is used for feature $i$; $t_i^q = 0$ otherwise

$x_{ij}$  Process sequence between features; for example, $x_{ij} = 1$ if feature $i$ is operated before feature $j$; $x_{ij} = 0$ otherwise

In the objective function, $f_1$ represents the total machine cost and tool cost. Specifically, for AFs, the powder consumption during the building process is counted and added in the tool cost. $f_2$ is the total cost of changing machines. $f_3$ formulates the total setup cost caused by changing the orientation of the workpiece in the CNC and PBF machine. $f_4$ calculates the total cost of changing the cutting tool.

Objective function:

$$\text{min.} \quad C = f_1 + f_2 + f_3 + f_4$$

$$f_1 = \sum_{i=1}^{N} \sum_{p=1}^{P} M_i^p m_i^p + \sum_{i=1}^{N} \sum_{q=1}^{Q} T_i^q t_i^q$$

$$f_2 = \sum_{i=1}^{N} \sum_{j=1}^{N} \sum_{p=1}^{P} \left( CM_p m_j^p \right) x_{ij} \left( 1 - \sum_{p=1}^{P} m_i^p m_j^p \right), i \neq j$$

$$f_3 = \sum_{i=1}^{N} \sum_{j=1}^{N} \sum_{p=1}^{P} \left( CR_p m_j^p \right) x_{ij} \left( 1 - \sum_{p=1}^{P} m_i^p m_j^p \sum_{r=1}^{R} d_i^r \, d_j^r \right), i \neq j$$

$$f_4 = \sum_{i=1}^{N} \sum_{j=1}^{N} \sum_{p=1}^{P} \left( CT_p m_j^p \right) x_{ij} \left( 1 - \sum_{p=1}^{P} m_i^p m_j^p \sum_{q=1}^{Q} t_i^q t_j^q \right), i \neq j$$

(5-35)

*Constraints:*

$$x_{ij} + x_{ji} \leq 1; \quad \forall i, j \in N \tag{5-36}$$

$$\sum_{p=1}^{P} m_i^p = 1; \sum_{q=1}^{Q} t_i^q = 1; \sum_{r=1}^{R} d_i^r = 1; \quad \forall i \in N \tag{5-37}$$

$$\sum_{j=1}^{N} x_{ij} = 1; \sum_{j=1}^{N} x_{ji} = 1; \quad \forall i \in N \tag{5-38}$$

$$x_{ij} + x_{ji} = 1; \quad \forall i, j \in F \tag{5-39}$$

$$x_{ij} = (1,0); \ m_i^p = (1,0); \ t_i^q = (1,0), d_i^r = (1,0) \quad \forall i, j \in N; \forall p \in$$
$$P; \forall q \in Q; \forall r \in R \tag{5-40}$$

Equation (5-36) means that there is, at most, one operation between two features. Equation (5-37) stipulates that one operation in a process plan should be performed with only one machine, one TAD, and one tool. Equation (5-38) indicates that one operation is performed before or after a feature. Equation (5-39) ensures the precedence relationships given by the HM rules. Equation (5-40) limits the variables to integer values only.

With this mathematical formulation, the PCOSP can be solved through branch and bound, linear programming, and dynamic programming as exact approaches.

## 5.3 Case Study and Discussion

In this section, the proposed method is illustrated with a remanufacturing case study. As shown in Figure 5.9, there are two used parts, one of which will be selected to build the final part. Two scenarios for the used part A and B are generated as two remanufacturing process plans. The proposed cost-driven decision system is applied to optimize the process plans of both scenarios and facilitate the final decision. Specifically, the pocket (p1) and the surfaces (s1 to s3) require high surface precision. Surfaces (s1 to s3) are constrained with the tolerances of the dimensions X1 and X2. The dimension of pockets (p1) is constrained with X3, the position of it is constrained with X4.



a        b        c        d
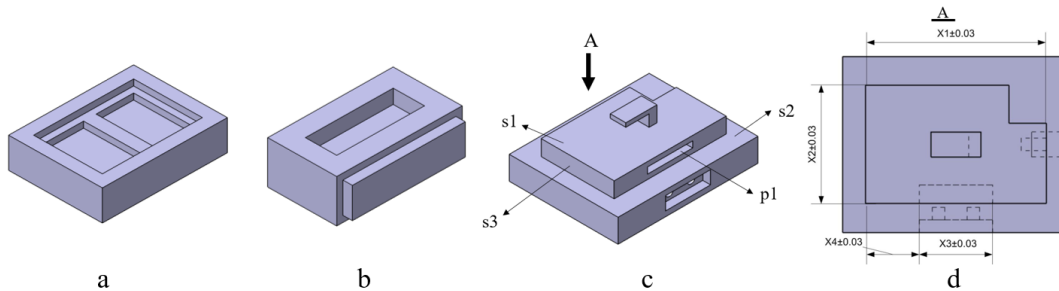
Figure 5.9: Test parts: (a) the used part A and (b) the used part B, and (c) the final part, (d) the top view of the final part and some important dimensions discussed in the case study.

The CSG for two used parts and final part are built by discrete level set functions on a design domain $D$ (150*150*50) with grid size $\Delta x$ (0.5mm) in Figure 5.10, Figure 5.11 and Figure 5.12.

Used part A: $\Phi_{u1} = \min(\Phi_{cube1}, -\Phi_{cube2}, -\Phi_{cube3}, -\Phi_{cube4})$
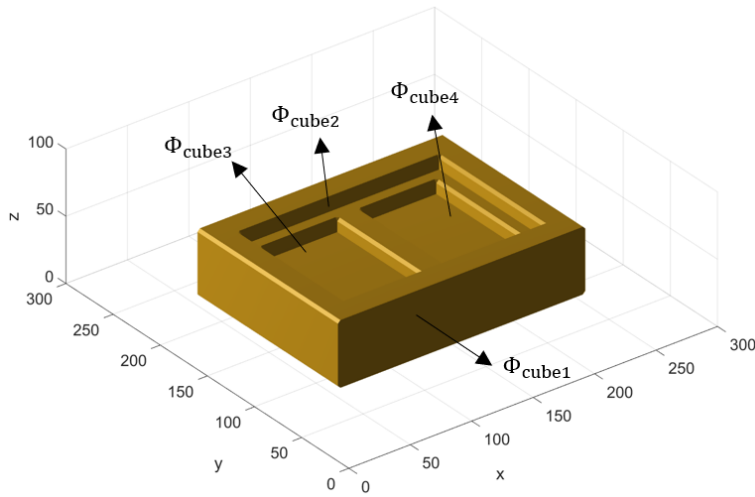


Figure 5.10: Discrete level-set representations of the used parts in Scenario A.

Used part B: $\Phi_{u2} = \min\{\max(\Phi_{cube1}, \Phi_{cube2}), -\Phi_{cube3}\}$
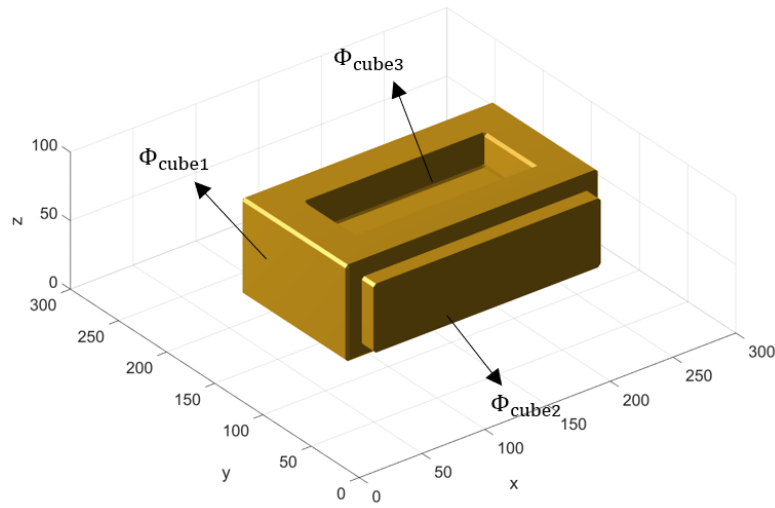
Figure 5.11: Discrete level-set representations of the used parts in Scenario B.

$$\text{Final part: } \Phi_f = \min \left\{ \begin{array}{c} \max(\Phi_{cube1}, \Phi_{cube2}, \Phi_{cube6}), -\Phi_{cube3}, \\ -\Phi_{cube4}, -\Phi_{cube5}, -\Phi_{cube7}, \\ -\Phi_{cyl1}, -\Phi_{cyl2}, -\Phi_{cyl3}, -\Phi_{cyl4} \end{array} \right\}$$
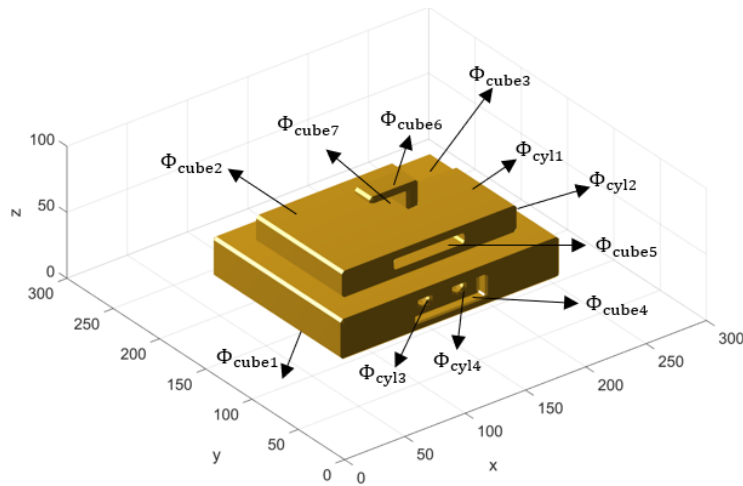


Figure 5.12: Discrete level-set representations of the final part.

In order to maximize the intersection volume, the intersection part extraction algorithm is implemented for the used parts. The results of optimizing the translation and rotation vectors of the used parts in Scenario A and Scenario B are listed in Table 5.6 and the

optimal intersection parts are shown in Figure 5.13. Their convergence histories are presented in Figure 5.14.

Table 5.6: The optimal translation and rotation for test parts.

| | Translation (mm) | | | Rotation (°) | | |
| | $t_x$ | $t_y$ | $t_z$ | $\theta_x$ | $\theta_y$ | $\theta_z$ |
|---|---|---|---|---|---|---|
| Scenario A: | 4.07 | 4.21 | 8.33 | 0 | 0 | 0 |
| Scenario B: | -20.18 | 10.17 | 4.32 | 0 | 0 | 180.02 |

Next step, the intersection parts are modified with respect to the constraints of the PBF process. The results for the optimal variables and the modified intersection parts are given in Figure 5.15. Specifically, in Scenario A, $\bar{z}$ is the only variable which has non-zero sensitivity, so the result of the modified intersection part is bounded by $\Phi_b = (48 - z)/\Delta x$ . In Scenario B, both $\bar{z}$ and $\bar{x}$ have sensitivities in optimization, and the intersection part is updated with bound of $\Phi_b = \min{(67 - z, 209 - y)}/\Delta x$ . The convergence histories of this optimization problem are presented in Figure 5.16.



a                                                    b
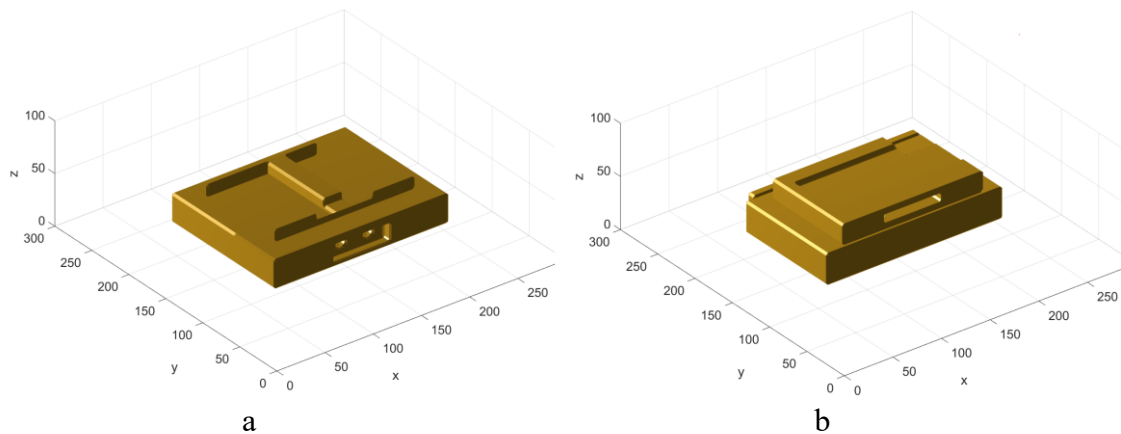
Figure 5.13: Optimal intersection parts in (a) Scenario A and (b) Scenario B.
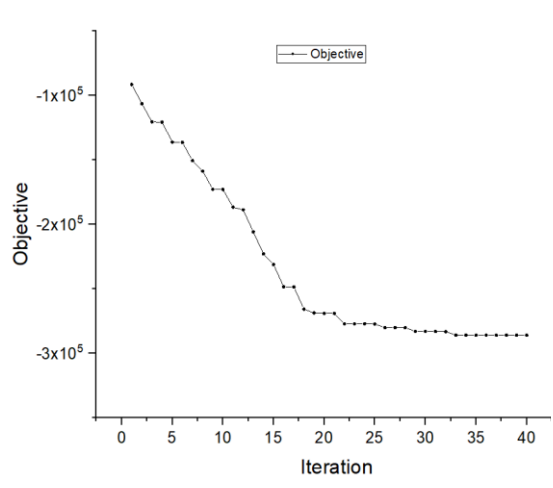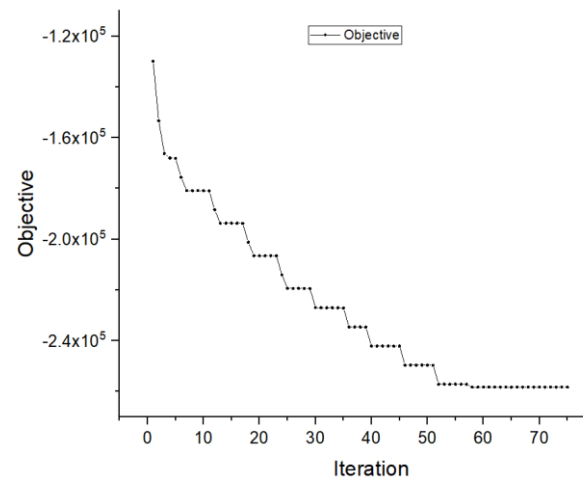
Figure 5.14: Convergence histories of the intersection part maximization problem of (a) Scenario A and (b) Scenario B.
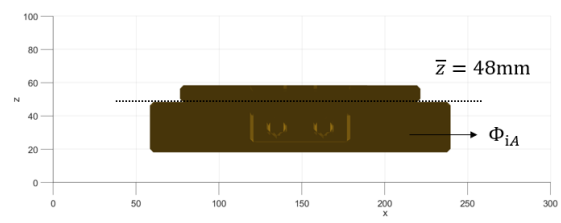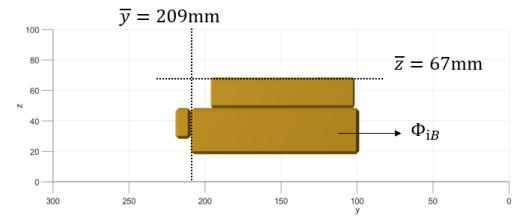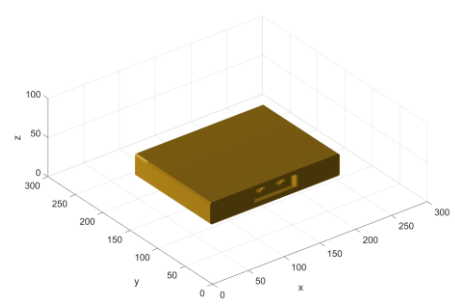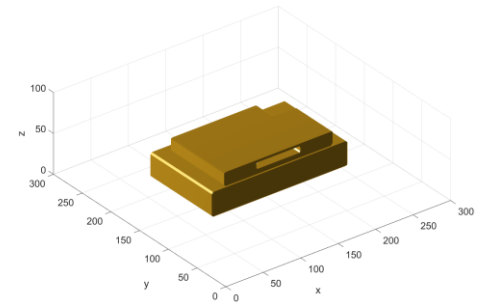


Figure 5.15: Boundaries for modifying the intersection part in (a) Scenario A and (b) Scenario B; the results of the modified intersection part in (c) Scenario A and (d) Scenario B.
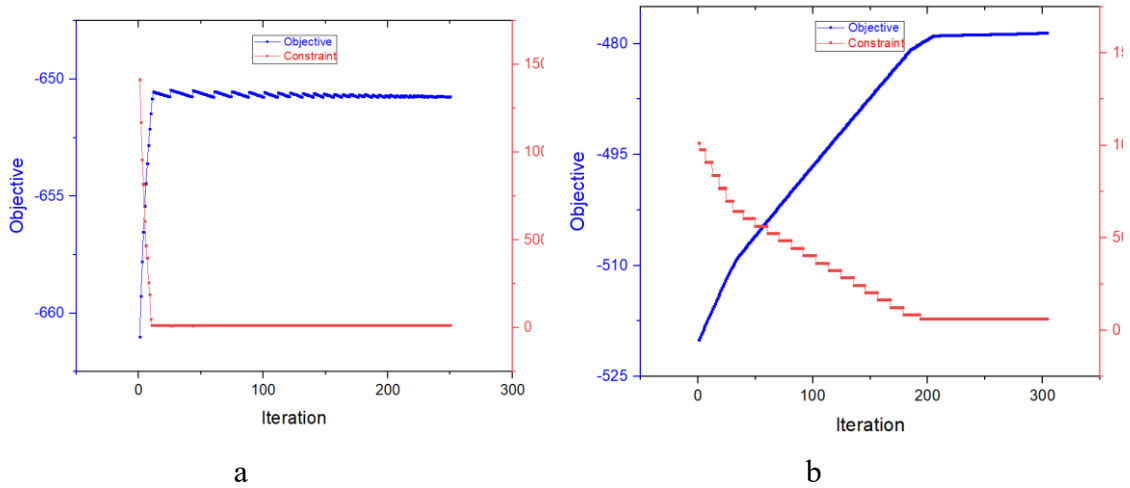
Figure 5.16: Convergence histories of the intersection part modification problem of (a) Scenario A and (b) Scenario B. (the units of the objective *y*-axis are mm).

With the modified intersection parts, the SFG and AFG are obtained and individual SFs and AFs are extracted from their corresponding group. The results of feature extraction are presented in Figure 5.17. In the case of Scenario A (Figure 5.17), there are two AFs ($AF_1$ and $AF_2$) and ten SFs ($SF_1$ to $SF_{10}$). There are two points to notice: $SF_7$ and $SF_9$ remove the support structures of $AF_1$ and $AF_2$ respectively; $AF_1$ and $AF_2$ should not be combined in a single AM process, since s1 of the final part (see Figure 5.9) requires a high surface quality, which can be achieved through a finishing process ($SF_{10}$). In Scenario B (Figure 5.18), there are four AFs ($AF_1$ to $AF_3$) and eleven SFs ($SF_1$ to $SF_{11}$). $AF_1$ and $AF_2$ have different building directions from $AF_3$ and $AF_4$, which will cause a re-setup to switch the build direction of the workpiece in PBF. Another point worth mentioning is that $SF_9$ and $SF_{10}$ need for surface finishing to meet the precision requirement of p1 in the final part (see Figure 5.9).
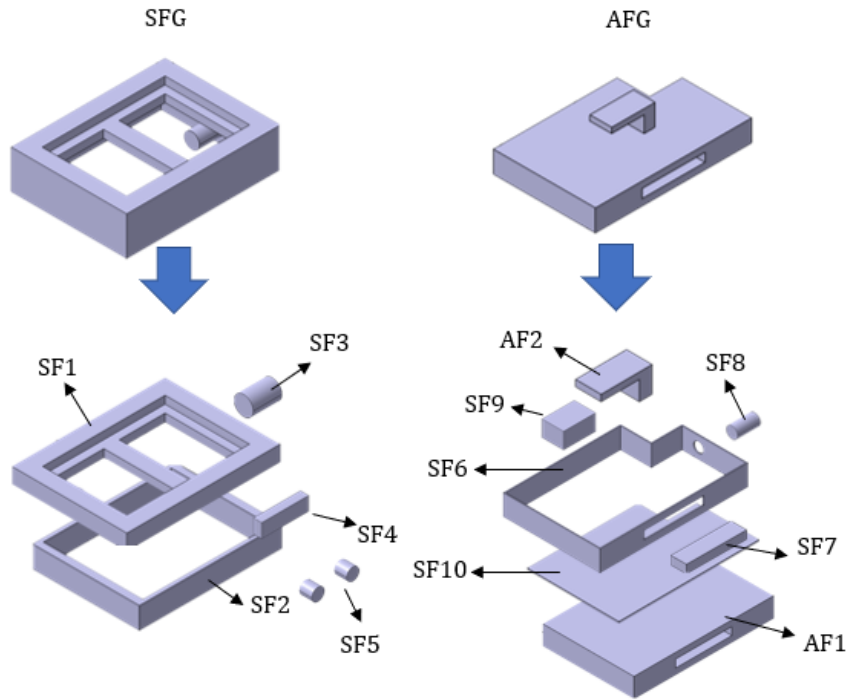
Figure 5.17: The SFG, AFG, and individual SFs and AFs for Scenario A.
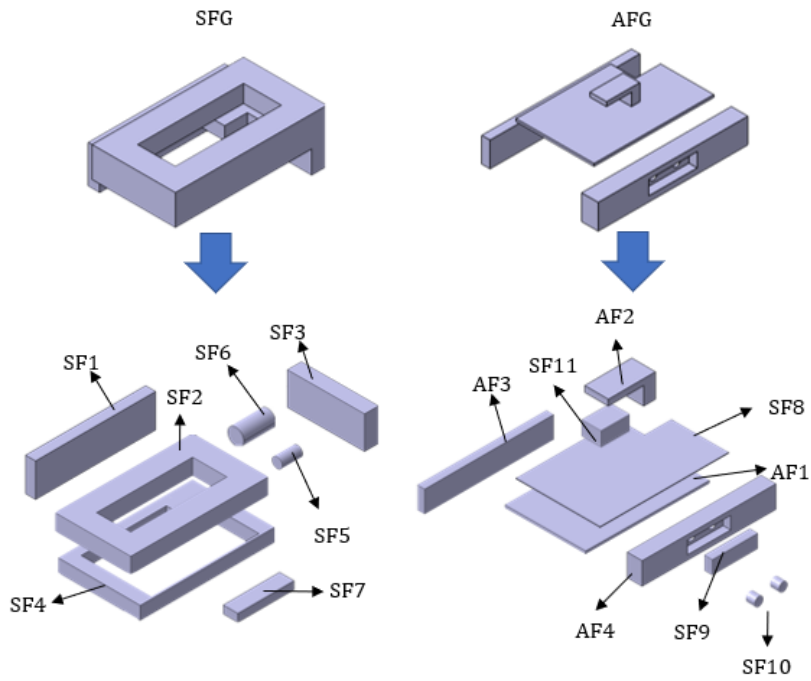


Figure 5.18: The SFG, AFG, and individual SFs and AFs for Scenario B.

95

The precedence constraints are expressed by the precedence-directed graphs in Figure 5.19. The black links indicate the precedence relations between features and red links represent the tolerance constraints between features. For Scenario A (Figure 5.19a), the precedence constraints of $AF_1 \rightarrow SF_6$, $AF_1 \rightarrow SF_7$, $AF_1 \rightarrow SF_8$, $AF_1 \rightarrow SF_{10}$, and $AF_2 \rightarrow SF_9$, follow Rule 1. The precedence relationships of $AF_1 \rightarrow SF_{10} \rightarrow AF_2$ follow Rule 2, which avoids collisions between the cutter and $AF_2$. $SF_1 \rightarrow AF_1$ is a result of following Rule 4. $SF_5$ is required to be machined before $SF_4$, which reduces the hole-deburring issues described in Rule 5. According to Rule 7, $SF_7$ should have the same machining setup of $SF_6$. In the process plan for Scenario B (Figure 5.19b), the precedence relationships $AF_4 \rightarrow SF_{10}$, $AF_2 \rightarrow SF_{11}$ are constrained by Rule 1. The relationships for $AF_1 \rightarrow SF_8 \rightarrow AF_1$ follow Rule 2. $SF_2 \rightarrow AF_1$ and $SF_1 \rightarrow AF_1$ follow Rule 4 to avoid building collisions. Rule 6 is applied in $SF_{10} \rightarrow SF_9$. $SF_7$ must have the same setup of $SF_4$ due to Rule 7.
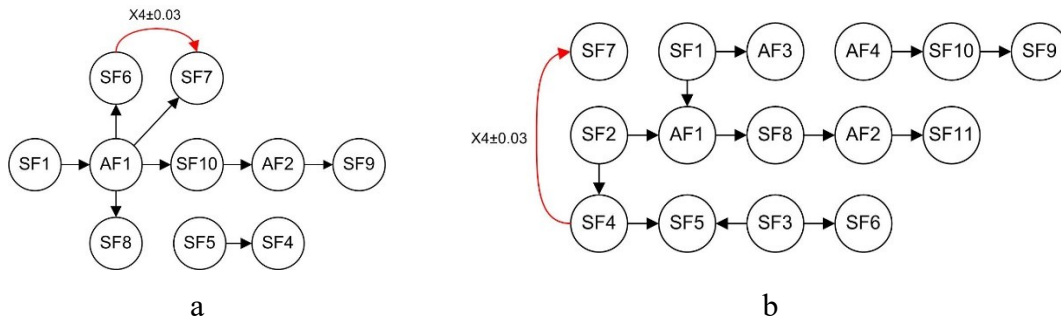


Figure 5.19: The precedence-directed graphs for (a) Scenario A, and (b) Scenario B.

The operation costs and change costs are formulated according to the proposed cost models. Several parameters are used in these cost estimations, which are shown in Table 5.7. The manufacturing resources, including the available tools and machines, are listed in Table 5.8.

The PCOSP can be solved by LINGO with a branch-and-bound solver. The optimized process plans of Scenario A and Scenario B are presented in Table 5.9 and Table 5.10, respectively. The minimum HM costs are $ 2421.29 and $ 1272.15 for Scenario A and

Scenario B, respectively. Therefore, in this case study, it can be determined that it is more economical to apply Scenario B in remanufacturing according to the optimized process plan.

Table 5.7: Data used for cost modeling.

| Parameter | Value |
|---|---|
| $C_{hs}$ | 25$/h |
| $C_{tool}$ | 5 $ |
| $C_{ha}$ | 100 $/h |
| $T_L$ | 0.05 mm |
| $\rho$ | $4.42 * 10^{-6}$ $kg/mm^3$ |
| $\bar{\rho}/\rho$ | 0.4 |
| $a_0$ | -1.29 h |
| $a_1$ | $4.53 * 10^{-3}$ h/mm |
| $a_2$ | $1.8 * 10^{-4}$ $h/mm^3$ |
| $a_3$ | $-1.33 * 10^{-4}$ $h/mm^2$ |
| $C_{material}^{unit}$ | 450 $/kg |
| $t_{PBF-setup}$ | 1.5 h |
| $C_{argon}$ | 20 $/h |
| $t_{CNC-setup}$ | 0.5h |
| $t_{CNC-re}$ | 0.33 h |
| $t_{CNC-tc}$ | 0.17 h |

Table 5.8: Manufacturing resources.

| Tool ID | Tool type | Diameter (mm) | Length of cut (mm) |
|---|---|---|---|
| T1 | End mill | 20 | 50.8 |
| T2 | End mill | 10 | 38 |
| T3 | End mill | 5 | 21 |
| T4 | Drill | 5 | 26 |
| T5 | Drill | 10 | 47 |
| T6 | PBF | - | - |
| Machine ID | Machine type | | |
| M1 | CNC machine | | |
| M2 | PBF machine | | |

Table 5.9: Optimal process plan for Scenario A.

| Scenario A | | | | |
|---|---|---|---|---|
| Sequence | Features | Machine | TAD | Tool |
| 1 | SF1 | M1 | +z | T1 |
| 2 | SF2 | M1 | +z | T1 |
| 3 | AF1 | M2 | +z | T6 |
| 4 | SF10 | M1 | +z | T2 |
| 5 | AF2 | M2 | +z | T6 |
| 6 | SF9 | M1 | +y | T3 |
| 7 | SF5 | M1 | +y | T4 |
| 8 | SF8 | M1 | +x | T4 |
| 9 | SF3 | M1 | +x | T4 |
| 10 | SF6 | M1 | +y | T2 |
| 11 | SF7 | M1 | +y | T3 |
| 12 | SF4 | M1 | +y | T3 |

Table 5.10: Optimal process plan for Scenario B.

| Scenario B | | | | |
|---|---|---|---|---|
| Sequence | Features | Machine | TAD | Tool |
| 1 | SF2 | M1 | +z | T1 |
| 2 | SF1 | M1 | +z | T2 |
| 3 | SF8 | M1 | +z | T2 |
| 4 | AF3 | M2 | -y | T6 |
| 5 | AF1 | M2 | +z | T6 |
| 6 | AF4 | M2 | +y | T6 |
| 7 | SF4 | M1 | +y | T2 |
| 8 | SF7 | M2 | +y | T3 |
| 9 | SF3 | M1 | +x | T2 |
| 10 | SF6 | M1 | +x | T5 |
| 11 | SF5 | M1 | +x | T6 |
| 12 | AF2 | M2 | +z | T6 |
| 13 | SF11 | M2 | +y | T3 |
| 14 | SF10 | M2 | +y | T5 |
| 15 | SF9 | M2 | +y | T3 |
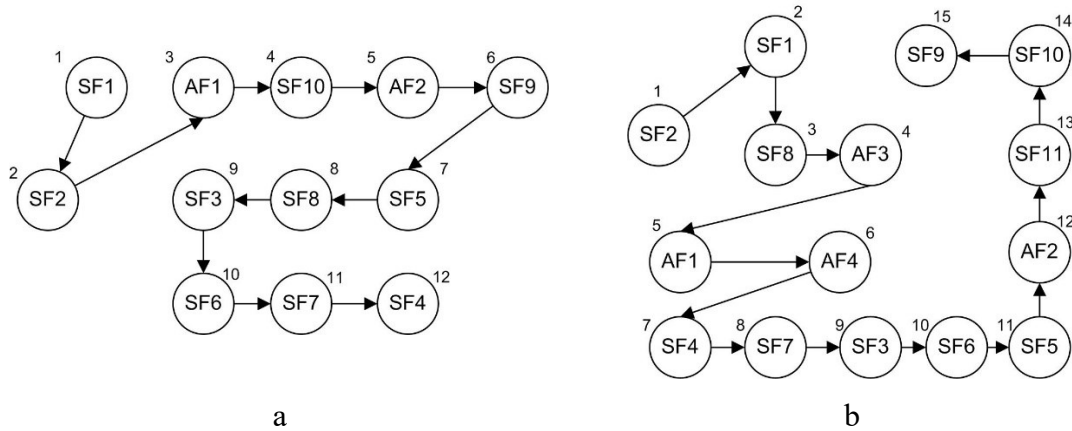
Figure 5.20: The optimal plans for (a) Scenario A, and (b) Scenario B.

Although the primary focus of this study is on the process planning of HM in a remanufacturing context, it is valuable to discuss the cost of production with other manufacturing strategies. The hybrid solution is needed to be compared with other solutions if the final part is manufactured from raw material rather than used parts via AM and SM.

With the single PBF or CNC processes, the costs for each process needed to produce the final part are listed in Table 5.11. It is obvious that the manufacturing cost of PBF is much higher than the cost of the remanufacturing strategy. By contrast, the CNC process seems to be a more economical solution. However, the CNC process is difficult to form complex geometries (Figure 5.21a) or internal structures (Figure 5.21b). In addition, remanufacturing is more environmentally friendly than the conventional strategy, wherein the existing part is recycled instead of the polluting disposal [79].

Another worth discussion point is that to decide the feasibility of the proposed remanufacturing process, not only cost but quality and productivity should be considered. In the PBF process, many process parameters can affect the porosity, microstructure and mechanical properties of the built part, such as scanning speed, layer temperature, power, layer height, etc. In addition, the selection of material is critical to determine the quality of the AM part. For the different quality requirements of the AM part, the variations of

process parameters and materials can change the cost. In machining, surface roughness plays an important role in the evaluation of machining accuracy. Machining parameters including spindle speed, feed rate, depth of cut and selection of cutting tool affect surface roughness. This study is only focusing on the cost of PBF and machining processes with fixed parameters. However, to implement the proposed method in a real application, the determination of parameters of PBF and machining processes will be studied for the quality requirement in the industry.

Table 5.11: Manufacturing cost for the single PBF and CNC process.

| PBF process | Setup time (h) | Argon gas cost ($) | Build time (h) | Material cost ($) | Building cost ($) |
|---|---|---|---|---|---|
| | 1.5 | 30 | 21.15 | 1918 | 2121 |

| CNC process | Setup time (h) | Stock cost ($) | Machining feature number | Re-orientation time (h) | Machining cost ($) |
|---|---|---|---|---|---|
| | 0.5 | 353 | 8 | 0.66 | 30.42 |
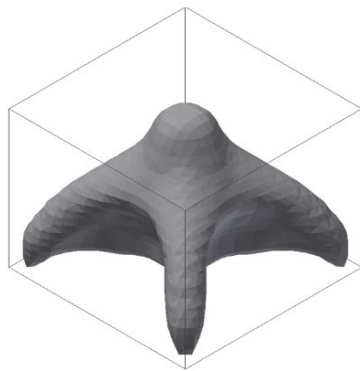
a
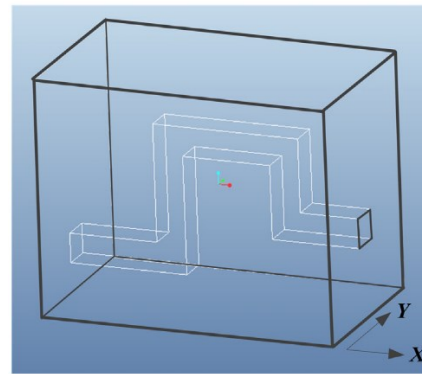
b

Figure 5.21: (a) A part with complex geometries (from academic research [92]) and (b) a part with internal structures (from academic research [131]).

## 5.4 Conclusions

Modern HM has emerged through mixing AM and SM to provide a more flexible, productive, and capable manufacturing approach. Since it makes full use of the individual advantages of AM and SM to add or remove features flexibly, HM increases the ability to remanufacture to a higher level. However, there are still some research gaps in HM-based remanufacturing. The motivation of this study is to address two challenging problems, namely that AM and SM feature extraction relies heavily on manual operations that lack algorithm support, and that the process planning result is non-unique and a quantitative evaluation mechanism is missing to support optimal decision-making.

In order to address these two issues, this study proposes an efficient cost-driven decision-making method for hybrid additive–subtractive remanufacturing. The main contribution of this study consists of the automated AF and SF recognition process and the cost-driven HM process plan optimization. The level-set based geometry representation and the detailed procedures and algorithms used to conduct the feature recognition process have been illustrated. The HM rules are formulated into a precedence-directed graph as constraints. With the carefully developed HM cost model, the process planning job is converted to a PCOSP and is solved by a branch-and-bound solver. The best scenario for remanufacturing can be determined accordingly.

# Chapter 6: Collision-free Process Planning of Integrated CNC-DED System for Remanufacturing

## 6.1 Overview

HM system synergistically integrates AM and SM processes within a single workstation (see Figure 6.1), has gained a lot of attention from academia and industry [111]. HM can capitalize on the strengths of independent techniques, whilst minimizing their disadvantages. At the same time, it has the potentials to enable remanufacturing technologies to achieve further improvement because it can to remove and add features flexibly. From Section 2.3, the integrated HM systems are reviewed in industrial and academic perspectives. It can be concluded that most of the single platform workstations for HM processes are integrating subtractive CNC machining and additive DED. However, these machines indicate rare support for the automation process planning for hybrid operations. The HM hardware technologies are striding ahead, whereas the process planning software to support their incredible capabilities are falling behind. For this reason, an increasing level of interest in research on process planning for HM has been witnessed over recent years, which is listed in Section 2.3. From these research results, it can be identified that SM is mostly playing a role as post-machining for AM in the HM process. Therefore, it is complicated to be applied directly in the remanufacturing, since SM is not only post-machining but also including geometric forming as AM process in remanufacturing. In addition, in remanufacturing context, the collision of the DED nozzle and workpiece is a critical issue because the deposition platform is not a simple geometry during remanufacturing.
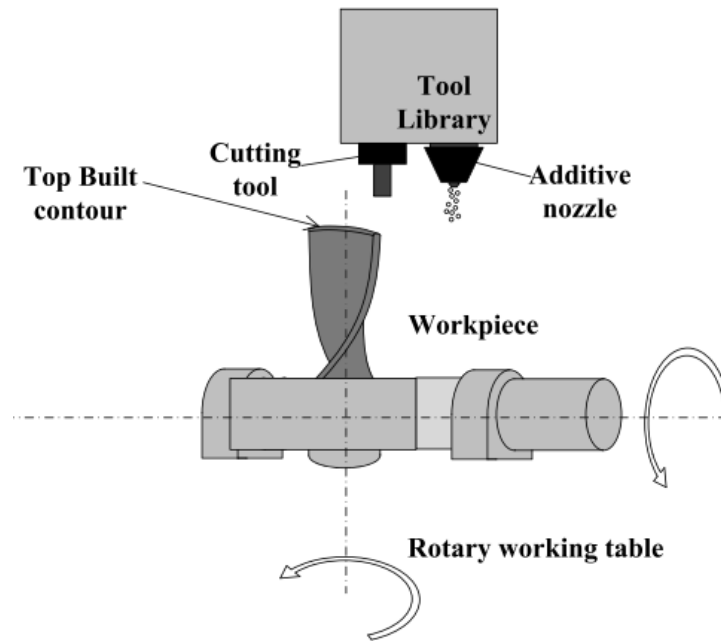
Figure 6.1: The configuration of the workstation for the hybrid machine (from academic research [153]).

This chapter is aiming to develop a method that provides automated feature extraction and cost-driven process planning for an integrated DED-CNC machine. The main contributions in this chapter are list as follows:

- Both primitive and free-form features are modelled in level set-based representations for the automated feature extraction which facilitate the process planning for HM remanufacturing;

- A collision-free DED-CNC process planning method is developed, resulting in the minimal cost in HM remanufacturing process;

- The defect and damaged area of the used part are considered to form a pre-machining feature in the process planning, which is an issue rarely addressed in the previous studies of process planning for remanufacturing.

## 6.2 Additive and Subtractive Feature Extraction

In this work, the level set function method is implemented to describe models with primitive and freeform surfaces. The flowchart of the additive and subtractive feature extraction method is proposed in Figure 6.2.
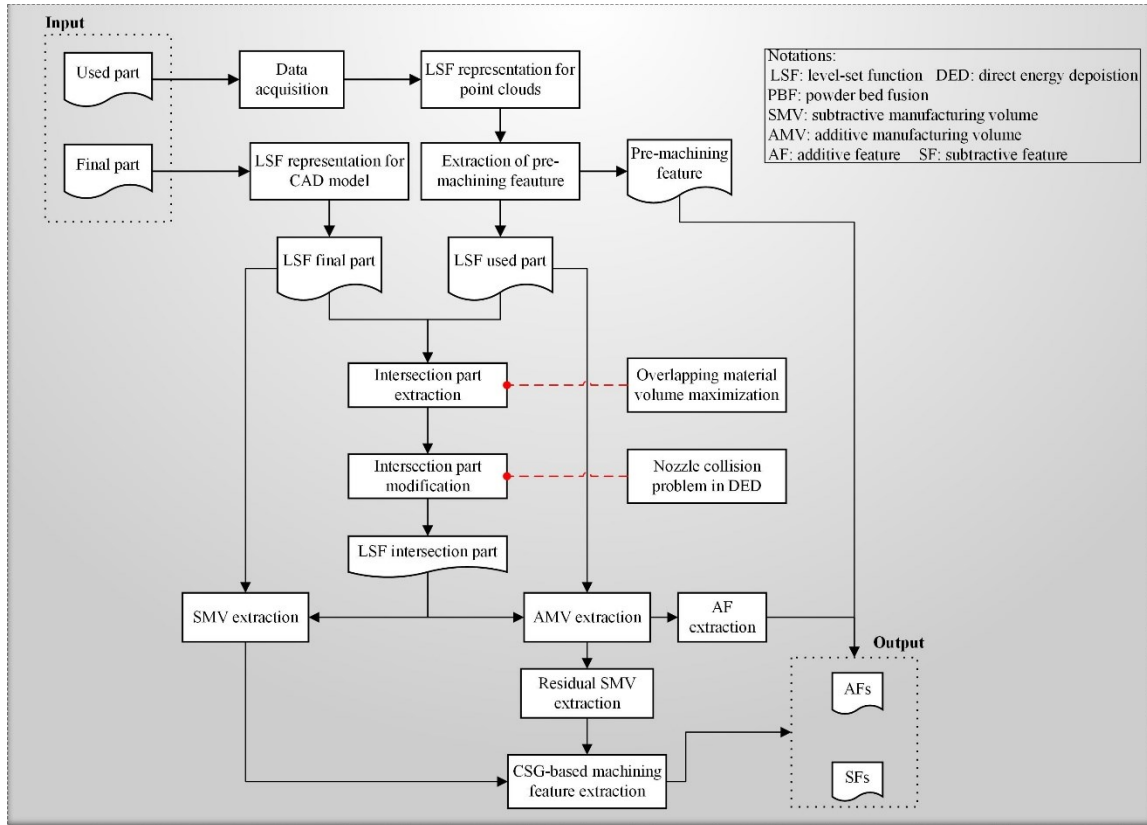


Figure 6.2: The flowchart of the proposed AF and SF extraction method for the remanufacturing process.

### 6.2.1 Level Set Function Representation for the CAD Model

Level set function $\Phi(\mathbf{X})$ $(R^n \rightarrow R)$ describes the geometry in an implicit form, as shown in Equation (6-1).

$$\begin{cases} \Phi(\mathbf{X}) > 0, & \mathbf{X} \in \Omega/\partial\Omega \\ \Phi(\mathbf{X}) = 0, & \mathbf{X} \in \partial\Omega \\ \Phi(\mathbf{X}) < 0, & \mathbf{X} \in D/\Omega \end{cases} \tag{6-1}$$

where $\Omega/\partial\Omega$ is the material domain, $D/\Omega$ is the void, $\partial\Omega$ is the structural boundary.

In the level set function-based modelling approach, the 3D model is constructed by bounding the boundary surfaces, as:

$$\Phi(\mathbf{X}) = \min\{\Phi_1, \Phi_2, \Phi_3, \dots, \Phi_n\} \tag{6-2}$$

As an example, the cube with $(x_0, y_0, z_0)$ as the center coordinates and $(Hx, Hy, Hz)$ as the lengths on the *x,y,z* axis can be represented by bounding six planer surfaces of $\Phi_1 = \frac{Hx}{2} - (x - x_0) = 0, \Phi_2 = \frac{Hx}{2} + (x - x_0) = 0, \Phi_3 = \frac{Hy}{2} - (y - y_0) = 0, \Phi_4 = \frac{Hy}{2} + (y - y_0) = 0, \Phi_5 = \frac{Hz}{2} - (z - z_0) = 0, \Phi_6 = \frac{Hz}{2} + (z - z_0) = 0$, as shown in Figure 6.3.
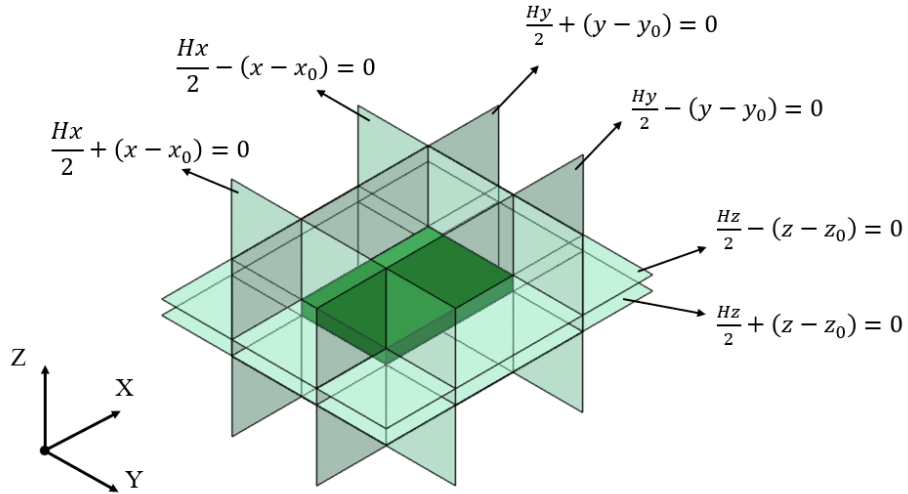


Figure 6.3: An example of a discrete level set representation for a cube.

This work focus on the level set function modelling for freeform geometries. From Equation (6-2), it can be manifested that finding the implicit forms for boundary surfaces is the most crucial work for the level set-based modelling approach. Algebraic techniques

based on elimination theory enable the conversion of parametric expression to its implicit expression $\Phi(\mathbf{X}) = 0$. Elimination theory investigates the conditions under that the sets of parametric expressions have common roots. The vanishing of the resultant is a necessary and sufficient condition for the parametric expressions to have a common non-trivial root. The implicitization of parametric geometry is based on the construction of these resultants.

A freeform 2.5D geometry can be constructed by extruding its freeform profile. As an example, in this study, the Bezier curve is implemented to represent the freeform profile. The parametric form of the Bezier curve is shown as:

$$F(u) = \sum_{i=0}^{n} B_{i,n}(u)\overline{P}_i \qquad (6\text{-}3)$$

where $F(u) = [f_x(u), f_y(u)]$, $\overline{P}_i = [\bar{p}_i^x, \bar{p}_i^y]$, $B_{i,n}(u) = C(n,i)u^i(1-u)^{n-i}$, $C(n,i)$ is the binomial coefficient: $C(n,i) = \frac{n!}{i!(n-i)!}$, $n$ is the degree of the curve, and $i$ is the number of control points, $\overline{P}_{ix}$ and $\overline{P}_{iy}$ are $x$ and $y$ coordinates of the control point.

By following elimination theory, the implicit form of the Bezier curve $\Phi_{curve}(\mathbf{X})$ can be obtained by eliminating the parameter $u$ between the parametric expressions in Eq. (6-3) by letting the resultant of them to be equal to zero.

As an example, a cubic Bezier curve is constructed by three control points: $\overline{P}_0 = (0,0), \overline{P}_1 = (40,220), \overline{P}_2 = (200,40)$ and $\overline{P}_3 = (0,0)$. By implementing the elimination theory, the implicit form for the Bezier curve can be obtained and the contour figure is shown in Figure 6.4a. Then, the 2.5D freeform shape can be modelled by $\Phi(\mathbf{X}) = \min(\Phi_{curve}, \Phi_{top}, \Phi_{bottom})$, where $\Phi_{top} = 157.5 - z$ and $\Phi_{bottom} = z - 122.5$. see Figure 6.4b.

a                          b
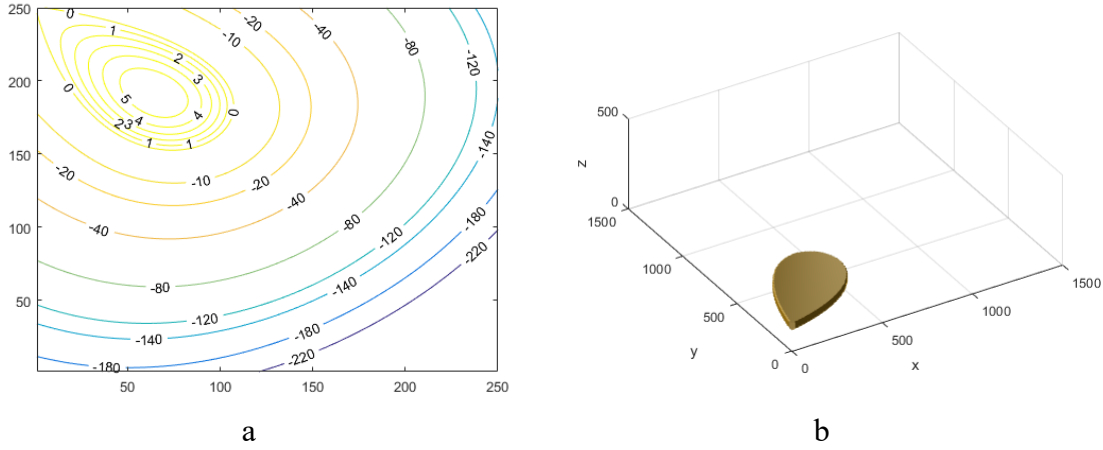
Figure 6.4: An example of a level set representation for 2.5D Bezier curve shape: (a) the contour of the Bezier curve in the level set form (note: the value is divided by 10e7); (b) 2.5D Bezier curve shape.

The parametric Bezier surface is extended from Bezier curve to $u$ and $v$ directions, as follows:

$$F(u,v) = \sum_{i=0}^{n} \sum_{j=0}^{m} B_{i,n}(u) B_{j,m}(v) \overline{P}_{i,j} \qquad (6\text{-}4)$$

where $F(u,v) = \left[f_x(u,v), f_y(u,v), f_z(u,v)\right]$ and $\overline{P}_{i,j} = [\bar{p}_{i,j}^x, \bar{p}_{i,j}^y, \bar{p}_{i,j}^z]$.

Analogously, the elimination theory can help to find the implicit form for the parametric expression in Equation (6-4). A Bezier surface is modelled by 3*3 control points; the level set form of this surface is shown in Figure 6.5a. The Bezier shape is bounded with planar surfaces $\Phi_1 = x - 200, \Phi_2 = 600 - x, \Phi_3 = y - 200, \Phi_4 = 600 - y$, see Figure 6.5b.

107
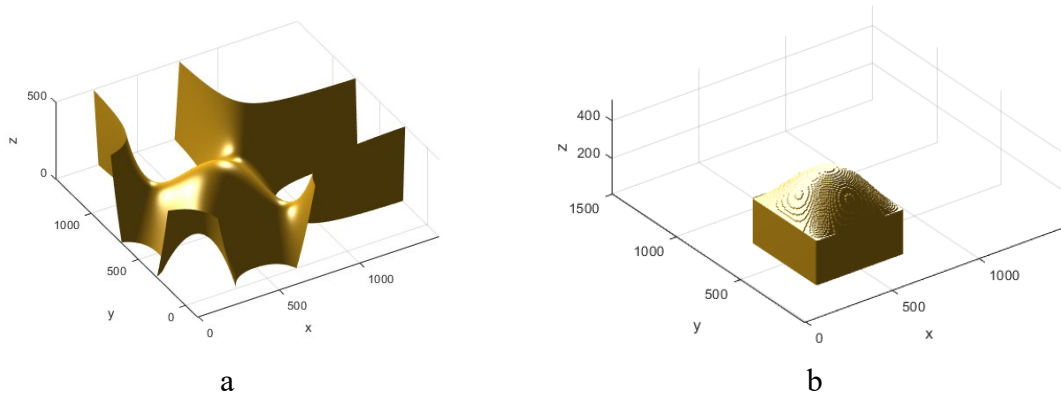
Figure 6.5: An example of a level set representation for (a) Bezier surface; (b) Bezier shape with boundaries.

The complex geometry can be constructed through Boolean operations on the level-set functions. However, this representation will cause non-differentiable problems in numerical calculation. R-functions can combine level functions of a complex structure into a new smooth level set function by operations of R-conjunction $\wedge$ and R-disjunction $\vee$, which are equivalent to Boolean operations $\cap$ and $\cup$ [154]. The operations of R-functions are defined as:

$$
\begin{aligned}
\text{Unite: } \Phi_1 \cup \Phi_2 &= \max(\Phi_1, \Phi_2) = \Phi_1 + \Phi_2 + \sqrt{\Phi_1{}^2 + \Phi_2{}^2} \\
\text{Intersect: } \Phi_1 \cap \Phi_2 &= \min(\Phi_1, \Phi_2) = \Phi_1 + \Phi_2 - \sqrt{\Phi_1{}^2 + \Phi_2{}^2} \\
\text{Subtract: } \Phi_1 \setminus \Phi_2 &= \min(\Phi_1, -\Phi_2) = \Phi_1 - \Phi_2 - \sqrt{\Phi_1{}^2 + \Phi_2{}^2}
\end{aligned}
\tag{6-5}
$$

## 6.2.2 Level Set Function Representation for Point Clouds

For a given used part, data acquisition is the first step to digitalize the part to point clouds. Therefore, the other situation is that we have the point cloud as the geometry input. To converting the point cloud data to the level set function model, the surface fitting techniques can be applied to obtain the parameters of surfaces and these parameters are used to forming the level set function representations. In this study, random sample consensus (RANSAC) surface fitting [71] is employed for surface fitting. The pseudocode for the forming level set function representation of the point clouds is given in Table 6.1.

Figure 6.6 provides two examples of the surface fitting for cylindrical surfaces and sphere from point clouds. The colour scale bars indicate the distance of each point to the fitted surface. The parameters of fitted surfaces are utilized for forming the level set functions through the proposed algorithm.

Table 6.1: Pseudocode of the forming level set function representation of point clouds.

---

**Input:** point clouds of the used part P

Set the max distance and max angular variation for fitting

$i = 1$

Remaining points $P_{m,i} \leftarrow P$

For the plane fitting, cylinder fitting, cone fitting, sphere fitting, free-form surface fitting:

      While there are enough points for supporting surface fitting in $P_{m,i}$:

            Parametric surface parameters $S_i \leftarrow$ surface fitting from $P_{m,i}$

            Converting the parametric surface to implicit function: $\Phi_i \leftarrow S_i$

            $i = i + 1$

            Remove the points $S_i$ which fit from remaining points to form new remaining points $P_{m,i}$

Forming the level set function representation from collected implicit functions by Boolean operations: $\Phi_u \leftarrow \{\Phi_1, \dots, \Phi_m\}$

End

**Output:** level set function representation of the used part $\Phi_u$

---

For construction level set functions for freeform surface, the surface fitting for freeform surface techniques can be employed. For example, the non-uniform rational basis spline (NURBS) surface fitting from point clouds has steps as: (a) parameterization of knot vectors; (b) determination of boundary condition; (c) calculation of control points; (d) construction of NURBS surface. Since the surface fitting for freeform surface is a well developed area and it is not the contribution in this study; the method used for NURBS surface fitting is presented in Appendix.

$$\Phi_{cylinder} = 8.13^2 - (x - 3.008)^2 - (y - 5.014)^2$$

$$\Phi_{sphere} = 6.043^2 - (x - 2.995)^2 - (y - 4.987)^2 - (z - 7.002)^2$$

a             b
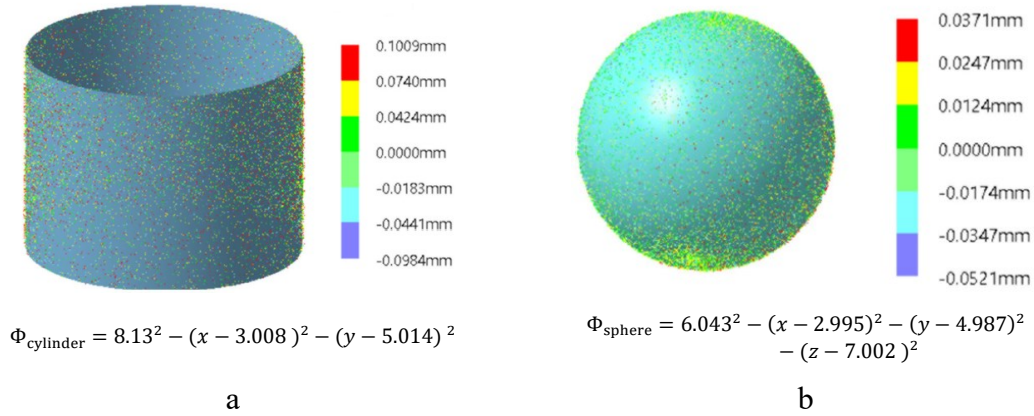
Figure 6.6: (a) Cylindrical surface fitting result and level set function; (b) Sphere fitting result and level set function.

## 6.2.3 Extraction of Pre-Machining Feature

In the repairing process, the defects on the damaged part need to be machined into a surface cavity. This cavity is to be refilled by the deposition of materials to recover the local geometry of the part. Equivalently, in terms of the remanufacturing process, it is necessary to carve out defects from the damaged part to eliminate the perturbation for the remanufacturing process planning caused by the defects. This study define the machining feature to carve out defects as a *pre-machining feature* since it has a similar concept as the pre-machining in the traditional machining process to remove the imperfections of the stock.

To construct the pre-machining feature, the first step is to segment surface defects from 3D scan data. In this work, random walks for unorganized point cloud segmentation [37] is adopted, since it does not rely on strong assumptions made on the characteristics of the expected defect or the geometry of the surrounding area. The algorithm segments defect areas on a weighted, undirected *k*-nearest neighbour graph (k-NNG) defined by local changes in point cloud properties. An example of the defect segmentation from point clouds by the random walks algorithm is shown in Figure 6.7. In the figure, the blue points indicate the points without defects and red points refer to the points on the defective area.

110
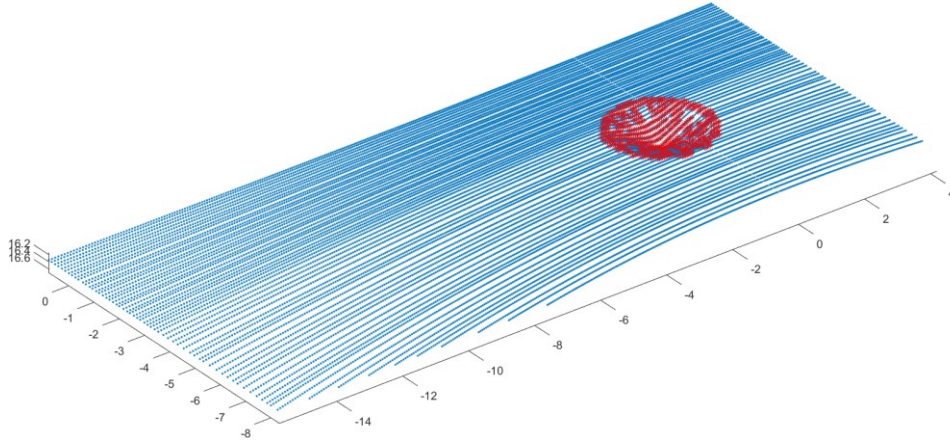
Figure 6.7: An example of defect segmentation from point cloud by the random walks algorithm.
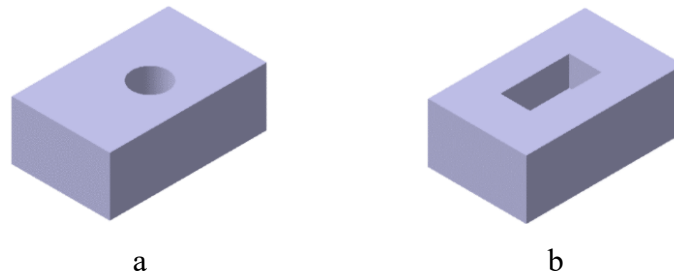


Figure 6.8: (a) Hole; (b) Rectangular pocket.

Different machining features can be applied to carve out the defect area. This study only investigates two basic machining features for the sake of simplicity. It is trivial to extend the method for other machining features. The hole and rectangular pocket are shown in Figure 6.8, and the level set function to represent these features is presented in Equation (6-6).

Hole: $\Phi = \min\left\{[R^2 - (x - x_0)^2 - (y - y_0)^2], \frac{H}{2} - (z - z_0), \frac{H}{2} + (z - z_0)\right\}$

Rectangular pocket: $\Phi = \min\left\{\frac{Hx}{2} - (x - x_0), \frac{Hx}{2} + (x - x_0), \frac{Hy}{2} - (y - y_0), \frac{Hy}{2} + (y - y_0), \frac{Hz}{2} - (z - z_0), \frac{Hz}{2} + (z - z_0)\right\}$

(6-6)

111

where $(x_0, y_0, z_0)$ are the center coordinates of the feature, $(Hx, Hy, Hz)$ is the length on the $x,y,z$ axis, $H$ is the height of the hole.

It is worth investigating the type and parameters of the machining feature, which leads to minimal materials being carved out. Meanwhile, the machining feature must remove all the defects. The problem can be mathematically formulated as a constrained optimization problem. For a given machining feature, the optimization problem is solving the optimal parameters. The objective function is minimizing the volume of the given machining feature by integrating $dxdydz$ in the material domain, referred to as Equation (6-7).

$$\text{min.} \quad f(\boldsymbol{a}) = \int_{\Omega} \text{H}(\Phi(\mathbf{X}, \boldsymbol{a})) \, dxdydz \tag{6-7}$$

where H() is the Heaviside function, $\Phi()$ is the level set function for the given machining feature, $\mathbf{X} = (x, y, z)$, $\mathbf{a} = (a_1, \dots, a_n)$ which indicates the parameters for the given machining feature.

To satisfy the condition that all defects are removed, the defective points need to be enclosed by the machining feature. Assuming there are defect points $(\boldsymbol{p}_1, \boldsymbol{p}_2, \dots, \boldsymbol{p}_M)$, series of constraints are formulated as in Equation (6-8) and the schematic plot is presented in Figure 6.9.

$$\text{s.t.} \quad g_i(\boldsymbol{a}) = \Phi(\boldsymbol{p}_i, \boldsymbol{a}) \geq 0, \quad i \in \{1, \dots, M\} \tag{6-8}$$

Lagrange formulation of this problem is written as:

$$\begin{aligned}
\mathcal{L}(a_1, &\dots, a_n, \lambda_1, \dots, \lambda_n, \eta_1, \dots, \eta_n) \\
&= f(a_1, \dots, a_n) - \sum_{i=1}^{M} \lambda_i \{g_i(a_1, \dots, a_n) - \eta_i^2\}
\end{aligned} \tag{6-9}$$

where $\lambda_i$ is the $i$-th Lagrange multiplier and $\eta_i$ is the $i$-th slack variable.

112

The sensitivity $\frac{\partial \mathcal{L}}{\partial a_1}$ of the Lagrange formulation is derived through Equation (6-10); others can be calculated similarly.

$$\frac{\partial f}{\partial a_1} = \int_\Omega \frac{\partial H(\Phi(\mathbf{X}, \boldsymbol{a}))}{\partial \Phi} \frac{\partial \Phi}{\partial a_1} d\Omega = \int_\Omega \delta(\Phi(\mathbf{X}, \boldsymbol{a})) \frac{\partial \Phi}{\partial a_1} d\Omega \qquad (6\text{-}10)$$

where $\delta()$ is the Dirac delta function.

This problem can be solved with a gradient-based optimization solver by updating the variables $a_1, \dots, a_n, \lambda_1, \dots, \lambda_n, \eta_1, \dots, \eta_n$ with their corresponding sensitivity.
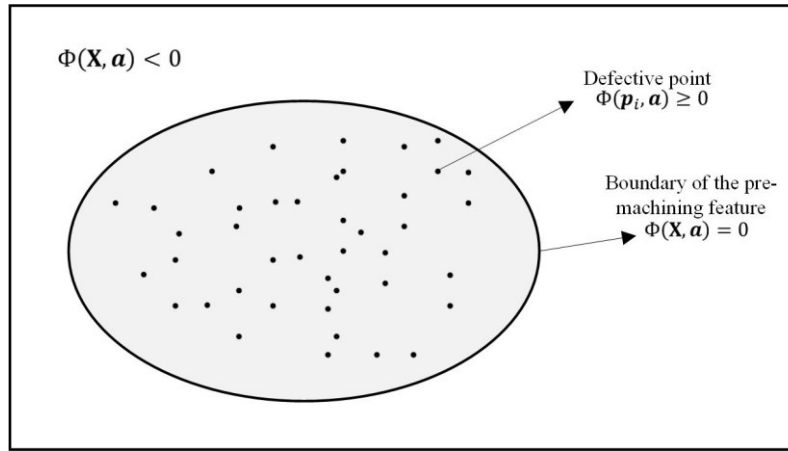


Figure 6.9: Schematic plot: the defective points are enclosed by the boundary of the pre-machining feature

Examples of the optimal parameters of a hole and a rectangular pocket features are illustrated in Figure 6.10. From the two pre-machining features, the minimal volume of the feature can be determined. In this example, the hole feature has a volume of $3.657 \text{ mm}^3$ and rectangular pocket has the volume of $4.3665 \text{ mm}^3$. Therefore, the hole feature is optimal for pre-machining.
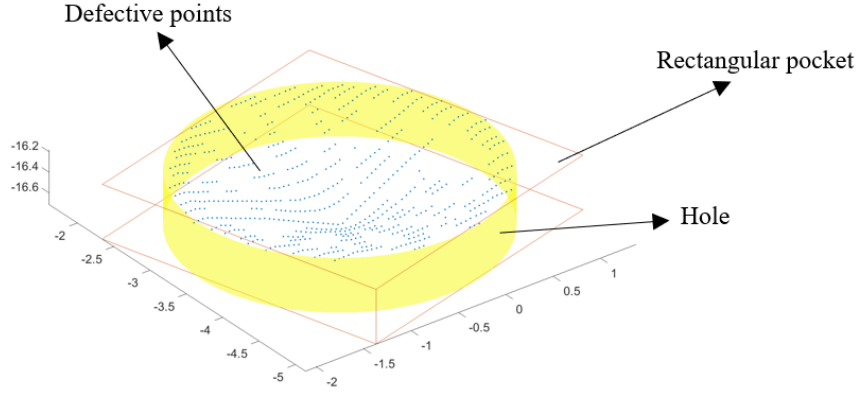
Figure 6.10: Examples of hole and rectangular features for defective points.

## 6.2.4 Intersection Part Extraction

As the level set function of the used part and final part are formulated, the relative position needs to be identified between two solid models to prepare for feature extraction. The objective is to maximize the overlapping material volume because the cost of AM is strongly affected by the volume of the new material to deposit.

$\Phi_u$ and $\Phi_f$ are the level set functions of the used part and the final part, respectively, within the global coordinate system $\mathbf{X} = (x, y, z)$. $\widetilde{\mathbf{X}}$ is a local coordinate system attached to the used part. Through Equation (6-11), an optimization problem can be formulated to figure out the translation and rotation of the local coordinate system ($\widetilde{\mathbf{X}}$) needed to maximize the overlapping volume between $\Phi_u$ and $\Phi_f$.

$$\begin{bmatrix} \widetilde{\mathbf{X}} \\ 1 \end{bmatrix} = \begin{bmatrix} \mathbf{R}_z(\theta_x)\mathbf{R}_y(\theta_y)\mathbf{R}_x(\theta_z) & \mathbf{T}(t_x, t_y, t_z) \\ \mathbf{0} & 1 \end{bmatrix} \begin{bmatrix} \mathbf{X} \\ 1 \end{bmatrix} \tag{6-11}$$

where $\mathbf{R}_x$, $\mathbf{R}_y$, $\mathbf{R}_z$ are the rotation matrix along $x,y,z$ direction with the variables of $\theta_x, \theta_z, \theta_y$, $\mathbf{T}$ is the translation matrix with the variables of $t_x, t_y, t_z$.

The used part $\Phi_i(\theta_x, \theta_z, \theta_y, t_x, t_y, t_z)$ has translation variables and rotation variables. The final part is fixed by $\Phi_f$. The intersection part ($\Phi_i$) is the intersection of the used part and the final part, given as:

$$\Phi_i(\theta_x, \theta_z, \theta_y, t_x, t_y, t_z) = \Phi_u(\theta_x, \theta_z, \theta_y, t_x, t_y, t_z) \cap \Phi_f$$
$$= \min(\Phi_u(\theta_x, \theta_z, \theta_y, t_x, t_y, t_z), \Phi_f) \tag{6-12}$$

The maximization optimization problem can be formulated of maximizing the intersection part by optimizing the variables $\theta_x, \theta_z, \theta_y, t_x, t_y, t_z$ :

$$\min. \quad f(\theta_x, \theta_z, \theta_y, t_x, t_y, t_z)$$
$$= -\int_\Omega H(\Phi_i(\mathbf{X}, \theta_x, \theta_z, \theta_y, t_x, t_y, t_z)) \, d\Omega \tag{6-13}$$

The sensitivity $\frac{\partial f}{\partial t_x}$ of the objective function is derived through Equation (6-14); others can be calculated similarly.

$$\frac{\partial f}{\partial t_x} = -\int_\Omega \frac{\partial H(\Phi_i(\theta_x, \theta_z, \theta_y, t_x, t_y, t_z))}{\partial \Phi_i} \frac{\partial \Phi_i}{\partial t_x} d\Omega$$
$$= -\int_\Omega \delta(\Phi_i(\theta_x, \theta_z, \theta_y, t_x, t_y, t_z)) \frac{\partial \Phi_i}{\partial t_x} \, d\Omega \tag{6-14}$$

This problem can be solved with a gradient-based optimization solver. In the gradient-based optimization algorithm, the $(\theta_x, \theta_z, \theta_y, t_x, t_y, t_z)$=(0,0,0,0,0,0) is set as the initial values. Generally, to prevent a local optimum issue, a multi-start strategy is suggested, i.e., to parallelly run the optimization program with a different initial guess of variables.

## 6.2.5 Intersection Part Modification for Collision-Free Remanufacturing

The geometry of intersection part geometry is not generally acceptable for AM processes. Figure 6.10 illustrates collision problems in the DED process, and the material deposition

nozzles may have collisions with the intersection part. Therefore, it is crucial to modify the intersection part by analyzing the tool accessibility constraints of the DED process.
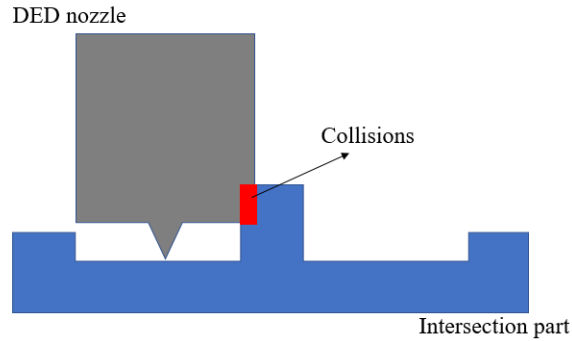


Figure 6.11: DED nozzle induced collisions.

Initially, the intersection part and DED nozzle are formulated as $\Phi_i$ and $\Phi_n$ by the level-set representation, respectively. In addition, the deposited material volume by AM is represented as $\Phi_d = \Phi_f/\Phi_i$, as shown in Figure 6.12. The voxel representations for $\Phi_i$, $\Phi_n$ and $\Phi_d$ are computing by applying Heaviside functions $V_i = \text{H}(\Phi_i)$, $V_n = \text{H}(\Phi_i)$, and $V_d = \text{H}(\Phi_d)$, separately.
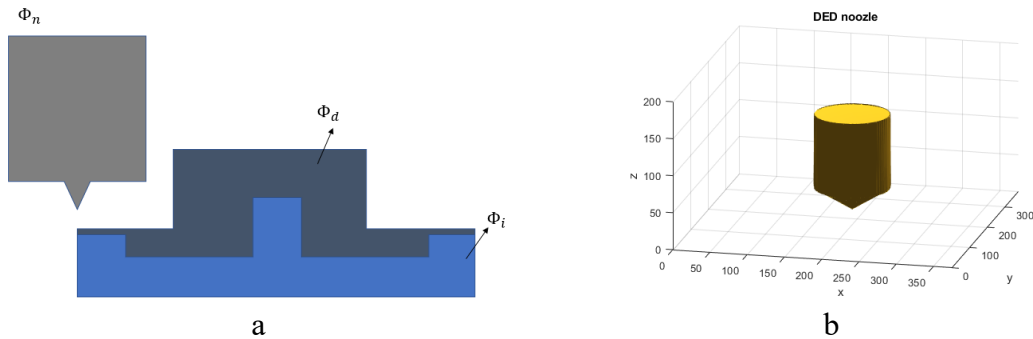


Figure 6.12. Representations in the DED nozzle collision problem: (a) The level-set representations for DED nozzle, deposition material and intersection part; (b) 3D voxel representation for DED nozzle

As far as the collision detection is concerned, the collision-free rigid motion of the DED nozzle in rigid motion needs to be calculated. In this study, dilation as a morphology operation is adopted to analyze the spatial planning of the DED nozzle. As one of the basic operations in mathematical morphology, dilation operation $\oplus$ is defined as:

116

$$A \oplus B = \bigcup_{b \in B} A_b \tag{6-15}$$

where $A_b$ represents the solid $A$ transformed by a rigid transformation $b$, $B$ is a structuring element, which is termed filters. For level set function represented models, the dilation operation is expressed as:

$$\Phi_A \oplus \Phi_B = \bigcup_{\Phi_B(b) \geq 0} \Phi_A(b) \tag{6-16}$$

For the DED process, the materials are deposited on the deposition volume layer by layer, which indicates that the tip of the deposition nozzle requires going through each point of the deposition volume (Figure 6.13a). It is crucial to mention that in a practical case, the vertical distance between the tip of the DED nozzle and the deposition area is not zero. The vertical distance is assumed to be zero for the sake of simplifying in explaining the proposed method. The technical implantation of the approach will be discussed with considering the vertical distance later in this section. It is meaningful to explore all motions of the DED nozzle to deposit the materials in the deposition volume. In the proposed method, the motions of the DED nozzle during deposition is calculated by dilating the deposition volume by the DED nozzle: $\Phi_m = \Phi_n \oplus \Phi_d$, and the this study define $\Phi_m$ as *motion space* of the DED nozzle, as presented in Figure 6.13b.



Motion of the DED nozzle

Deposition volume

$\Phi_n \oplus \Phi_d$

a                                                b
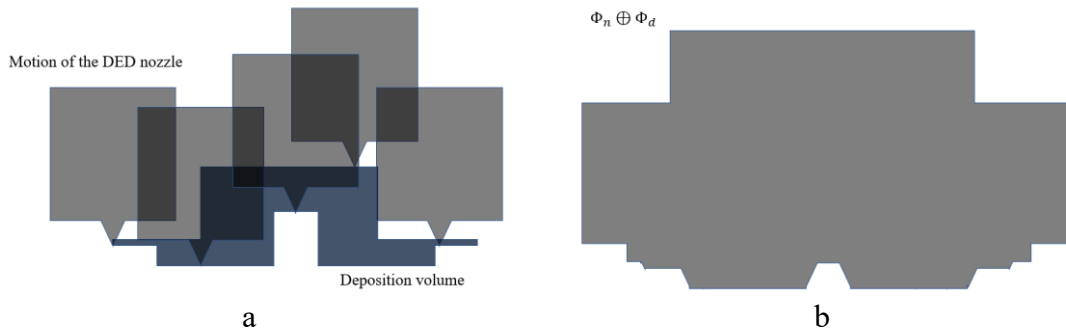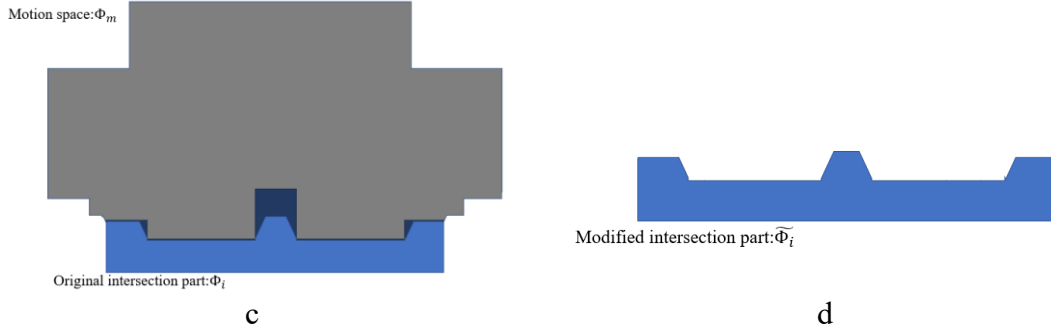
Figure 6.13. (a) Motions of the DED nozzle during deposition; (b) motion space of the DED nozzle; (c) motions space and original intersection part; (d) modified intersection part.

**Theorem:**

The modified intersection part $\widetilde{\Phi}_i$ can be derived from: $\widetilde{\Phi}_i = \Phi_i \setminus \Phi_m = \Phi_i \setminus (\Phi_n \oplus \Phi_d)$, which leads no collision with the DED nozzle in operation, as shown in Figure 6.13d.

**Proof:**

In the condition of no collision occurring during deposition, $\widetilde{\Phi}_i \cap \widetilde{\Phi}_m = \emptyset$ is required to be satisfied, where $\widetilde{\Phi}_m$ is the new motion space derived from the modified intersection part $\widetilde{\Phi}_m = \Phi_n \oplus \widetilde{\Phi}_d$. $\widetilde{\Phi}_m$ can be expanded into:

$$\begin{aligned} \widetilde{\Phi}_m &= \Phi_n \oplus \left(\Phi_f \setminus \widetilde{\Phi}_i\right) = \Phi_n \oplus \left(\Phi_f \cap \left(-\widetilde{\Phi}_i\right)\right) \\ &= \Phi_n \oplus \left(\Phi_f \cap \left(-(\Phi_i \cap (-\Phi_m))\right)\right) \end{aligned} \tag{6-17}$$

where $\Phi_f$ indicates the level set function of the final part. According to the associativity, commutativity of Boolean operation and distribution of dilation, Eq. (6-17) can be rearranged as:

$$\widetilde{\Phi}_m = (\Phi_n \oplus \Phi_d) \cap (\Phi_n \oplus \Phi_m) \tag{6-18}$$

Therefore, no collusion condition is derived as:

118

$$\widetilde{\Phi}_i \cap \widetilde{\Phi}_m = \Phi_i \cap (-\Phi_m) \cap (\Phi_n \oplus \Phi_d) \cap (\Phi_n \oplus \Phi_m) \tag{6-19}$$

Since $\Phi_n \oplus \Phi_d = \Phi_m$, $(-\Phi_m) \cap (\Phi_n \oplus \Phi_d) = \emptyset$. So, $\widetilde{\Phi}_i \cap \widetilde{\Phi}_m = \Phi_i \cap \emptyset \cap (\Phi_n \oplus \Phi_m)$. Due to the annihilator law for $\cap$, $\widetilde{\Phi}_i \cap \widetilde{\Phi}_m = \emptyset$.

The study develops an algorithm to implement the proposed method for discrete level set function representations, also considering the vertical distance ($d$) between the nozzle tip and deposition area. The pseudocode for the proposed algorithm is presented in Table 6.2. An example of the implantation of the proposed method is shown in Figure 6.14. Figure 6.14a presents the original intersection part and Figure 6.14b shows deposition volume derived from the original intersection part by $\Phi_f \backslash \Phi_i$. The motion space calculated from Equation (6-16) is shown in Figure 6.14c and Figure 6.14d gives the modified intersection part $\widetilde{\Phi}_i$.

Table 6.2: Pseudocode of the algorithm.

---

**Input:** discrete level set function $\Phi_n$, $\Phi_d$ and $\Phi_i$; vertical distance $d$

$\Phi_m \leftarrow 0$ with size of $\Phi_d$

[x, y, z] = index of $\Phi_d > 0$ in x,y,z directions

The position of the tip is obtained from $\Phi_n$ as x_tip, y_tip, z_tip

For i = 1 to size of x direction:

    Move on x direction $M_x$ = x (i) - x_tip

    Move on y direction $M_y$ = y (i) - y_tip

    Move on z direction $M_z$ = z (i) - z_tip + $d$

    New position of DED nozzle $\Phi_{\tilde{n}}$ = translating the $\Phi_d$ over $M_x$, $M_y$, $M_z$

---

$$\Phi_m = \Phi_m \cup \Phi_{\tilde{n}} = \max(\Phi_m, \Phi_{\tilde{n}})$$

End

**Output:** discrete level set function of modified intersection part $\widetilde{\Phi}_i = \Phi_i \backslash \Phi_m = \min(\Phi_i, -\Phi_m)$
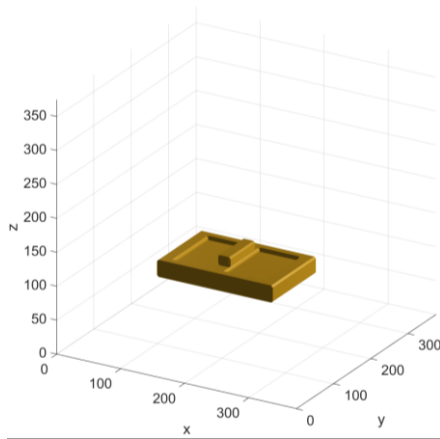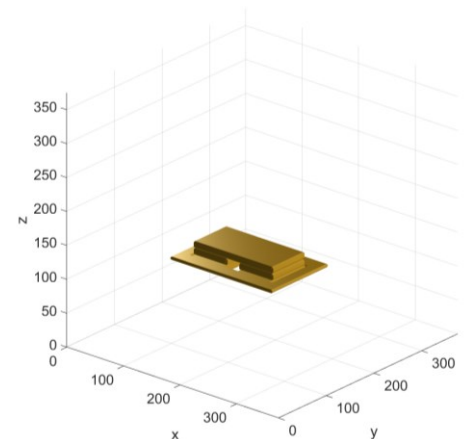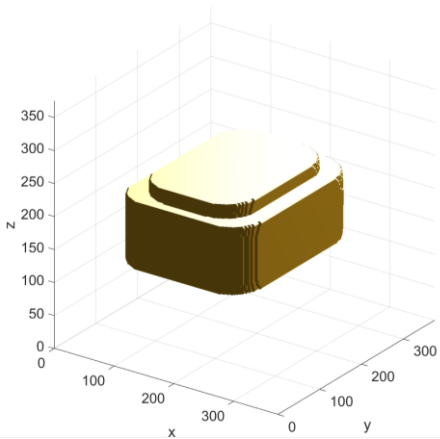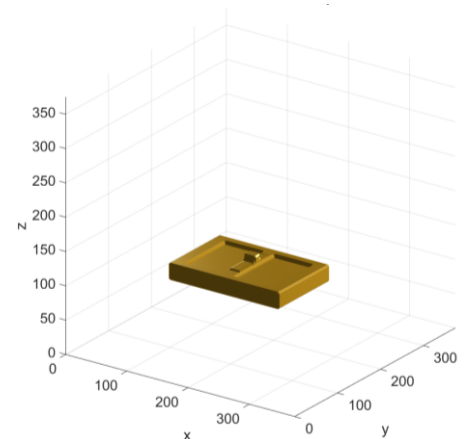


Figure 6.14. An example for the intersection part modification method: (a) original intersection part; (b) deposition volume; (c) motion space; (d) modified intersection part.

## 6.2.6 Individual Feature Extraction

As the modified intersection part has been calculated, a subtractive feature volume (SFV) and an additive feature volume (AFV) can be calculated in their level set function representations as:

$$\Phi_{SFV} = \Phi_u \setminus \widetilde{\Phi}_i$$
$$\Phi_{AFV} = \Phi_f \setminus \widetilde{\Phi}_i$$

(6-20)

Individual features are required to be recognized and extracted from SMV and AMV. The research of CSG-based feature recognition has been developed from the 1990s, but this technique did not go far primarily due to the non-uniqueness of CSG trees [136]. Recently, there are some research efforts have been devoted to address non-uniqueness problems in CSG and show the strength in recognize sophisticated machining features by 3D convolution neuron network [155,156]. Therefore, developing a new machining feature recognition method is not a contribution to this study. The level set function representation of SFV is converted into 3D voxel grid information $V_{SFG}$ by Heaviside function $H()$, and then SFs can be extracted by any CSG-based feature recognition techniques; see Equation (6-21).

$$V_{SFV} = H(\Phi_{SFV}) \rightarrow \{SF_1, SF_2, SF_3, \dots SF_n\}$$

(6-21)

AFV comprises both AFs and SFs. In the AM process, leaving a sufficient over-thickness to have a finishing operation is vital for meeting the tolerance and surface roughness requirements. The over-thickness value is estimated by the required specifications of the final feature, the surface roughness generated by the AM processes and the machining conditions. With considering over-thickness, the modified additive feature volume ($\overline{AFV}$) is modified. The level set function representation of $\overline{AFV}$ can be derived via Equation (6-22), where t represents the over-thickness value. The residual

121

subtractive feature volume ($\overline{\text{SFV}}$) is obtained via Equation (6-23). Similarly, the individual SFs could be recognized by a CSG-based feature recognition method by Equation (6-24).

$$\Phi_{\overline{\text{AFV}}} = (\Phi_{\text{AFV}} + t) \setminus \widetilde{\Phi}_i \qquad (6\text{-}22)$$

$$\Phi_{\overline{\text{SFV}}} = \Phi_{\overline{\text{AFV}}} \setminus \Phi_{\text{AFV}} \qquad (6\text{-}23)$$

$$H(\Phi_{\overline{\text{SFV}}}) \rightarrow \{SF_{n+1}, SF_{n+2}, SF_{n+3}, \ldots SF_{n+m}\} \qquad (6\text{-}24)$$

## 6.3 Cost-driven Process Planning for Remanufacturing

The number of AFs and SFs are obtained from the proposed feature extraction method. Each feature represents an operation in the AM or SM process. Under considering the topological relationship of different features, the sequences of some operations are forced. Therefore, precedence constraints between operations are required to formulated to respect the hybrid additive-subtractive manufacturing rules. The precedence constraints are comprehensively summarized in Section 5.2.2.

Although precedence constraints are formulated, some residual process sequences are still undermined. To develop the process planning problem into a process sequence optimization, the cost for each operation/feature is required to be estimated. With precedence constraints between features and cost model for each feature, an integer programming model is formulated to calculate the optimal process plan that minimizes the overall remanufacturing cost.

### 6.3.1 Cost Estimation for Hybrid CNC-DED process

The motivation of the cost estimation for this study is approximating the cost models for the integer programming model to determine the optimal process plan, rather than exploring the precise cost for each operation. Although there are numbers of publications are relevant to cost estimation for the SM and AM process [157–159], few researchers focus on the constructing cost model for integrated hybrid CNC-DED manufacturing

system, explicitly considering the change cost between two different operations. Therefore, in this section, rough and fast estimations are given for SFs and AFs, and the change costs between various features are also introduced.

### 6.3.1.1 Cost of subtractive feature

The total cost comprises operation cost and tool cost as:

$$C_{SF} = C_{hh} * t_{SF} + C_{tool} * n_{tool} \tag{6-25}$$

where $C_{SF}$ is the total cost of an SF, $C_{hh}$ is the hourly operation cost for HM machine operation, $t_{SF}$ is the machining time for the SF, $C_{tool}$ is the cost of each cutting tool, and $n_{tool}$ is the number of tool changes. Most commercial CAM software systems can estimate the machining time $t_{SF}$ by dividing the tool path in the milling process by the programmed feed rate.

### 6.3.1.2 Cost of additive feature

The cost of AF is determined by the machine cost and material consumption cost, see Eq.(6-26).

$$C_{AF} = C_{hh} * t_{AF} + C_{m-AF} \tag{6-26}$$

where $C_{AF}$ is the total cost of an AF, $C_{hh}$ is the hourly operation cost for HM machine operation, $t_{AF}$ is the building time of the AF, and $C_{m-AF}$ is the cost of material consumption.

The cost of material consumption in DED process is approximately calculated from the volume of the feature and its support structure, as:

$$C_{m-AF} = \frac{(V_{AF}\rho + V_{AF-s}\overline{\rho})}{\mu} C_{material}^{unit} \tag{6-27}$$

where, $V_{AF}$ and $V_{AF-s}$ refer to the volume of the building part and support structure, $\rho$ is the material density, $\overline{\rho}$ is the material density of the support structure, and $C_{material}^{unit}$

indicates the price per unit of material. In the DED process, complex gas flow leads a diffusion of powder distribution, which results in low powder efficiency because some powder cannot reach the meltpool. Powder efficiency rate $\mu$ varies between different machines, and in this research the value is 70%.

For the DED process, the building time $t_{AF}$ estimation adopted an analytical build time model which is proposed in [160], and the general equation is shown in Eq.(6-28). This model uses G-code of the part as input and an algorithm extracts the kinematic characteristics of the nozzle to estimate very accurate build time results since the acceleration and deceleration of the machine head are considered.

$$t_{AF} = \text{Deposition Time} + \text{Rapid Movements Time} \qquad (6\text{-}28)$$

### 6.3.1.3 Cost of Change

For the hybrid additive-subtractive system, the AM/SM operations are switching by changing different tools. It is crucial to discuss the cost of change between two consecutive operations since it is costly due to frequent tool changing. Besides the tool change cost, the re-orientation of the workpiece also results in costs. In this study, CR and CT represent indexes of the re-orientation cost, and the tool change cost, respectively. The details of the calculation are given below.

*Re-orientation cost:*

While the orientation of the workpiece is switched in the HM machine, a re-orientation change occurs that requires workpiece fixing and laser calibration.

$$CR = C_{hh} * t_{re} \qquad (6\text{-}29)$$

For the index of feature $i, j \in F = \{1, 2, \ldots, F\}$, the index of cost for orientation CR is formed by grouping the cost of orientation between any two features.

*Tool change cost:*

For HM machine the tool change cost is formulated as:

$$CT = C_{hh} * t_{tc} \hspace{3cm} (6\text{-}30)$$

Similarly, the index of tool change cost $CT$ is constructed by grouping the cost of tool change cost between any two features.

## 6.3.2 Sequence Optimization

As the cost model for each feature, change cost, and precedence constraints are obtained. The process sequence optimization problem is formulated as an integer programming model and solved by branch and fathoming algorithm [94]. In a directed graph visualization of the model, a node represents a feature/operation and the cost model, and the directed line indicates the precedence relation between two features/operations and the change costs. As an example, AFs (AF1 and AF2) and SFs (SF1, SF2, SF3) are extracted from the proposed feature recognition method. The cost for each node is calculated and the change cost between any two nodes is formulated. The precedence constraints are applied to these nodes initially as dash lines (Figure 6.15a). With the optimization of the - integer programming model, the output is a sequence of operations that results in a minimal cost (Figure 6.15b).
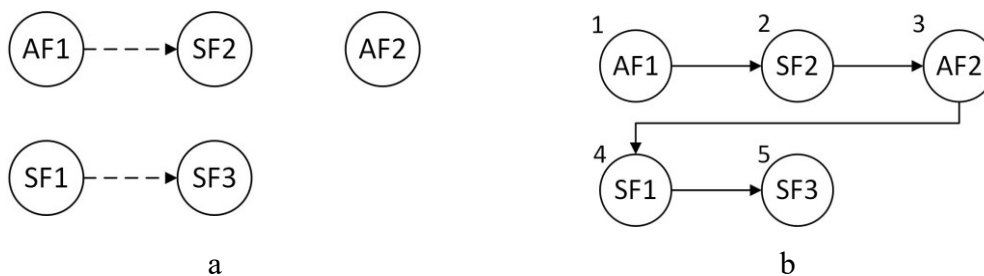


Figure 6.15: Directed graphs representation: (a) precedence-constrained model; (b) optimal model.

The mathematical formulation of the integer programming model is employed from Section 5.2.4 [161]. With this mathematical formulation, the model can be solved through branch and bound, linear programming, dynamic programming as exact approaches or genetic algorithm as an approximate approach.

## 6.4 Case Study I: test part remanufacturing

In this section, the proposed method is verified by the correctness and efficiency of a virtual case study.

Figure 6.16a shows the point cloud scanned from the used part, which is required to be remanufactured. Figure 6.16b represents the CAD model of the final part, which has different functionalities compared to the used part. Especially, the final part has primitive features and 2.5D freeform feature.



a                                             b
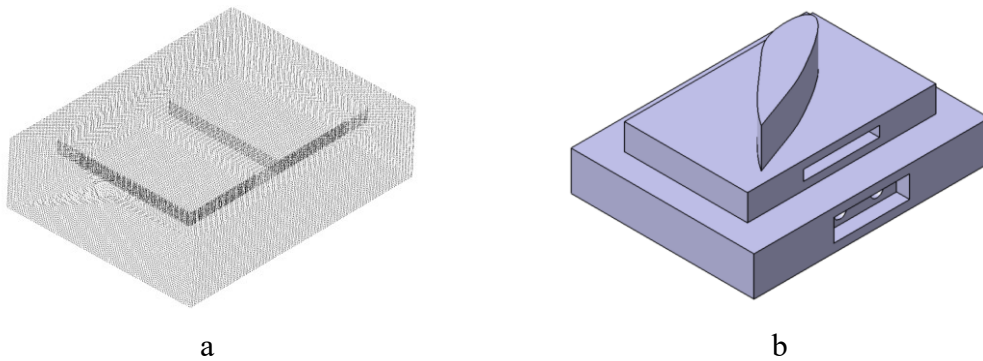
Figure 6.16: Case study 1: (a) point cloud of the used part (b) CAD model final part.

The level set function for the final part is built from the CAD modelling on a design domain of size 150*150*150 with grid size $\Delta x$ (0.5mm), as Figure 6.17 shown. The modelling history is given in Table 6.3, and the mathematical formulation of each level set function is provided in Appendix.
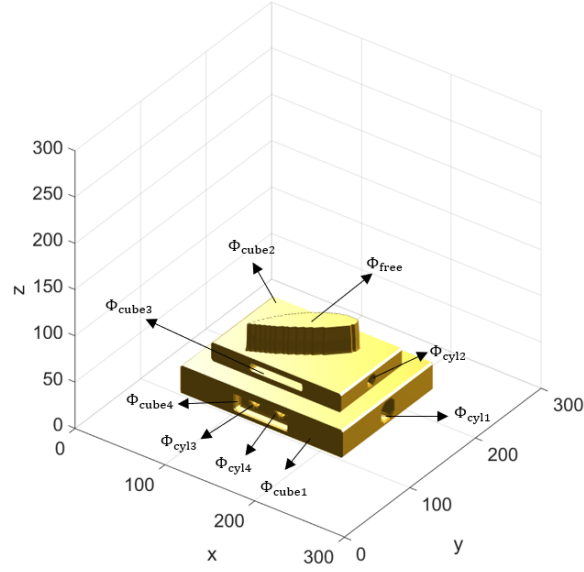
Figure 6.17: Level set representation for the final part.

Table 6.3: Case study 1: Modelling history of the level set representation for the final part.

| Modelling history: |
|---|
| $\Phi_{f_1} = \max\left(\Phi_{\text{cube1}}, \Phi_{\text{cube2}}, \Phi_{\text{free}}\right)$ |
| $\Phi_{f_2} = \min\left(\Phi_{f_1}, -\Phi_{\text{cyl1}}, -\Phi_{\text{cyl2}}, -\Phi_{\text{cyl3}}\right)$ |
| $\Phi_f = \min\left(\Phi_{f_2}, -\Phi_{\text{cube3}}, -\Phi_{\text{cube4}}\right)$ |
| Notations: |
| $\Phi_{\text{cube}}$: level set function for cube; |
| $\Phi_{\text{cyl}}$: level set function for cylinder; |
| $\Phi_{\text{cyl}}$: level set function for cylinder; |
| $\Phi_{\text{free}}$: level set function for freeform feature; |
| $\Phi_f$: level set function for final part. |

In terms of the used part, the RANSAC surface fitting technique is adapted and the max distance and angular distance variants are set as 0.002 m and 5 degrees, respectively. The surface fitting results are shown in Figure 6.18a. By implementing the k-NNG-based defect identification method, the defect points are differentiated from the point clouds

127

Figure 6.18b. The level set function for the used part is constructed in Figure 6.19a with modelling history: $\Phi_u = \min{(\Phi_{cube1}, -\Phi_{cube2}, -\Phi_{cube3}, -\Phi_{cube4})}$ and formulations for each level set functions are given in Appendix. The optimal pre-machining feature can be obtained from the defect points, and the used part is updated with the pre-machining feature, as shown in Figure 6.19b.

The proposed intersection part extraction algorithm is applied to find the relative position between the used part and the final part. The optimization results of the translation and rotation variables are listed in Table 6.4 and the output of the intersection part is shown in Figure 6.20.

For the next step, the intersection part is modified by considering the collision problem in the DED process. The DED nozzle is modelled in level set function as shown in Figure 6.21a and the vertical distance d is set as 10 mm. Figure 6.21b shows the deposition volume, which is obtained by subtracting the final part by the original intersection part. The motion space that represents all possible motions of the DED nozzle during deposition is derived from the proposed algorithm (Table 6.2); see Figure 6.21c. The result of the modified intersection part through subtracting the original intersection part by motion space is presented in Figure 6.21d.



|  a  |  b  |
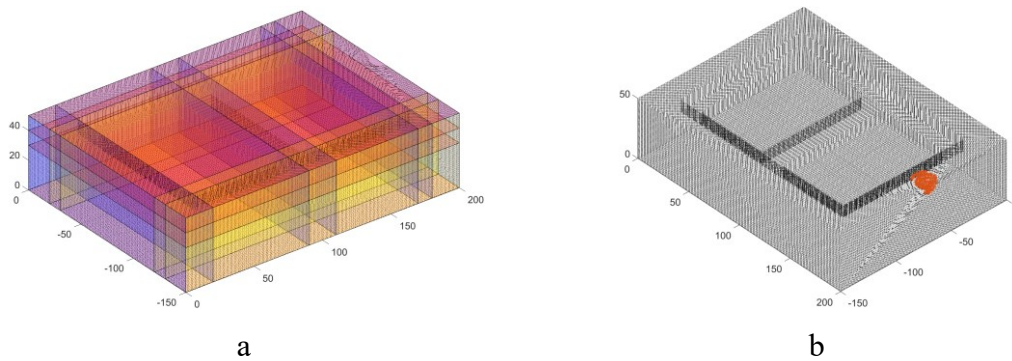
Figure 6.18: Case study 1: (a) Surface fitting results; (b) defect area (red points) from point clouds of the used part;
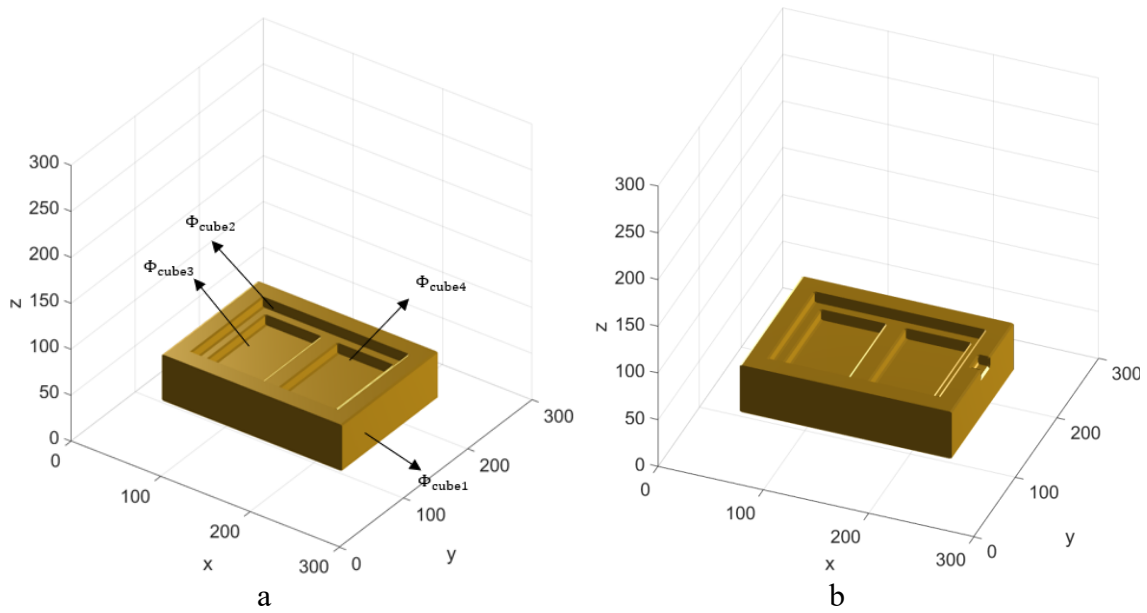
Figure 6.19: Case study 1: (a) Level set representation for the used part; (b) updated used part with pre-machining feature.

Table 6.4: Case study 1: The optimal translation and rotation for test parts.

| | Translation (mm) | | | Rotation (°) | | |
|---|---|---|---|---|---|---|
| | $t_x$ | $t_y$ | $t_z$ | $\theta_x$ | $\theta_y$ | $\theta_z$ |
| Optimal variables: | 4.07 | 4.21 | -1.33 | 0 | 0 | 0 |

a                                           b
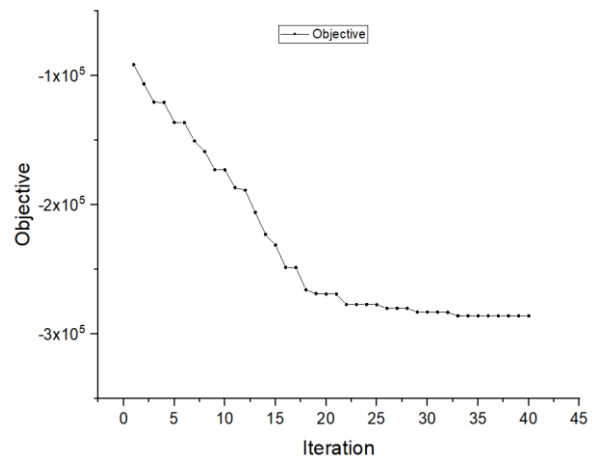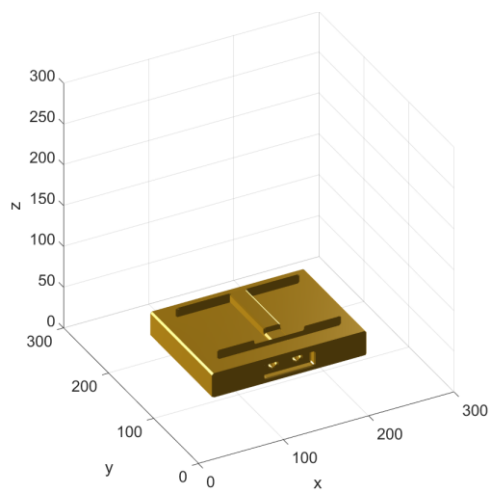
Figure 6.20: Case study 1: (a) Optimal intersection part; (b) convergence history of the intersection part maximization.



a                                           b



c                                           d
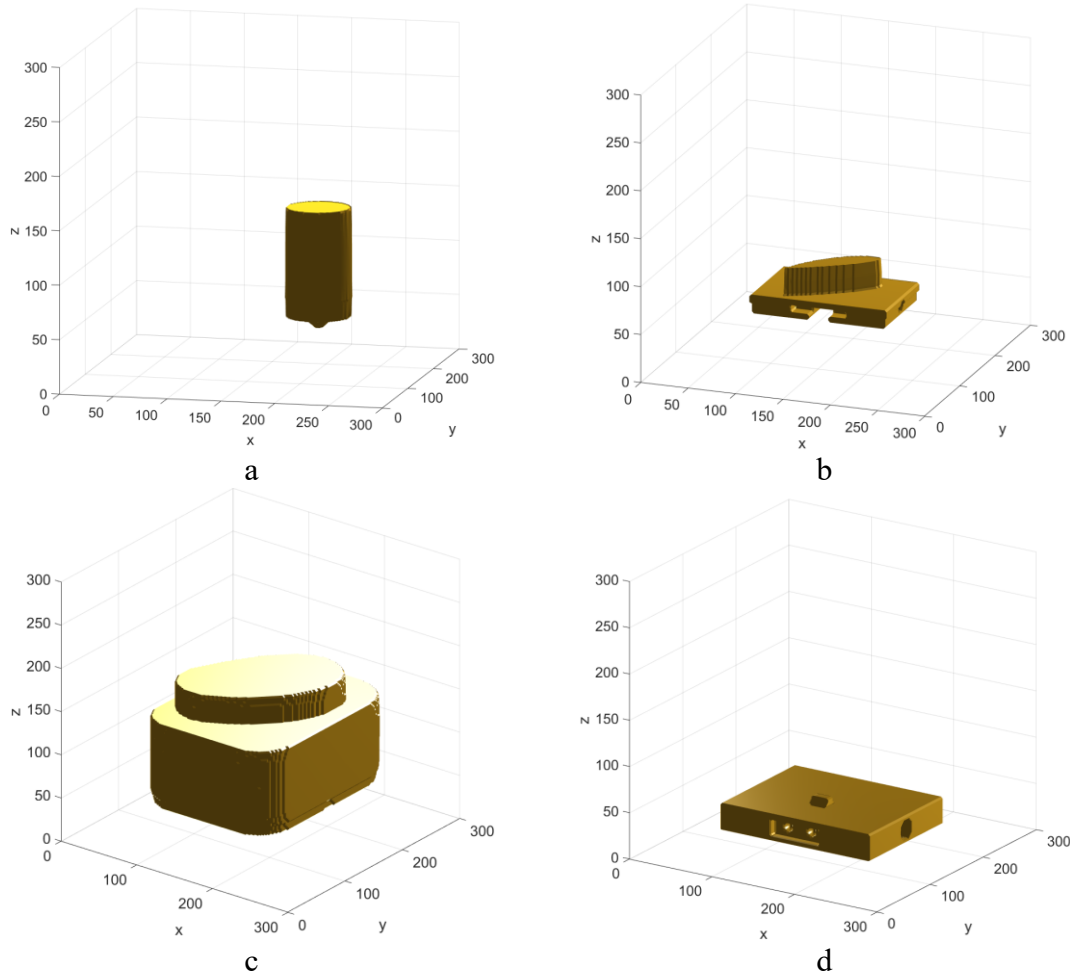
Figure 6.21: Case study 1: (a) DED nozzle; (b) deposition volume; (c) motion space of DED nozzle; (d) modified intersection part.

By subtracting the final part and the used part by the modified intersection part, SFV and AFV can be collected, respectively. Then, each SF and AF are extracted, as presented in Figure 6.22. With respecting HM rules, precedence constraints are applied to all features.

The parameters and machine resources that are used in the cost estimation are listed in Table 6.5. In this study, Ti-6Al-4V is used as the material for the DED process. The sequence optimization problem is solved by a branch-and-bound solver and the optimized

process plans are presented in Table 6.6, and the optimal remanufacturing plan costs $ 1835.24.
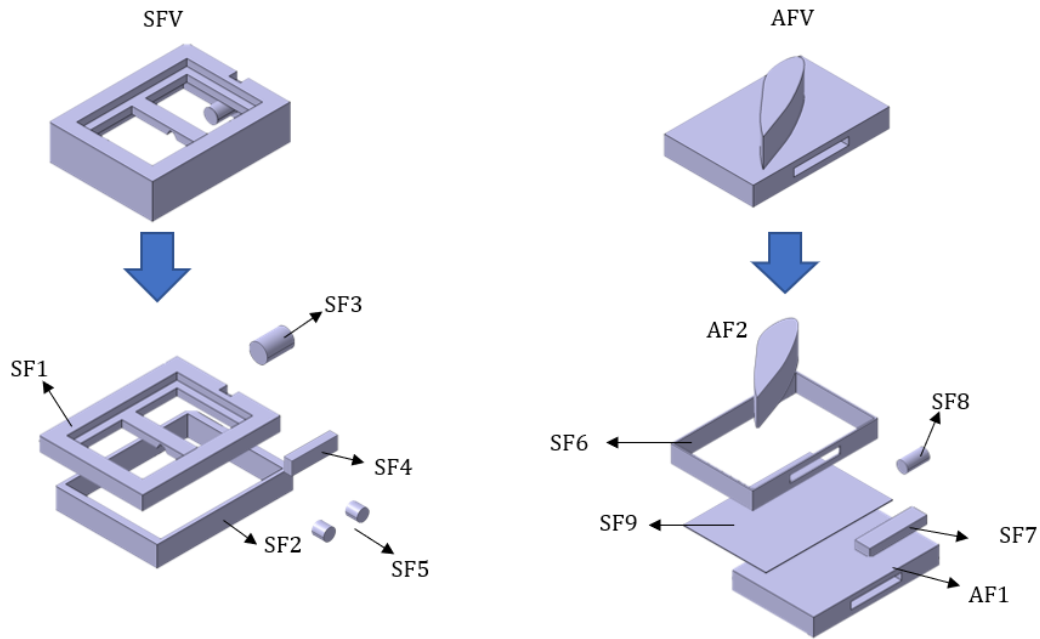


Figure 6.22: The results of SFs and AFs extraction from SFV and AFV.

Table 6.5: Manufacturing parameters and manufacturing resources for cost estimation.

| Manufacturing parameters | | Manufacturing resources | | |
|---|---|---|---|---|
| Parameter | Value | Tool ID | Tool type | Diameter (mm) |
| $C_{hh}$ | 100 $/h | T1 | End mill | 20 |
| $C_{tool}$ | 5 $ | T2 | End mill | 10 |
| $\rho$ | 4.43 $kg$/dm$^3$ | T3 | End mill | 5 |
| $\bar{\rho}/\rho$ | 0.4 | T4 | Drill | 5 |
| $C_{material}^{unit}$ | 450 $/kg | T5 | Drill | 10 |
| $t_{re}$ | 0.35 h | T6 | DED | - |
| $t_{tc}$ | 0.17 h | | | |

Table 6.6: Case study 1: Optimal process plan.

| Sequence | Features | TAD | Tool |
|---|---|---|---|
| 1 | SF1 | +z | T1 |
| 2 | SF2 | +z | T1 |
| 3 | AF1 | +z | T6 |
| 4 | SF9 | +z | T2 |
| 5 | AF2 | +z | T6 |
| 6 | SF5 | +y | T4 |
| 7 | SF8 | +x | T4 |
| 8 | SF3 | +x | T4 |
| 9 | SF6 | +y | T2 |
| 10 | SF7 | +y | T3 |
| 11 | SF4 | +y | T3 |

## 6.5 Case Study II: bracket remanufacturing

In the second case study, the proposed method is validated by the remanufacturing process of a used pillow bracket (see Figure 6.23a) to a new featured bracket (see Figure 6.23b). The CSG models for the used part and final part are constructed by discrete level set function on a design domain of size 150*150*150 with grid size $\Delta x$ (0.5mm), as shown in as follows:
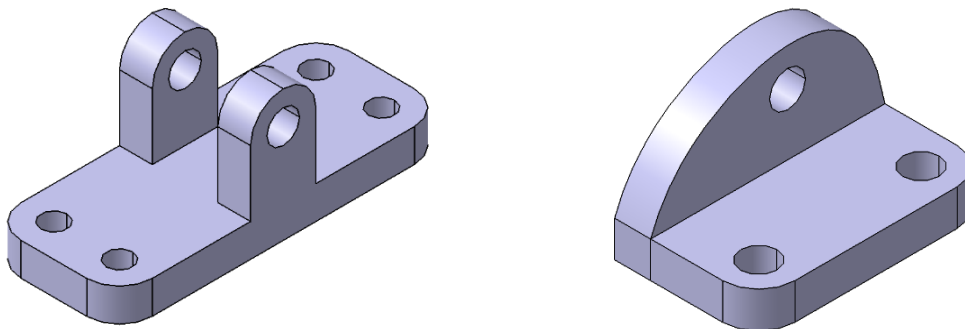
Figure 6.23: Case study 2: (a) the used pillow bracket (b) the final part.



a                                           b
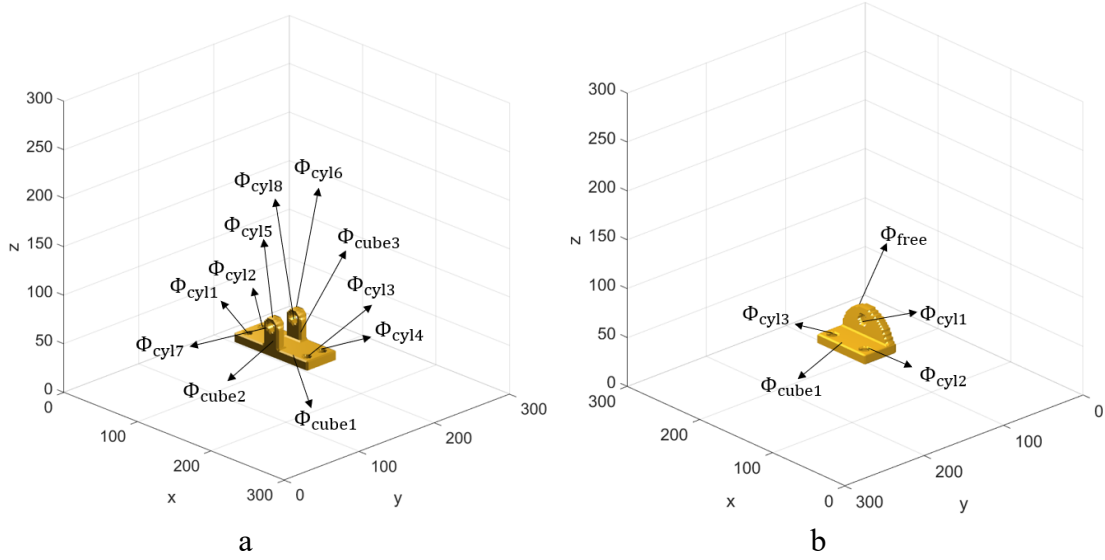
Figure 6.24: Discrete level-set representation: (a) the used pillow bracket (b) the final part.

Table 6.7: Case study 2: Modelling history of the level set representations.

| Modelling history for the used part: |
| --- |
| $\Phi_{f_1} = \max\left(\Phi_{cube1}, \Phi_{cube2}, \Phi_{cube3}, \Phi_{cyl5}, \Phi_{cyl6}\right)$ |
| $\Phi_f = \min\left(\Phi_{f_1}, -\Phi_{cyl1}, -\Phi_{cyl2}, -\Phi_{cyl3}, -\Phi_{cyl4}, -\Phi_{cyl7}, -\Phi_{cyl8}\right)$ |
| Modelling history for the final part: |
| $\Phi_{f_1} = \max\left(\Phi_{cube1}, \Phi_{free}\right)$ |
| $\Phi_{f_2} = \min\left(\Phi_{f_1}, -\Phi_{cyl1}, -\Phi_{cyl2}, -\Phi_{cyl3}\right)$ |

The intersection part extraction algorithm is implemented for the used part and final part to obtain the maximized intersection volume, and the optimal translation and rotation values are shown in Table 6.8. The intersection part is presented in Figure 6.2a and the convergence history is shown in Figure 6.2b. It can be observed that, the optimization problem is converging quickly, and the optimal values are achieved around 10 iterations.

133

Table 6.8: Case study 2: The optimal translation and rotation for test parts.

| | Translation (mm) | | | Rotation (°) | | |
|---|---|---|---|---|---|---|
| | $t_x$ | $t_y$ | $t_z$ | $\theta_x$ | $\theta_y$ | $\theta_z$ |
| Optimal variables: | -2.2 | 1.2 | 2.34 | 0 | 0 | 0 |
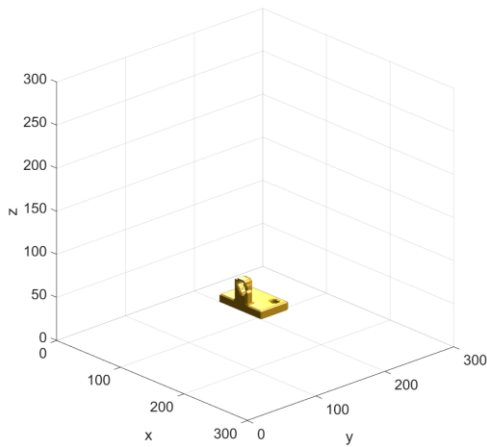
a
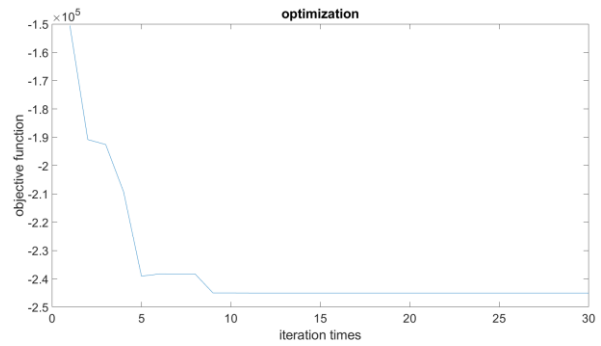
b

Figure 6.25: Case study 2: (a) Optimal intersection part; (b) convergence history of the intersection part maximization.

The nozzle is constructed by level set function in Figure 6.26a; the intersection volume for the AM process is represented in Figure 6.26b; the motion space for nozzle deposition is modelled in Figure 6.26c; by implementing the modification algorithm, the result of the modified intersection part is obtained in Figure 6.26d.
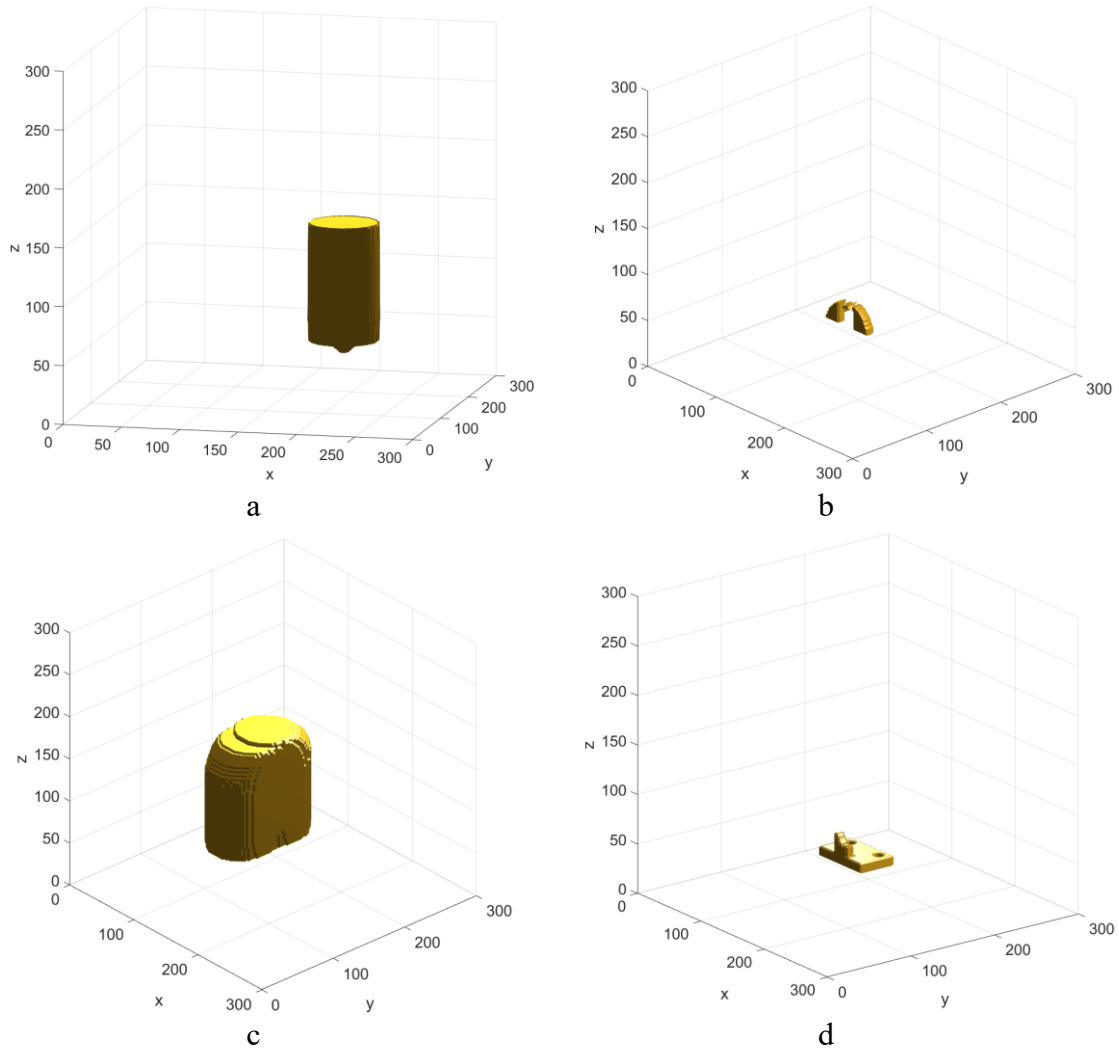
Figure 6.26: Case study 2: (a) DED nozzle; (b) deposition volume; (c) motion space of DED nozzle; (d) modified intersection part.

By subtracting the final part and the used part by the modified intersection part, SFV and AFV are collected, respectively. Then, each SF and AF are extracted. With the cost model for each feature and precedence constraint information, the programming model is formulated and solved by LINGO. The optimized process plans are presented in Table 6.9.

Table 6.9: Case study 2: Optimal process plan.

| Sequence | Features | TAD | Tool |
|---|---|---|---|
| 1 | SF3 | +z | T4 |
| 2 | SF4 | +z | T4 |
| 3 | SF1 | +z | T2 |
| 4 | SF2 | +z | T2 |
| 5 | SF5 | +z | T2 |
| 6 | SF6 | +z | T2 |
| 7 | AF1 | +z | T6 |
| 8 | AF2 | +z | T6 |

## 6.6 Conclusion

Nowadays, the combination of AM and SM in a single workstation is emerging to provide a more flexible and productive and capable manufacturing approach comparing with traditional manufacturing strategies. Because it utilizes the merits of AM and SM to add and remove features flexibly, HM has the potentials to raise remanufacturing technology to a higher level. In this chapter, taking to account the benefits of the HM process, hybrid CNC-DED manufacturing technology in a single workstation is investigated to remanufacture an end of life part (used part) to a new part (final part) with new functionalities, avoiding the material recycling process.

This chapter has demonstrated a novel feature extraction algorithm and a cost-driven process planning method for hybrid CNC-DED manufacturing in a remanufacturing context. Specifically, starting from point clouds for the used part and a solid CAD model for the final part, geometry modeling is performed to transform the input to level set representations. Also, the defects on the used part are investigated and an optimal pre-machining feature is derived from the proposed method and applied to remove the perturbation caused by the defects. The feature extraction method, developed under the level set framework, is proposed as an automated process to extract the AM and SM features for remanufacturing process planning, which addresses the numerical calculation between two solid models. Moreover, the collision problems of DED nozzle during

deposition are considered and this method provides collision-free motions. With the carefully developed hybrid CNC-DED cost model, the process planning work is converted to an integer programming model as an optimization problem. Finally, the optimal process plan can be determined by solving the optimization problem.

For future work, there are more research works need to be done to expand the current methodology. A practical case study is required to validate the work presented in this study. Moreover, in the present study, the AM and SM processes are considered as a 3-axis type. However, the feature extraction and process planning problems for multi-axis capability need to be addressed.

# Chapter 7: Conclusion, Discussion & Future work

## 7.1 Conclusions

The increasing developments and over-exploitation of resources outcome vast amount "end-of-life" products. Remanufacturing and repairing are identified as environmentally friendly approaches to deal with them since the energy consumption to produce a new part can be minimized by maintaining the intrinsic energy of the legacy part. The research presented aims to automate and optimize the remanufacturing and repairing processes and, the current remanufacturing and repairing processes can be improved in perspectives of damage inspection, nominal volume reconstruction, process planning. The developed framework enables (a) an intelligent inspection to support automated classification and localization of damages from the end-of-life part; (b) an efficient geometric reconstruction of the damaged part to support the damaged volume extraction; (c) cost-driven and collision-free process planning that support HM processes.

In the module of intelligent damage inspection, firstly, the RGB image and depth image are acquired by a depth camera. Then, the Mask RCNN-based model train the collected data and results in the damage segments with the recognized damage type. With that result, the spatial position of the damaged area is calculated by the integration of damage segments and a point cloud from the depth data. The results of the damage type and damage location are beneficial to damage the volume extraction module for the repairing process and also process planning module for the remanufacturing process. In the damage volume extraction module, an efficient and precise nominal model reconstruction method is developed, which includes the processes of StepRANSAC surface fitting, SDM refitting, modelling, damage volume localization, and extraction. The result of reconstruction significantly facilitates the repairing process because it does not require prior information on the nominal CAD model. In the process planning for hybrid remanufacturing, two scenarios of CNC-PBF and CNC-DED are explored separately due to their different

working principles. In both scenarios, the level of automation of hybrid processes is strongly raised by collision-free and cost-minimized process plans.

## 7.2 Research Contributions

The main contributions of this research are summarized as follows:

- Developed a deep learning-based damage inspection method which performs damage classification and 3D localization simultaneously. The method can achieve an acceptable accuracy (average relative error from 4.322% to 11.253%) to localize the damage area in 3D frame with a small training data size and a low cost RGB-D camera.

- Developed a primitive-based nominal reconstruction method for the general mechanical component which is less concentrated in previous studies. With the reconstruction results, the repairing does not require a priori information of the nominal CAD model.

- Developed a novel primitive surface fitting method, by the combination of StepRANSAC and SDM. It has been proven a 60–90% improvement in precision compared with the traditional RANSAC method.

- Proposed a primitive and free-form feature modelling method under an implicit level set representation for the automation of feature extraction for HM remanufacturing.

- Summarized precedence constraints for hybrid remanufacturing.

- Formulated the process planning for remanufacturing into an integer programming model which can be numerically optimized in an objective of cost-minimization.

- Developed cost-driven process planning methods for hybrid CNC-PBF and CNC-DED separately in remanufacturing context.

- Proposed a concept of pre-machining feature for removing defect area from the end-of-life part, which is an issue rarely addressed in the previous studies of process planning for remanufacturing.

- Developed the cost estimation for HM and proposed a concept of change cost which can explicitly explore the cost of switching operations in a hybrid process.

## 7.3 Limitations and future work

Despite the achievement of its goal, the research presented is confronted by particular limitations and can be addressed in future work:

- The current remanufacturing/repair industry relies on visual inspection to determine the damage type, damage location and damage degree to schedule the process plans. The proposed damage classification and localization method currently is able to perform damage detection to output the damage type, and location. However, the damage degree determination is also significantly important to schedule process plans for remanufacturing/repairing, which is not covered in this thesis. In future work, the proposed method can be extended for damage degree characterization by constructing quantified scores for the damaged part. Different damage features (e.g. wear, crack and corrosion) with their corresponding quantification model can be established, as examples of wear damage model, crack damage model and corrosion model.

- The primitive surface-based nominal model reconstruction method is currently only focusing on primitives (e.g. plane, cylinder, cone and sphere). Given the fact that freeform surfaces are playing an increasingly important role in mechanical design, this aspect can be highly focused on future work.

- The framework of process planning for hybrid remanufacturing has been proven its efficiency in several virtual case studies. However, it also needs to be validated in some practical case studies, because the manufacturing constraints may vary from specific AM and SM machines. Therefore, some more specific manufacturing constraints should be considered in real case studies, which can be addressed in future work. The promising application can be remanufacturing of high-value components such as molds and dies, components of aircraft.

- Additive-subtractive process with multi-axis capability need to be considered for complex freeform surface. In the future work, the motion space analysis proposed in this thesis can be extended to explore the motions of nozzle of DED and cutting tool

140

in CNC machining under a five-axis environment. In addition, issues of fixture and AM support structure are also necessary to be addressed in the future.

# Bibliography

[1]     Kristyn S-K. Global Waste to Grow by 70 Percent by 2050 Unless Urgent Action is Taken: World Bank Report 2018. https://www.worldbank.org/en/news/press-release/2018/09/20/global-waste-to-grow-by-70-percent-by-2050-unless-urgent-action-is-taken-world-bank-report.

[2]     Wang H, Jiang Z, Zhang X, Wang Y, Wang Y. A fault feature characterization based method for remanufacturing process planning optimization. J Clean Prod 2017;161:708–19. https://doi.org/10.1016/j.jclepro.2017.05.178.

[3]     King AM, Burgess SC, Ijomah W, McMahon CA. Reducing waste: Repair, recondition, remanufacture or recycle? Sustain Dev 2006;14:257–67. https://doi.org/10.1002/sd.271.

[4]     Zhang JH, Yang B, Chen M. Challenges of the development for automotive parts remanufacturing in China. J Clean Prod 2017;140:1087–94. https://doi.org/10.1016/j.jclepro.2016.10.061.

[5]     Zhang X, Zhang M, Zhang H, Jiang Z, Liu C. A review on energy , environment and economic assessment in remanufacturing based on life cycle assessment method. J Clean Prod 2020;255:120160. https://doi.org/10.1016/j.jclepro.2020.120160.

[6]     Lee CM, Woo WS, Roh YH. Remanufacturing: Trends and issues. Int J Precis Eng Manuf - Green Technol 2017;4:113–25. https://doi.org/10.1007/s40684-017-0015-0.

[7]     Jiang Z, Zhou T, Zhang H, Wang Y, Cao H, Tian G. Reliability and cost optimization for remanufacturing process planning. J Clean Prod 2016;135:1602–10. https://doi.org/10.1016/j.jclepro.2015.11.037.

[8]     Liu Z, Jiang Q, Li T, Dong S, Yan S, Zhang H, et al. Environmental benefits of

remanufacturing: A case study of cylinder heads remanufactured through laser cladding. J Clean Prod 2016;133:1027–33. https://doi.org/10.1016/j.jclepro.2016.06.049.

[9]     Newman ST, Zhu Z, Dhokia V, Shokrani A. Process planning for additive and subtractive manufacturing technologies. CIRP Ann - Manuf Technol 2015;64:467–70. https://doi.org/10.1016/j.cirp.2015.04.109.

[10]    Ijomah WL, McMahon CA, Hammond GP, Newman ST. Development of design for remanufacturing guidelines to support sustainable manufacturing. Robot Comput Integr Manuf 2007;23:712–9. https://doi.org/10.1016/j.rcim.2007.02.017.

[11]    Zhang Y, Liu S, Liu Y, Yang H, Li M. The ' Internet of Things ' enabled real-time scheduling for remanufacturing of automobile engines. J Clean Prod 2018;185:562–75. https://doi.org/10.1016/j.jclepro.2018.02.061.

[12]    Zheng J, Li Z, Chen X. Worn area modeling for automating the repair of turbine blades. Int J Adv Manuf Technol 2006;29:1062–7. https://doi.org/10.1007/s00170-003-1990-6.

[13]    Wilson JM, Piya C, Shin YC, Zhao F, Ramani K. Remanufacturing of turbine blades by laser direct deposition with its energy and environmental impact analysis. J Clean Prod 2014;80:170–8. https://doi.org/10.1016/j.jclepro.2014.05.084.

[14]    Annie K, Jean-pierre K, Pierre D, Victor S, Vladimir P. Stochastic models and numerical solutions for manufacturing / remanufacturing systems with applications to the printer cartridge industry. J Manuf Syst 2015;37:662–71. https://doi.org/10.1016/j.jmsy.2014.11.019.

[15]    Yi P, Huang M, Guo L, Shi T. A retailer oriented closed-loop supply chain network design for end of life construction machinery remanufacturing. J Clean Prod 2016;124:191–203. https://doi.org/10.1016/j.jclepro.2016.02.070.

[16]    Feng C, Liang J, Gong C, Pai W, Liu S. Repair volume extraction method for

damaged parts in remanufacturing repair. Int J Adv Manuf Technol 2018;98:1523–36. https://doi.org/10.1007/s00170-018-2300-7.

[17]    Zhang X, Li W, Liou F. Damage detection and reconstruction algorithm in repairing compressor blade by direct metal deposition. Int J Adv Manuf Technol 2017. https://doi.org/10.1007/s00170-017-1413-8.

[18]    Li L, Li C, Tang Y, Du Y. An integrated approach of reverse engineering aided remanufacturing process for worn components. Robot Comput Integr Manuf 2017;48:39–50. https://doi.org/10.1016/j.rcim.2017.02.004.

[19]    Geng Z, Bidanda B. Review of reverse engineering systems–current state of the art. Virtual             Phys             Prototyp             2017;12:161–72. https://doi.org/10.1080/17452759.2017.1302787.

[20]    Nguyen A, Le B. 3D point cloud segmentation: A survey. IEEE Conf Robot Autom Mechatronics,      RAM      -      Proc      2013:225–30. https://doi.org/10.1109/RAM.2013.6758588.

[21]    Bhanu B, Lee S, Ho CC, Henderson T. Range Data Processing: Representation of Surfaces By Edges. Proc - Int Conf Pattern Recognit 1986:236–8.

[22]    Jiang XY, Meier U, Bunke H. Fast range image segmentation using high-level segmentation primitives. IEEE Work Appl Comput Vis - Proc 1996:83–8. https://doi.org/10.1109/acv.1996.572006.

[23]    Sappa AD, Devy M. Fast range image segmentation by an edge detection strategy. Proc Int Conf 3-D Digit Imaging Model 3DIM 2001;2001-Janua:292–9. https://doi.org/10.1109/IM.2001.924460.

[24]    Köster K, Spann M. MIR: An approach to robust clustering - application to range image segmentation. IEEE Trans Pattern Anal Mach Intell 2000;22:430–44. https://doi.org/10.1109/34.857001.

[25]    Rusu RB, Marton ZC, Blodow N, Dolha M, Beetz M. Towards 3D Point cloud

based object maps for household environments. Rob Auton Syst 2008;56:927–41. https://doi.org/10.1016/j.robot.2008.08.005.

[26]   Pu S, Vosselman G. Automatic extraction of building features from terrestrial laser scanning. Int Arch Photogramm 2006;36:25–7. https://doi.org/10.1.1.222.2486.

[27]   Biosca JM, Lerma JL. Unsupervised robust planar segmentation of terrestrial laser scanner point clouds based on fuzzy clustering methods. ISPRS J Photogramm Remote Sens 2008;63:84–98. https://doi.org/10.1016/j.isprsjprs.2007.07.010.

[28]   Filin S. Surface clustering from airborne laser scanning data. Int Arch Photogramm Remote Sens Spat Inf Sci 2001;34:119–124.

[29]   Vosselman G, Dijkman S. 3D building model reconstruction from point clouds and ground plans. Int Arch Photogramm Remote Sens 2001;XXXIV:37–43.

[30]   Tarsha-Kurdi F, Landes T, Grussenmeyer P. Hough-Transform and Extended Ransac Algorithms for Automatic Detection of 3D Building Roof Planes From Lidar Data. ISPRS Work Laser Scanning 2007 SilviLaser 2007 2007;XXXVI:407–12.

[31]   Li Y, Wu X, Chrysathou Y, Sharf A, Cohen-Or D, Mitra NJ. GlobFit: Consistently Fitting Primitives by Discovering Global Relations. ACM Trans Graph 2011;30:52:1--52:12. https://doi.org/10.1145/2010324.1964947.

[32]   Gelfand N, Guibas LJ. Shape segmentation using local slippage analysis. ACM Int Conf Proceeding Ser 2004;71:214–23. https://doi.org/10.1145/1057432.1057461.

[33]   Schnabel R, Degener P, Klein R. Completion and reconstruction with primitive shapes. Comput Graph Forum 2009;28:503–12. https://doi.org/10.1111/j.1467-8659.2009.01389.x.

[34]   Golovinskiy A, Funkhouser T. Min-cut based segmentation of point clouds. 2009 IEEE 12th Int Conf Comput Vis Work ICCV Work 2009 2009:39–46. https://doi.org/10.1109/ICCVW.2009.5457721.

145

[35] Strom J, Richardson A, Olson E. Graph-based segmentation for colored 3D laser point clouds. IEEE/RSJ 2010 Int Conf Intell Robot Syst IROS 2010 - Conf Proc 2010:2131–6. https://doi.org/10.1109/IROS.2010.5650459.

[36] Schoenberg JR, Nathan A, Campbell M. Segmentation of dense range information in complex urban scenes. IEEE/RSJ 2010 Int Conf Intell Robot Syst IROS 2010 - Conf Proc 2010:2033–8. https://doi.org/10.1109/IROS.2010.5651749.

[37] Hitchcox T, Zhao YF. Random walks for unorganized point cloud segmentation with application to aerospace repair. Procedia Manuf 2018;26:1483–91. https://doi.org/10.1016/j.promfg.2018.07.093.

[38] Grady L. Random Walks for Image Segmentation 2006;28:1768–83.

[39] Jovančević I, Pham HH, Orteu JJ, Gilblas R, Harvent J, Maurice X, et al. 3D Point Cloud Analysis for Detection and Characterization of Defects on Airplane Exterior Surface. J Nondestruct Eval 2017;36. https://doi.org/10.1007/s10921-017-0453-1.

[40] Borsu V, Yogeswaran A, Payeur P. Automated surface deformations detection and marking on automotive body panels. 2010 IEEE Int Conf Autom Sci Eng CASE 2010 2010:551–6. https://doi.org/10.1109/COASE.2010.5584643.

[41] Kashani AG, Graettinger AJ. Cluster-Based Roof Covering Damage Detection in Ground-Based Lidar Data. Autom Constr 2015;58:19–27. https://doi.org/10.1016/j.autcon.2015.07.007.

[42] Shinozaki Y, Kohira K, Masuda H. Detection of deterioration of furnace walls using large-scale point-clouds. Comput Aided Des Appl 2018;15:575–84. https://doi.org/10.1080/16864360.2017.1419645.

[43] Wang J, Fu P, Gao RX. Machine vision intelligence for product defect inspection based on deep learning and Hough transform. J Manuf Syst 2019;51:52–60. https://doi.org/10.1016/j.jmsy.2019.03.002.

[44] Iglesias C, Martínez J, Taboada J. Automated vision system for quality inspection

of slate slabs. Comput Ind 2018;99:119–29. https://doi.org/10.1016/j.compind.2018.03.030.

[45] Zeng J, Chang B, Du D, Hong Y, Zou Y, Chang S. A visual weld edge recognition method based on light and shadow feature construction using directional lighting. J Manuf Process 2016;24:19–30. https://doi.org/10.1016/j.jmapro.2016.07.002.

[46] Aminzadeh M, Kurfess T. Automatic thresholding for defect detection by background histogram mode extents. J Manuf Syst 2015;37:83–92. https://doi.org/10.1016/j.jmsy.2015.09.004.

[47] Tsai DM, Lin CT. Fast normalized cross correlation for defect detection. Pattern Recognit Lett 2003;24:2625–31. https://doi.org/10.1016/S0167-8655(03)00106-5.

[48] Crispin AJ, Rankov V. Automated inspection of PCB components using a genetic algorithm template-matching approach. Int J Adv Manuf Technol 2007;35:293–300. https://doi.org/10.1007/s00170-006-0730-0.

[49] Kong H, Yang J, Chen Z. Accurate and Efficient Inspection of Speckle and Scratch Defects on Surfaces of Planar Products. IEEE Trans Ind Informatics 2017;13:1855–65. https://doi.org/10.1109/TII.2017.2668438.

[50] Masci J, Meier U, Ciresan D, Schmidhuber J, Fricout G. Steel defect classification with Max-Pooling Convolutional Neural Networks. Proc Int Jt Conf Neural Networks 2012:10–5. https://doi.org/10.1109/IJCNN.2012.6252468.

[51] He K, Gkioxari G, Dollar P, Girshick R. Mask R-CNN. Proc IEEE Int Conf Comput Vis 2017;2017-Octob:2980–8. https://doi.org/10.1109/ICCV.2017.322.

[52] Ferguson M, Ak R, Lee Y-TT, Law KH. Detection and Segmentation of Manufacturing Defects with Convolutional Neural Networks and Transfer Learning. Smart Sustain Manuf Syst 2018;2:20180033. https://doi.org/10.1520/ssms20180033.

[53] Fooladgar F, Kasaei S. A survey on indoor RGB-D semantic segmentation: from

hand-crafted features to deep convolutional neural networks. Multimed Tools Appl 2020;79:4499–524. https://doi.org/10.1007/s11042-019-7684-3.

[54] Gupta S, Girshick R, Arbeláez P, Malik J. Learning rich features from RGB-D images for object detection and segmentation. Lect Notes Comput Sci (Including Subser Lect Notes Artif Intell Lect Notes Bioinformatics) 2014;8695 LNCS:345–60. https://doi.org/10.1007/978-3-319-10584-0_23.

[55] Song S, Xiao J. Deep sliding shapes for amodal 3D object detection in RGB-D images. Proc IEEE Comput Soc Conf Comput Vis Pattern Recognit 2016;2016-Decem:808–16. https://doi.org/10.1109/CVPR.2016.94.

[56] Song S, Lichtenberg SP, Xiao J. SUN RGB-D: A RGB-D scene understanding benchmark suite. Proc IEEE Comput Soc Conf Comput Vis Pattern Recognit 2015;07-12-June:567–76. https://doi.org/10.1109/CVPR.2015.7298655.

[57] Zhang X, Li W, Adkison KM, Liou F. Damage reconstruction from tri-dexel data for laser-aided repairing of metallic components. Int J Adv Manuf Technol 2018. https://doi.org/10.1007/s00170-018-1830-3.

[58] Zhang X, Li W, Cui W, Liou F. Modeling of worn surface geometry for engine blade repair using Laser-aided Direct Metal Deposition process. Manuf Lett 2018;15:1–4. https://doi.org/10.1016/j.mfglet.2017.11.001.

[59] Hascoët J, Touzé S, Rauch M. Automated identification of defect geometry for metallic part repair by an additive manufacturing process. Weld World 2018;62:229–41.

[60] He J, Li L, Li J. Research of key-technique on automatic repair system of plane blade welding. 2011 Int Conf Control Autom Syst Eng CASE 2011 2011. https://doi.org/10.1109/ICCASE.2011.5997615.

[61] Gao J, Chen X, Yilmaz O, Gindy N. An integrated adaptive repair solution for complex aerospace components through geometry reconstruction. Int J Adv Manuf

Technol 2008;36:1170–9. https://doi.org/10.1007/s00170-006-0923-6.

[62]    Yilmaz O, Gindy N, Gao J. A repair and overhaul methodology for aeroengine components. Robot Comput Integr Manuf 2010;26:190–201. https://doi.org/10.1016/j.rcim.2009.07.001.

[63]    Piya C, Wilson JM, Murugappan S, Shin Y, Ramani K. Virtual repair: Geometric reconstruction for remanufacturing gas turbine blades. ASME 2011 Int. Des. Eng. Tech. Conf. Comput. Inf. Eng. Conf. IDETC/CIE, vol. 9, 2011, p. 895–904. https://doi.org/10.1115/DETC2011-48652.

[64]    Goyal M, Murugappan S, Piya C, Benjamin W, Fang Y, Liu M, et al. Towards locally and globally shape-aware reverse 3D modeling. CAD Comput Aided Des 2012;44:537–53. https://doi.org/10.1016/j.cad.2011.12.004.

[65]    Wang J, Yu Z. Quadratic curve and surface fitting via squared distance minimization. Comput Graph 2011;35:1035–50. https://doi.org/10.1016/j.cag.2011.09.001.

[66]    Goshtasby  a. A. Grouping and parameterizing irregularly spaced points for curve fitting. ACM Trans Graph 2000;19:185–203. https://doi.org/10.1145/353981.353992.

[67]    Hoppe H, DeRose T, Duchamp T, Halstead M, Jin H, McDonald J, et al. Piecewise smooth surface reconstruction. Proc 21st Annu Conf Comput Graph Interact Tech - SIGGRAPH '94 1994:295–302. https://doi.org/10.1145/192161.192233.

[68]    Wang W, Pottmann H, Liu Y. Fitting B-spline curves to point clouds by curvature-based squared distance minimization. ACM Trans Graph 2006;25:214–38. https://doi.org/10.1145/1138450.1138453.

[69]    Nurunnabi A, Sadahiro Y, Lindenbergh R. Robust Cylinder Fitting in Three-Dimensional Point Cloud Data. ISPRS - Int Arch Photogramm Remote Sens Spat Inf Sci 2017;XLII-1/W1:63–70. https://doi.org/10.5194/isprs-archives-XLII-1-

W1-63-2017.

[70]   Fischler MA, Bolles RC. Random sample consensus: a paradigm for model fitting with applications to image analysis and automated cartography. Commun ACM 1981;24:381–95. https://doi.org/10.1145/358669.358692.

[71]   Schnabel R, Wahl R, Klein R. Efficient RANSAC for point-cloud shape detection. Comput Graph Forum 2007;26:214–26. https://doi.org/10.1111/j.1467-8659.2007.01016.x.

[72]   Le T, Duan Y. A primitive-based 3D segmentation algorithm for mechanical CAD models. Comput Aided Geom Des 2017;52–53:231–46. https://doi.org/10.1016/j.cagd.2017.02.009.

[73]   Terrazas CA, Gaytan SM, Rodriguez E, Espalin D, Murr LE, Medina F, et al. Multi-material metallic structure fabrication using electron beam melting. Int J Adv Manuf Technol 2014;71:33–45. https://doi.org/10.1007/s00170-013-5449-0.

[74]   Liu Q, Wang Y, Zheng H, Tang K, Li H, Gong S. TC17 titanium alloy laser melting deposition repair process and properties. Opt Laser Technol 2016;82:1–9. https://doi.org/10.1016/j.optlastec.2016.02.013.

[75]   Jahangir MN, Mamun MAH, Sealy MP. A review of additive manufacturing of magnesium alloys. AIP Conf Proc 2018;1980. https://doi.org/10.1063/1.5044305.

[76]   Dutta B, Froes FH (Sam. The Additive Manufacturing (AM) of titanium alloys. Met Powder Rep 2017;72:96–106. https://doi.org/10.1016/j.mprp.2016.12.062.

[77]   Liu J, Gaynor AT, Chen S, Kang Z, Suresh K, Takezawa A, et al. Current and future trends in topology optimization for additive manufacturing 2018.

[78]   Strong D, Kay M, Conner B, Wakefield T, Manogharan G. Hybrid manufacturing – integrating traditional manufacturers with additive manufacturing (AM) supply chain. Addit Manuf 2018;21:159–73. https://doi.org/10.1016/j.addma.2018.03.010.

[79] Le VT, Paris H, Mandil G. Environmental impact assessment of an innovative strategy based on an additive and subtractive manufacturing combination. J Clean Prod 2017;164:508–23. https://doi.org/10.1016/j.jclepro.2017.06.204.

[80] Gao W, Zhang Y, Ramanujan D, Ramani K, Chen Y, Williams CB, et al. The status, challenges, and future of additive manufacturing in engineering. CAD Comput Aided Des 2015;69:65–89. https://doi.org/10.1016/j.cad.2015.04.001.

[81] Cottam R, Brandt M. Laser cladding of Ti-6Al-4V powder on Ti-6Al-4V substrate: Effect of laser cladding parameters on microstructure. Phys Procedia 2011;12:323–9. https://doi.org/10.1016/j.phpro.2011.03.041.

[82] Zhang X, Li W, Chen X, Cui W, Liou F. Evaluation of component repair using direct metal deposition from scanned data. Int J Adv Manuf Technol 2017:1–14. https://doi.org/10.1007/s00170-017-1455-y.

[83] Zhao Z, Chen J, Zhang Q, Tan H, Lin X, Huang W dong. Microstructure and mechanical properties of laser additive repaired Ti17 titanium alloy. Trans Nonferrous Met Soc China (English Ed 2017;27:2613–21. https://doi.org/10.1016/S1003-6326(17)60289-9.

[84] Mandil G, Le VT, Paris H, Suard M. Building new entities from existing titanium part by electron beam melting: microstructures and mechanical properties. Int J Adv Manuf Technol 2016;85:1835–46. https://doi.org/10.1007/s00170-015-8049-3.

[85] Navrotsky V, Graichen A, Brodin H. Industrialisation of 3D printing (additive manufacturing) for gas turbine components repair and manufacturing. VGB PowerTech J 2015;12:48–52.

[86] Portolés L, Jordá O, Jordá L, Uriondo A, Esperon-Miguez M, Perinpanayagam S. A qualification procedure to manufacture and repair aerospace parts with electron beam melting. J Manuf Syst 2016;41:65–75. https://doi.org/10.1016/j.jmsy.2016.07.002.

[87]  Le VT, Paris H, Mandil G. The development of a strategy for direct part reuse using additive and subtractive manufacturing technologies. Addit Manuf 2018;22:687–99. https://doi.org/10.1016/j.addma.2018.06.026.

[88]  Le VT, Paris H, Mandil G. Process planning for combined additive and subtractive manufacturing technologies in a remanufacturing context. J Manuf Syst 2017;44:243–54. https://doi.org/10.1016/j.jmsy.2017.06.003.

[89]  Jones JB, McNutt P, Tosi R, Perry C, Wimpenny DI. Remanufacture of turbine blades by laser cladding, machining and in-process scanning in a single machine. 23rd Annu Int Solid Free Fabr Symp Austin, Texas, USA 2012:821–7. https://doi.org/https://doi.org/10.1016/j.phpro.2012.10.051.

[90]  Zheng Y, Qureshi AJ, Ahmad R. Algorithm for remanufacturing of damaged parts with hybrid 3D printing and machining process. Manuf Lett 2018;15:38–41. https://doi.org/10.1016/j.mfglet.2018.02.010.

[91]  Zhu Z, Dhokia V, Newman ST. A novel decision-making logic for hybrid manufacture of prismatic components based on existing parts. J Intell Manuf 2017;28:131–48. https://doi.org/10.1007/s10845-014-0966-8.

[92]  Liu J, Zheng Y, Ma Y, Qureshi A, Ahmad R. A Topology Optimization Method for Hybrid Subtractive–Additive Remanufacturing. Int J Precis Eng Manuf Technol 2019. https://doi.org/10.1007/s40684-019-00075-8.

[93]  Xu X, Wang L, Newman ST. Computer-aided process planning - A critical review of recent developments and future trends. Int J Comput Integr Manuf 2011;24:1–31. https://doi.org/10.1080/0951192X.2010.518632.

[94]  Lee DH, Kiritsis D, Xirouchakis P. Branch and fathoming algorithms for operation sequencing in process planning. Int J Prod Res 2001;39:1649–69. https://doi.org/10.1080/00207540010028100.

[95]  Deja M, Siemiatkowski MS. Machining process sequencing and machine

assignment in generative feature-based CAPP for mill-turn parts. J Manuf Syst 2018;48:49–62. https://doi.org/10.1016/j.jmsy.2018.06.001.

[96] Givehchi M, Haghighi A, Wang L. Generic machining process sequencing through a revised enriched machining feature concept. J Manuf Syst 2015;37:564–75. https://doi.org/10.1016/j.jmsy.2015.04.004.

[97] Lee DH, Kiritsis D, Xirouchakis P. Iterative approach to operation selection and sequencing in process planning. Int J Prod Res 2004;42:4745–66. https://doi.org/10.1080/00207540410001720412.

[98] Fernandes KJ, Raja VH. Incorporated Tool Selection System using object technology. Int J Mach Tools Manuf 2000;40:1547–55. https://doi.org/10.1016/S0890-6955(00)00027-4.

[99] Su Y, Chu X, Chen D, Sun X. A genetic algorithm for operation sequencing in CAPP using edge selection based encoding strategy. J Intell Manuf 2018;29:313–32. https://doi.org/10.1007/s10845-015-1109-6.

[100] Mokhtar A, Xu X. Machining precedence of 21/2D interacting features in a feature-based data model. J Intell Manuf 2011;22:145–61. https://doi.org/10.1007/s10845-009-0268-8.

[101] You CF, Sheen BT, Lin TK. Selecting optimal tools for arbitrarily shaped pockets. Int J Adv Manuf Technol 2007;32:132–8. https://doi.org/10.1007/s00170-005-0320-6.

[102] Meseguer A, Gonzalez F. A methodology for cutting-tool management through the integration of CAPP and scheduling. Int J Prod Res 2008;46:1685–706. https://doi.org/10.1080/00207540600898049.

[103] Huang SH, Xu N. Automatic set-up planning for metal cutting: An integrated methodology. Int J Prod Res 2003;41:4339–56. https://doi.org/10.1080/00207540310000153351.

[104] Frank MC, Wysk RA, Joshi SB. Determining setup orientations from the visibility of slice geometry for rapid computer numerically controlled machining. J Manuf Sci Eng Trans ASME 2006;128:228–38. https://doi.org/10.1115/1.2039100.

[105] Joneja A, Chang TC. Setup and fixture planning in automated process planning systems. IIE Trans (Institute Ind Eng 1999;31:653–65. https://doi.org/10.1080/07408179908969866.

[106] Singh P, Dutta D. Multi-Direction Slicing for Layered Manufacturing. J Comput Inf Sci Eng 2001;1:129. https://doi.org/10.1115/1.1375816.

[107] Ding D, Pan Z, Cuiuri D, Li H, Larkin N, Van Duin S. Automatic multi-direction slicing algorithms for wire based additive manufacturing. Robot Comput Integr Manuf 2016;37:130–50. https://doi.org/10.1016/j.rcim.2015.09.002.

[108] Zhang Y, Bernard A, Gupta RK, Harik R. Feature based building orientation optimization for additive manufacturing. Rapid Prototyp J 2016;22:358–76. https://doi.org/10.1108/RPJ-03-2014-0037.

[109] Ren L, Sparks T, Ruan J, Liou F. Process planning strategies for solid freeform fabrication of metal parts. J Manuf Syst 2008;27:158–65. https://doi.org/10.1016/j.jmsy.2009.02.002.

[110] Steuben JC, Iliopoulos AP, Michopoulos JG. Implicit slicing for functionally tailored additive manufacturing. CAD Comput Aided Des 2016;77:107–19. https://doi.org/10.1016/j.cad.2016.04.003.

[111] Flynn JM, Shokrani A, Newman ST, Dhokia V. Hybrid additive and subtractive machine tools - Research and industrial developments. Int J Mach Tools Manuf 2016;101:79–101. https://doi.org/10.1016/j.ijmachtools.2015.11.007.

[112] Arcella FG, Froes FH. Producing titanium aerospace components from powder using laser forming. Jom 2000;52:28–30. https://doi.org/10.1007/s11837-000-0028-x.

[113] Hybrid ManufacturingTechnologies. Hybrid Manufacturing Technologies n.d. http://www.hybridmanutech.com/ (accessed January 8, 2020).

[114] MORI D. LASERTEC 65 3D hybrid n.d. https://uk.dmgmori.com/products/machines/additive-manufacturing/powder-nozzle/lasertec-65-3d-hybrid (accessed January 8, 2020).

[115] MORI D. LASERTEC 125 3D hybrid n.d. https://uk.dmgmori.com/products/machines/additive-manufacturing/powder-nozzle/lasertec-125-3d-hybrid (accessed January 8, 2020).

[116] MORI D. LASERTEC 4300 3D hybrid n.d. https://uk.dmgmori.com/products/machines/additive-manufacturing/powder-nozzle/lasertec-4300-3d-hybrid (accessed January 8, 2020).

[117] Mazak. INTEGREX i-400S AM n.d. https://www.mazakusa.com/machines/integrex-i-400s-am/ (accessed January 8, 2020).

[118] Mazak. VC-500A/5X AM HWD n.d. https://www.mazakusa.com/machines/vc-500a-5x-am-hwd/ (accessed January 8, 2020).

[119] Cybaman. CybaCast Hybrid n.d. http://www.cybamantech.co.uk/en/products/additive_manufacturing/cyba_cast_hybrid (accessed January 8, 2020).

[120] Technologies WM. WFL n.d. https://www.machinery.co.uk/machinery-features/wfl-millturn-technologies-kyal-machine-tools-additive-manufacturing (accessed January 8, 2020).

[121] Hermle. The MPA 40 n.d. https://3dprint.com/46227/hybrid-cnc-mill-and-additive-manufacturing-marvel/ (accessed January 8, 2020).

[122] Sodick. OPM250L n.d. https://www.sodick.com/products/metal-3d-printing/opm250l (accessed January 8, 2020).

[123] Matsuura. LUMEX Avance-25 n.d. https://www.lumex-matsuura.com/english/lumex-avance-25 (accessed January 8, 2020).

[124] Matsuura. LUMEX Avance-60 n.d. https://www.lumex-matsuura.com/english/lumex-avance-60 (accessed January 8, 2020).

[125] Zhu Z, Dhokia VG, Nassehi A, Newman ST. A review of hybrid manufacturing processes - State of the art and future perspectives. Int J Comput Integr Manuf 2013;26:596–615. https://doi.org/10.1080/0951192X.2012.749530.

[126] Behandish M, Nelaturi S, de Kleer J. Automated process planning for hybrid manufacturing. CAD Comput Aided Des 2018;102:115–27. https://doi.org/10.1016/j.cad.2018.04.022.

[127] Manogharan G, Wysk R, Harrysson O, Aman R. AIMS - A Metal Additive-hybrid Manufacturing System: System Architecture and Attributes. Procedia Manuf 2015;1:273–86. https://doi.org/10.1016/j.promfg.2015.09.021.

[128] Joshi A, Anand S. Geometric Complexity Based Process Selection for Hybrid Manufacturing. Procedia Manuf 2017;10:578–89. https://doi.org/10.1016/j.promfg.2017.07.056.

[129] Chen L, Xu K, Tang K. Optimized sequence planning for multi-axis hybrid machining of complex geometries. Comput Graph 2018;70:176–87. https://doi.org/10.1016/j.cag.2017.07.018.

[130] Kerbrat O, Mognol P, Hascoët JY. A new DFM approach to combine machining and additive manufacturing. Comput Ind 2011;62:684–92. https://doi.org/10.1016/j.compind.2011.04.003.

[131] Zhu Z, Dhokia V, Newman ST. The development of a novel process planning algorithm for an unconstrained hybrid manufacturing process. J Manuf Process 2013;15:404–13. https://doi.org/10.1016/j.jmapro.2013.06.006.

[132] Zhu Z, Dhokia V, Newman ST, Nassehi A. Application of a hybrid process for high

precision manufacture of difficult to machine prismatic parts. Int J Adv Manuf Technol 2014;74:1115–32. https://doi.org/10.1007/s00170-014-6053-7.

[133] ElMaraghy H, Moussa M. Optimal platform design and process plan for managing variety using hybrid manufacturing. CIRP Ann 2019:4–7. https://doi.org/10.1016/j.cirp.2019.03.025.

[134] Liu J, Zheng Y, Ma Y, Qureshi A, Ahmad R. A Topology Optimization Method for Hybrid Subtractive–Additive Remanufacturing. Int J Precis Eng Manuf Technol 2019:1–24. https://doi.org/10.1007/s40684-019-00075-8.

[135] Li L, Liu J, Ma Y, Ahmad R, Qureshi A. Multi-view feature modeling for design-for-additive manufacturing. Adv Eng Informatics 2019;39:144–56. https://doi.org/10.1016/j.aei.2018.12.004.

[136] Verma AK, Rajotia S. A review of machining feature recognition methodologies. Int J Comput Integr Manuf 2010;23:353–68. https://doi.org/10.1080/09511921003642121.

[137] Le VT, Paris H, Mandil G. Extraction of features for combined additive manufacturing and machining processes in a remanufacturing context. Adv. Mech. Des. Eng. Manuf., Springer International Publishing; 2017, p. 179–89. https://doi.org/10.1007/978-3-319-45781-9_19.

[138] Le VT, Paris H, Mandil G. Extracting features for manufacture of parts from existing components based on combining additive and subtractive technologies. Int J Interact Des Manuf 2018;12:525–36. https://doi.org/10.1007/s12008-017-0395-y.

[139] Kerbrat O, Mognol P, Hascoët J-Y. A new DFM approach to combine machining and additive manufacturing. Comput Ind 2011;62:684–92. https://doi.org/10.1016/j.compind.2011.04.003.

[140] Manogharan G, Wysk RA, Harrysson OLA. Additive manufacturing-integrated hybrid manufacturing and subtractive processes: Economic model and analysis. Int

J Comput Integr Manuf 2016;29:473–88. https://doi.org/10.1080/0951192X.2015.1067920.

[141] Babic B, Nesic N, Miljkovic Z. A review of automated feature recognition with rule-based pattern recognition. Comput Ind 2008;59:321–37. https://doi.org/10.1016/j.compind.2007.09.001.

[142] He K, Zhang X, Ren S, Sun J. Deep residual learning for image recognition. Proc IEEE Comput Soc Conf Comput Vis Pattern Recognit 2016;2016-Decem:770–8. https://doi.org/10.1109/CVPR.2016.90.

[143] Lin TY, Dollár P, Girshick R, He K, Hariharan B, Belongie S. Feature pyramid networks for object detection. Proc - 30th IEEE Conf Comput Vis Pattern Recognition, CVPR 2017 2017;2017-Janua:936–44. https://doi.org/10.1109/CVPR.2017.106.

[144] Girshick R. Fast R-CNN. Proc IEEE Int Conf Comput Vis 2015;2015 Inter:1440–8. https://doi.org/10.1109/ICCV.2015.169.

[145] Lin TY, Maire M, Belongie S, Hays J, Perona P, Ramanan D, et al. Microsoft COCO: Common objects in context. Lect Notes Comput Sci (Including Subser Lect Notes Artif Intell Lect Notes Bioinformatics) 2014;8693 LNCS:740–55. https://doi.org/10.1007/978-3-319-10602-1_48.

[146] Dutta A, Zisserman A. The VIA annotation software for images, audio and video. MM 2019 - Proc 27th ACM Int Conf Multimed 2019:2276–9. https://doi.org/10.1145/3343031.3350535.

[147] Rabbani T, Heuvel F Van Den. Efficient Hough Transform for Automatic Detection of Cylinders in Point Clouds. ISPRS Work Laser Scanning 2005;3:60–65. https://doi.org/10.1.1.118.1736.

[148] Tran TT, Cao VT, Laurendeau D. Extraction of cylinders and estimation of their parameters from point clouds. Comput Graph 2015;46:345–57.

https://doi.org/10.1016/j.cag.2014.09.027.

[149] Gomes AJP, Teixeira JG. Form feature modelling in a hybrid CSG/BRep scheme. Comput Graph 1991;15:217–29. https://doi.org/10.1016/0097-8493(91)90075-S.

[150] Zheng Y, Liu J, Liu Z, Wang T, Ahmad R. A primitive-based 3D reconstruction method for remanufacturing. Int J Adv Manuf Technol 2019:3667–81. https://doi.org/10.1007/s00170-019-03824-w.

[151] Bénière R, Subsol G, Gesquière G, Le Breton F, Puech W. A comprehensive process of reverse engineering from 3D meshes to CAD models. CAD Comput Aided Des 2013;45:1382–93. https://doi.org/10.1016/j.cad.2013.06.004.

[152] Rickenbacher L, Spierings A, Wegener K. An integrated cost-model for selective laser melting (SLM). Rapid Prototyp J 2013;19:208–14. https://doi.org/10.1108/13552541311312201.

[153] Chen L, Lau TY, Tang K. Manufacturability analysis and process planning for additive and subtractive hybrid manufacturing of Quasi-rotational parts with columnar features. CAD Comput Aided Des 2020;118:102759. https://doi.org/10.1016/j.cad.2019.102759.

[154] Cai S, Zhang W, Zhu J, Gao T. Stress constrained shape and topology optimization with fixed mesh: A B-spline finite cell method combined with level set function. Comput Methods Appl Mech Eng 2014;278:361–87. https://doi.org/10.1016/j.cma.2014.06.007.

[155] Zhang Z, Jaiswal P, Rai R. FeatureNet: Machining feature recognition based on 3D Convolution Neural Network. CAD Comput Aided Des 2018;101:12–22. https://doi.org/10.1016/j.cad.2018.03.006.

[156] Shi P, Qi Q, Qin Y, Scott PJ, Jiang X. A novel learning-based feature recognition method using multiple sectional view representation. J Intell Manuf 2020;31:1291–309. https://doi.org/10.1007/s10845-020-01533-w.

[157] Jung JY. Manufacturing cost estimation for machined parts based on manufacturing features. J Intell Manuf 2002;13:227–38. https://doi.org/10.1023/A:1016092808320.

[158] Barclift M, Joshi S, Simpson T, Dickman C. Cost Modeling and Depreciation for Reused Powder Feedstocks in Powder Bed Fusion Additive Manufacturing. Solid Free Fabr Proc 2016:2007–28.

[159] Bouaziz Z, Younes J Ben, Zghal A. Cost estimation system of dies manufacturing based on the complex machining features. Int J Adv Manuf Technol 2006;28:262–71. https://doi.org/10.1007/s00170-004-2179-3.

[160] Komineas G, Foteinopoulos P, Papacharalampopoulos A, Stavropoulos P. Build Time Estimation Models in Thermal Extrusion Additive Manufacturing Processes. Procedia Manuf 2018;21:647–54. https://doi.org/10.1016/j.promfg.2018.02.167.

[161] Zheng Y, Liu J, Ahmad R. A cost-driven process planning method for hybrid additive–subtractive remanufacturing. J Manuf Syst 2020;55:248–63. https://doi.org/10.1016/j.jmsy.2020.03.006.

# Appendix

**NURBS surface fitting from point clouds:**

NURBS surface:

$$p(u,v) = \frac{\sum_{i=0}^{m} \sum_{j=0}^{n} \omega_{i,j} d_{i,j} N_{i,k}(u) N_{j,l}(v)}{\sum_{i=0}^{m} \sum_{j=0}^{n} \omega_{i,j} N_{i,k}(u) N_{j,l}(v)}$$

where $\omega_{i,j}$ is the weight of control points; $d_{i,j}$ is the control point; $N_{i,k}(u)$ and $N_{j,l}(v)$ are the basis B-spline functions in $u$ and $v$ direction separately, they are defined over the knot vectors as: $U = [u_0, u_1, \cdots, u_{m+k+1}]$, $V = [v_0, v_1, \cdots, v_{m+k+1}]$.

Matrix formulation:

$$p_{i,j}(\alpha, \beta) = \frac{U M_i D_{i,j} M_j^T V^T}{U M_i W_{i,j} M_j^T V^T}$$

where $i = 0,1,\cdots, m-3$; $j = 0,1,\cdots, n-3$;

$U = [1 \quad \alpha \quad \alpha^2 \quad \alpha^3]$, $V = [1 \quad \beta \quad \beta^2 \quad \beta^3]$;

$$M_i = \begin{bmatrix} m_{11} & m_{12} & m_{13} & m_{14} \\ m_{21} & m_{22} & m_{23} & m_{24} \\ m_{31} & m_{32} & m_{33} & m_{34} \\ m_{41} & m_{42} & m_{43} & m_{44} \end{bmatrix};$$

$$M_i = \begin{bmatrix} \dfrac{(\Delta_{i+3})^2}{\Delta_{i+2}^2 \Delta_{i+1}^3} & 1 - m_{11} - m_{13} & \dfrac{(\Delta_{i+2})^2}{\Delta_{i+2}^2 \Delta_{i+2}^3} & 0 \\[3mm] -3m_{11} & 3m_{11} - m_{23} & \dfrac{3\Delta_{i+2}\Delta_{i+3}}{\Delta_{i+2}^2 \Delta_{i+2}^3} & 0 \\[3mm] 3m_{11} & -3m_{11} - m_{33} & \dfrac{3(\Delta_{i+3})^2}{\Delta_{i+2}^2 \Delta_{i+2}^3} & 0 \\[3mm] -m_{11} & m_{11} - m_{43} - m_{44} & -\left(\dfrac{1}{3}m_{33} + m_{44} + \dfrac{(\Delta_{i+3})^2}{\Delta_{i+3}^2 \Delta_{i+2}^3}\right) & \dfrac{(\Delta_{i+3})^2}{\Delta_{i+3}^2 \Delta_{i+3}^3} \end{bmatrix};$$

$$D_{i,j} = \begin{bmatrix} \omega_{i,j}d_{i,j} & \omega_{i,j+1}d_{i,j+1} & \omega_{i,j+2}d_{i,j+2} & \omega_{i,j+3}d_{i,j+3} \\ \omega_{i+1,j}d_{i+1,j} & \omega_{i+1,j+1}d_{i+1,j+1} & \omega_{i+1,j+2}d_{i+1,j+2} & \omega_{i+1,j+3}d_{i+1,j+3} \\ \omega_{i+2,j}d_{i+2,j} & \omega_{i+2,j+1}d_{i+2,j+1} & \omega_{i+2,j+2}d_{i+2,j+2} & \omega_{i+2,j+3}d_{i+2,j+3} \\ \omega_{i+3,j}d_{i+3,j} & \omega_{i+3,j+1}d_{i+3,j+1} & \omega_{i+3,j+2}d_{i+3,j+2} & \omega_{i+3,j+3}d_{i+3,j+3} \end{bmatrix};$$

$$W_{i,j} = \begin{bmatrix} \omega_{i,j} & \omega_{i,j+1} & \omega_{i,j+2} & \omega_{i,j+3} \\ \omega_{i+1,j} & \omega_{i+1,j+1} & \omega_{i+1,j+2} & \omega_{i+1,j+3} \\ \omega_{i+2,j} & \omega_{i+2,j+1} & \omega_{i+2,j+2} & \omega_{i+2,j+3} \\ \omega_{i+3,j} & \omega_{i+3,j+1} & \omega_{i+3,j+2} & \omega_{i+3,j+3} \end{bmatrix};$$

$$\alpha = \frac{u-u_i}{u_{i+1}-u_i}, \beta = \frac{v-v_i}{v_{i+1}-v_i} \ (0 \le \alpha, \beta \le 1);$$

$$\Delta_i = u_{i+1} - u_i; \Delta_i^2 = u_{i+2} - u_i; \Delta_i^3 = u_{i+3} - u_i.$$

Parameterization of knot vector:

$$\begin{cases} u_0 = u_1 = u_2 = u_3 = 0; \\ u_{i+3} = u_{i+2} + |p_i - p_{i-1}|^{1/2} \Big/ \sum_{i=1}^{n} |p_i - p_{i-1}|^{1/2}; \\ u_{n+3} = u_{n+4} = u_{n+5} = u_{n+6} = 1 \end{cases}$$

where $i = 1,2,\cdots,n-1$ and $p_i$ is a measured point.

Boundary condition:

Freeform terminal vertex condition: $\begin{cases} d_0 = d_1 \\ d_{n+2} = d_{n+1} \end{cases};$

Closed curve condition: $\begin{cases} d_0 = d_{n+1} \\ d_1 = d_{n+2} \end{cases}.$

Calculation of control points:

$$\begin{bmatrix} B_1 & C_1 & & & & & A_1 \\ A_2 & B_2 & C_2 & & & & \\ & \cdot & \cdot & \cdot & & & \\ & & \cdot & \cdot & \cdot & & \\ & & & \cdot & \cdot & \cdot & \\ & & & & A_{n-3} & B_{n-3} & C_{n-3} \\ C_{n-2} & & & & & A_{n-2} & B_{n-2} \end{bmatrix} \begin{bmatrix} d_1 \\ d_2 \\ \cdot \\ \cdot \\ \cdot \\ d_{n-3} \\ d_{n-2} \end{bmatrix} = \begin{bmatrix} E_1 \\ E_2 \\ \cdot \\ \cdot \\ \cdot \\ E_{n-3} \\ E_{n-2} \end{bmatrix}$$

Where $A_i = \dfrac{(\Delta_{i+2})^2}{\Delta_i + \Delta_{i+1} + \Delta_{i+2}}$; $B_i = \dfrac{\Delta_{i+2}(\Delta_i + \Delta_{i+1})}{\Delta_i + \Delta_{i+1} + \Delta_{i+2}} + \dfrac{\Delta_{i+1}(\Delta_{i+2} + \Delta_{i+3})}{\Delta_{i+1} + \Delta_{i+2} + \Delta_{i+3}}$; $C_i = \dfrac{(\Delta_{i+1})^2}{\Delta_{i+1} + \Delta_{i+2} + \Delta_{i+3}}$;

$$E = (\Delta_{i+1} + \Delta_{i+2})p_{i-1}$$

$p_i$ is the control point and $\Delta_i = u_{i+1} - u_i (i = 1,2,\cdots.n-2)$.

**Level set function for the final part in Chapter 5 case study 1:**

$$\Phi_{\text{cube1}} = \min(120 - x, y - 30, 110 - y, y - 40, 25 - z, z - 10);$$

$$\Phi_{\text{cube2}} = \min(111 - x, x - 39, 98.5 - y, y - 51.5, 35 - z, z - 25);$$

$$\Phi_{\text{cube3}} = \min(89.5 - x, x - 60.5, 45 - y, y - 40, 21.75 - z, z - 13.25);$$

$$\Phi_{\text{cube4}} = \min(89.5 - x, x - 60.5, 59 - y, y - 60.5, 32 - z, z - 28);$$

$$\Phi_{\text{cyl1}} = \min\{6.25 - (z - 30)^2 - (y - 75)^2, 114.75 - x, x - 104.75\};$$

$$\Phi_{\text{cyl2}} = \min\{25 - (z - 17.5)^2 - (y - 75)^2, 120 - x, x - 105\};$$

$$\Phi_{\text{cyl3}} = \min\{6.25 - (z - 17.5)^2 - (x - 68)^2, 50 - y, y - 45\};$$

$$\Phi_{\text{cyl4}} = \min\{6.25 - (z - 17.5)^2 - (x - 82)^2, 50 - y, y - 45\};$$

$\Phi_{\text{free}} = \min\{-(x - 55)^3 + (x - 55)^2 * (18 * (y - 55) + 19200) + (x - 55) *$
$(108 * (y - 55)^2 - 46080 * (y - 55) + 216 * (y - 55)^3 + 15360 * (y - 55)^2, x +$
$y - 110, 83 - z, z - 68\}.$

**Level set function for the used part in Chapter 5 case study 1:**

$$\Phi_{\text{cube1}} = \min(125 - x, x - 25, 112.5 - y, y - 37.5, 37.5 - z, z - 12.5);$$

$$\Phi_{\text{cube2}} = \min(115 - x, x - 35, 102.5 - y, y - 47.5, 37.5 - z, z - 32.5);$$

$$\Phi_{\text{cube3}} = \min(70 - x, x - 40, 87.5 - y, y - 52.5, 32.5 - z, z - 27.5);$$

$$\Phi_{\text{cube4}} = \min(110 - x, x - 80, 87.5 - y, y - 52.5, 32.5 - z, z - 27.5);$$